Chair of Nonferrous Metallurgy

Doctoral Thesis

High precision measurements on metallic systems using Fast Scanning Calorimetry

Cameron Ross Quick, MChem.

October 2022

AFFIDAVIT

I declare on oath that I wrote this thesis independently, did not use other than the specified sources and aids, and did not use any unauthorized aids.

I declare that I have read, understood, and complied with the guidelines of the senate of the Montanuniversitaet Leoben for "Good Scientific Practice".

Furthermore, I declare that the electronic and printed version of the submitted thesis are identical, both, formally and with regard to content.

Date 18.10.2021

_____
Signature Author
Cameron Ross Quick

ACKNOWLEDGEMENTS

ABSTRACT

Modern metallurgy and alloy design can make use of a multitude of characterisation techniques to develop materials and processes for desirable properties such as low density and high strength. However, the technical capabilities of modern devices are in some cases ahead of the practical expertise, and state of the art research can greatly benefit from an optimised and robust execution of experiments.

This thesis explores some approaches to high precision measurements on metallic systems using micro-electromechanical systems-based (MEMS-based) technologies, with a particular focus on Fast Differential Scanning Calorimetry (FDSC). FDSC uses modern MEMS fabrication techniques in the construction of a nanocalorimeter which achieves high sensitivity and heating rates orders of magnitude faster than conventional calorimetry devices. Material heat capacity was investigated, owing firstly to its well documented and calculable equilibrium properties, and secondly to its practical importance for materials science. Precise heat capacity measurements were made on pure lead and aluminium, where comparisons to literature helped develop and validate an experimental methodology based on cyclic thermal treatments and a correction for intrinsic heat losses. A eutectic AlSi12 alloy is then similarly examined at rapid heating rates comparable to those occurring during metal additive manufacturing. Varied quench and re-heating rates reveal the kinetics of the supersaturated Al-Si system, while the experimental approach is carefully explained to inform related experiments using FDSC.

A further MEMS-based technique was also explored, whereby sample heating in-situ inside a transmission electron microscope (TEM) is possible. Novel sample preparation techniques were employed, similar to those used for metallic foil preparation in FDSC, to investigate heat treatment in an AlMgZn(Cu) aluminium crossover alloy. The specific approach to sample preparation is described in detail and its merits are discussed in comparison to more conventional methods, while the techniques and results are demonstrative for related experiments on metallic foils.

KURZFASSUNG

Die moderne Metallurgie und das Legierungsdesign können eine Vielzahl von Charakterisierungstechniken nutzen, um Werkstoffe und Verfahren für erwünschte Eigenschaften wie geringe Dichte und hohe Festigkeit zu entwickeln. Die technischen Möglichkeiten moderner Geräte sind jedoch in einigen Fällen dem praktischen Fachwissen voraus und die Forschung auf dem neuesten Stand der Technik kann von einer optimierten Durchführung von Experimenten stark profitieren.

In dieser Arbeit werden einige Ansätze für hochpräzise Messungen an metallischen Systemen unter Verwendung von MEMS-Technologien (mikroelektromechanische Systeme) untersucht, wobei ein besonderer Schwerpunkt auf der schnellen Differenzialscanningkalorimetrie (FDSC) liegt. Bei der FDSC werden moderne MEMS-Fertigungstechniken für die Konstruktion eines Nanokalorimeters verwendet, das eine hohe Empfindlichkeit und um Größenordnungen schnellere Heizraten als herkömmliche Kalorimetriegeräte erreicht. Die Wärmekapazität von Materialien wurde untersucht, zum einen wegen ihrer gut dokumentierten und berechenbaren Gleichgewichtseigenschaften, zum anderen wegen ihrer praktischen Bedeutung für die Materialwissenschaft. Präzise Wärmekapazitätsmessungen wurden an reinem Blei und Aluminium durchgeführt, wobei Vergleiche mit der Literatur zur Entwicklung und Validierung einer experimentellen Methodik beitrugen, die auf zyklischen Wärmebehandlungen und einer Korrektur für intrinsische Wärmeverluste beruht. Eine eutektische AlSi12-Legierung wird dann in ähnlicher Weise bei schnellen Erwärmungsraten untersucht, wie sie bei der additiven Fertigung von Metallen auftreten. Unterschiedliche Abschreck- und Wiederaufheizraten zeigen die Kinetik des übersättigten Al-Si-Systems auf, während der experimentelle Ansatz sorgfältig erläutert wird, um Informationen für ähnliche Experimente bereitzustellen.

Eine weitere MEMS-basierte Technik wurde ebenfalls erforscht, bei der eine Probenerwärmung in-situ in einem Transmissionselektronenmikroskop (TEM) möglich ist. Für die Untersuchung der Wärmebehandlung einer AlMgZn(Cu)-Aluminium-Crossover-Legierung wurden neuartige Probenvorbereitungstechniken eingesetzt, die denen für die Vorbereitung von Metallfolien in der FDSC ähneln. Es erfolgt eine ausführliche Beschreibung des spezifischen Ansatzes für die Probenvorbereitung und seine Vorzüge werden im Vergleich zu konventionellen Methoden diskutiert, während die Techniken und Ergebnisse für verwandte Experimente an Metallfolien demonstriert werden.

TABLE OF CONTENTS

1. INTRODUCTION

Sophistication and miniaturisation of electronics has been instrumental in technological development of the last century, pervading every aspect of modern society. Scientific equipment of course is no exception. Besides the obvious move to semiconductor-based computation technology, sophistication of sensor technology based on electronic circuits is largely responsible for the evolution of scientific measurement, and continues to bridge the technology gap to better precision and new measurement opportunities.

Micro-electro-mechanical systems (MEMS) is a broad area of technology, finding many applications and also supporting ground breaking research in many scientific fields. Utilising state of the art circuit fabrication, a high variety of MEMS sensor chips are produced for new and diverse experiments with scientific measurement devices, for instance transmission electron microscopes (TEMs) and calorimeters. Their use in electron microscopy tends to involve in-situ experiments, and successful manipulation of sample conditions while observing the changes in real time. Meanwhile, MEMS sensors in calorimetry have developed alongside the instruments they integrate with to greatly expand the precision and temperature rates possible during measurement, this new technique falling into the discipline fast scanning calorimetry (FSC). While early applications of FSC involved custom-built devices, the technique's many advantages have brought a lot of scientific interest with commercial measurement solutions now available in devices such as Mettler-Toledo's Flash DSC 2+.

In metallurgy, thermal history and heat treatments majorly impact the state and properties of the material. Such properties are evaluated through numerous means such as mechanical testing, chemical analysis, microscopy analysis, calorimetric analysis and also through kinetic and thermodynamic calculations. MEMS implementation in Fast Scanning Calorimetry, which is the main topic in this thesis, allows heat experiments and analysis at extremely rapid temperature changes (up to 50,000 K s^{-1}), which becomes increasingly relevant to state-of-the-art materials and processing methods.

This thesis explores the measurement and interpretation of specific heat capacity curves for metallic systems measured at high scanning rates using FSC. Major focus is given to developing a robust methodology for high precision measurements involving a correction for systematic heat losses.

Additionally, TEM is used with an appropriate MEMS sensor to observe precipitation and grain boundary movement in a crossover AlMgZn(Cu) alloy *in-situ* during a paint bake heat treatment. Here once more the major focus is given to the methodology, namely the sample preparation, which was derived from FSC sample preparation methods using a scalpel and hair stylus to section and position the sample. This approach avoids the inherent problems in a conventional focused ion beam (FIB) based approach such as contamination from welding and implantation of Ga ions.

Furthermore, the work presented herein explores the potential of a MEMS-based approach to material characterisation with state of the art equipment and materials, while already providing new and vital data on heat-induced changes in metallic materials.

2. STATE OF THE ART

2.1. FOUNDATIONS OF HEAT CAPACITY, ENTROPY, AND GIBBS FREE ENERGY

Among the most crucial and fundamental material properties is that of heat capacity (C), the material response to heat being integral to the physical sciences, and describes how an increase in a system's internal energy (U) manifests an increase in temperature (T).

If a constant volume (V) is considered, then the change in internal energy does not involve any thermal expansion work done by the system and the heat capacity at constant volume (C_V) is written as Equation 2.1 [1].

$$C_V = \left(\frac{\delta U}{\delta T}\right)_V \qquad \text{Equation 2.1}$$

Practically, a measured material is not normally confined in its volume; but, the work done by thermal expansion of a solid on the surrounding atmosphere has negligible impact on the pressure of the surroundings. Therefore, considering the heat capacity at constant pressure (C_p) during an enthalpy change, since no expansion work is done by system on the surroundings, the change in internal energy of the system is identical to the enthalpy change of the system (dH) giving Equation 2.2. [1]

$$C_p = \left(\frac{\delta H}{\delta T}\right)_p \qquad \text{Equation 2.2}$$

When no other work is done by the system, this enthalpy change is also identical to the heat supplied to the system (dq), allowing construction of Equation 2.3.

$$dH = dq = C_p dT \qquad \text{Equation 2.3}$$

This definition in terms of state variables is extremely relevant for calorimetry measurements, where these parameters of heat and temperature are the major measurement concerns. The C_p per unit mass is the specific heat capacity (in J K^{-1} g^{-1}), and is given the symbol c_p.

A thermodynamic description of heat capacity is approached by considering the thermodynamics of a reversible process general [2]. From the 2nd law of thermodynamics, it can be stated that the entropy of an isolated system must increase over the course of a spontaneous change, and at equilibrium there is no change in entropy (since it is a state function).

To describe the actual spontaneity of a process at constant pressure and temperature, the entropic and enthalpic changes can be accounted for in the Gibbs free energy equation (Equation 2.4), where ΔG is the change in Gibbs energy, and ΔH and ΔS are the enthalpy and entropy changes involved in the process. When $\Delta G < 0$, the change occurs spontaneously.

$$\Delta G = \Delta H - T \cdot \Delta S \qquad \text{Equation 2.4}$$

The amount of entropy added to the system as a result of heating was described in 1855 by the Clausius theorem (Equation 2.5), where dq is the energy supplied as heat at temperature T.

$$dS = \frac{dq}{T} \qquad\qquad \text{Equation 2.5}$$

Using Equation 2.3, this relation can be written in terms of c_p (Equation 2.6), and the absolute entropy found by integrating over temperature change, as in Equation 2.7, where S_T and S_{T_1} are the entropy values at temperatures T and T_1, respectively.

$$dS = \frac{c_p}{T} dT \qquad\qquad \text{Equation 2.6}$$

$$S_T = S_{T_1} + \int_{T_1}^{T} \frac{c_p}{T} dT \qquad\qquad \text{Equation 2.7}$$

In terms of these definitions, the Gibbs energy of a system at constant pressure can be formulated as Equation 2.8 [2]:

$$G_T(T) = H_{T_1} + \int_{T_1}^{T} c_p(T) dT - T \left[S_{T_1} + \int_{T_1}^{T} \frac{c_p(T)}{T} dT \right] \qquad \text{Equation 2.8}$$

Importantly, here the Gibbs energy (at constant pressure) is expressed as the function of a single temperature-dependent variable: the specific heat capacity, $c_p(T)$. With the constants S_{T_1} and H_{T_1} being the entropy and enthalpy of the system at temperature T_1. All the parameters on which Gibbs energy depends can be determined experimentally (e.g. with calorimetry) or derived from first principles [3] (e.g. from *ab-initio* simulations). This relationship proves to be extremely powerful in making predictions of the equilibrium state of a system, since thermodynamically the most stable state of a system is that of lowest Gibbs energy. Furthermore, the dependence behaviour of the Gibbs energy curves with temperature, pressure, composition and even parameters like electrical fields, can reveal something of the thermodynamic properties of the material's phases and phase transitions. For instance, when the 1st derivative of the Gibbs energy across a phase transformation is discontinuous, as is the case for the line intersections in Figure 2.1a, the phase transition can be classified as 1st order, which has implications on the nature of the conversion process.

The variation of Gibbs energy with temperature is shown in Figure 2.1a [1] for the respective solid, liquid and gas phases of a pure substance. The actual equilibrium state of the system at a given temperature is whichever has the lowest Gibbs energy (traced by the dotted line), with the phase transitions occurring at these changes in gradient. Figure 2.1b depicts a unary phase diagram at constant pressure, with the melting point (m.p.) at the solid-liquid intersection and the boiling at the liquid-gas intersection (b.p.).
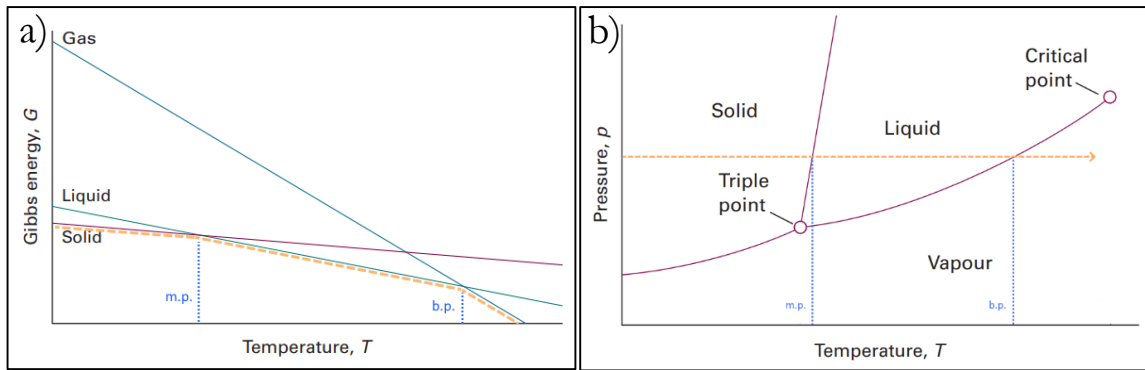
Figure 2.1: a) Gibbs energy dependence on temperature for the solid, liquid and gas phases of a substance at constant pressure [1]. Melting and boiling occurs when a phase change serves to minimise the Gibbs energy. b) shows a generalised unary phase diagram. A typical heating path through solid, liquid and gas phases is highlighted by the dotted line in both panels.

For multicomponent systems, metallic alloys for example, the Gibbs energy can be represented by the partial contributions of each species in pure form (dependent on their mole fractions), and an additional contribution, ΔG_{mix}, due to the enthalpy and entropy changes involved in mixing the species [1,2]. For a binary system of A and B, the total Gibbs energy can be then written as Equation 2.9.

$$G_{total} = \chi_A G_A + \chi_B G_B + \Delta G_{mix} \qquad\qquad \text{Equation 2.9}$$

This additional contribution is associated with attractive and repulsive forces between the components, and in the case that a solution is formed, effectively curves the Gibbs energies, $G(T)$ of the respective phases. The Gibbs energy diagram is plotted over mole fraction for the fcc and liquid phases of the Ni-Cu binary system at 1523 K and constant pressure in Figure 2.2a [2], with the corresponding phase diagram in Figure 2.2b [4].

Figure 2.2: a) Gibbs energy curves of fcc and liquid phases in Ni-Cu binary system at 1523 K as a function of mole fraction. An initial alloy composition of X_0 will tend to form a mixture of two concurrent phases (fcc and liquid) to reduce the total Gibbs energy of the system. b) similarly represents this in the Ni-Cu phase diagram, where an initial alloy composition A will tend to form two phases of compositions B and C.

For mixtures, this means that at certain conditions of composition, pressure and temperature, the Gibbs energy of the system can actually be minimi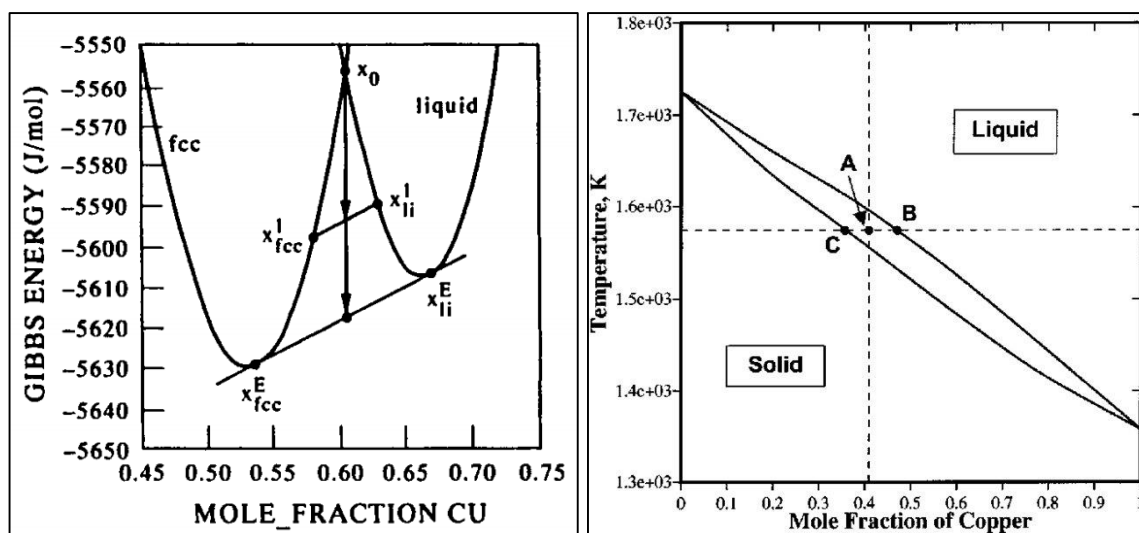sed by forming two or more concurrent phases. Also meaning that the relative amount of each phase can and will adjust to reduce the overall Gibbs energy while preserving the overall atomic composition. The actual composition of these concurrent phases is dictated not by their Gibbs energy minima, but by the common tangent between the phases' Gibbs energy curves.

Using these relationships between Gibbs energies and equilibrium phase composition, phase diagrams for multicomponent systems can be constructed. The actual Gibbs energy curves cannot be analytically determined; but, the thermodynamic properties of the phases and phase transitions can be measured through other means, and from this data the character of the Gibbs energy curves can be found. This approach is known as the CALPHAD method (CALculation of PHAse Diagrams), where a database of thermophysical properties of individual phases is used to analyse multicomponent systems and predict phase diagrams and stability, and is an extremely powerful tool for investigating solution thermodynamics.

Metallic alloys themselves normally involve solid solutions, and as such metallurgical fields make heavy use of CALPHAD calculations to simulate alloy systems and relate experimental data to their thermodynamic (and also kinetic) properties [5]. The impact of kinetics on the evolution of phase composition is a major concern of metallurgy and of CALPHAD simulations. Any phase transformation requires a reorganization of matter; this requires some time and is dependent on kinetic barriers such as lattice migration enthalpies, activation energies and rates of diffusion. Metallurgy exploits this to access metastable material states using heat treatment programs to control the diffusion and thereby the alloy's microstructure and mechanical properties.

Knowing the Gibbs energy curves of the system from their thermodynamic properties, as well as the kinetic barriers involved in phase transformations, numerical calculations can be performed to predict a system's non-equilibrium properties. MatCalc is an applied software to do just that, and with a sufficient database of thermophysical properties and appropriate modelling of conversion processes, can simulate various time dependent processes (e.g. dynamic phase contents [6,7], yield strength curves [8] and even precipitate sizes [7] and dislocations [9]). The Gibbs energy contribution of thermal vacancies and their impact on specific heat capacity can also be considered by the CALPHAD formalism, with their formation entropy being temperature dependent [10–13].

Key here is that the predictive power of CALPHAD simulations is dependent on comprehensive thermodynamic and kinetic data determined through other methods. To improve the predictions and simulations requires improvement and expansion of the known thermophysical properties, with new experimental techniques such as fast differential scanning calorimetry being extremely valuable in this regard.

2.2. PHYSICAL MODELS OF HEAT CAPACITY AND INTERNAL ENERGY

Beyond these thermodynamic descriptions of c_p, fundamental theories, derivations and models of solid state heat capacity have their basis in chemistry and condensed matter physics. As such, they have developed along with modern understandings of structure, bonding and quantization. The Dulong-Petit law (Equation 2.10) based on classical descriptions of particle motion was initially proposed in 1819 [1,14], and does account for the high temperature limit to heat capacity but does not describe the drop observed at lower temperatures.

$$C_{V,\mathrm{m}} = 3R \qquad\qquad \text{Equation 2.10a}$$

$$C_V = 3Nk_B \qquad\qquad \text{Equation 2.10b}$$

Equation 2.10a and 2.10b are written in terms of the fundamental constants which were later discovered; R is the universal gas constant defined in 1874 by Mendeleev, k_B the Boltzmann constant proposed by Planck in 1900. N is the number of atoms.

Revolutionary works from Einstein in 1907 and then Debye in 1912 dealt with descriptions of heat capacity by modelling the internal energy in terms of quantized oscillations. Einstein's model considers the atoms of a solid as an ensemble of independent quantum harmonic oscillators [15], whose total sum energy represents the internal energy, U. Using this approach, one can obtain Einstein's formula (Equation 2.11, 2.12); it describes the temperature dependence of heat capacity, crucially matching the Dulong-Petit law at high temperatures, while also decaying to zero as temperature approaches absolute zero.

$$C_V(T) = 3Nk_B \left(\frac{\theta_\mathrm{E}}{T}\right)^2 \frac{e^{\theta_\mathrm{E}/T}}{\left(e^{\theta_\mathrm{E}/T}-1\right)^2} \qquad\qquad \text{Equation 2.11}$$

Where θ_E is the Einstein temperature with $\hbar$ the reduced Planck constant and ω_0 the oscillator's eigenfrequency:

$$\theta_E = \left(\frac{\hbar\omega_0}{k_B}\right)^2 \qquad\qquad\qquad \text{Equation 2.12}$$

Nevertheless, the predicted heat capacity of the Einstein model depends on $e^{\theta_E/T}$ which decays too rapidly at temperatures approaching 0 K, and was supplanted by Debye's model which correctly predicts the low temperature heat capacity dependence as proportional to T^3 (Equation 2.13, 2.14). A comparison of predicted heat capacities for silver using Einstein's and Debye's models are shown in Figure 2.3.
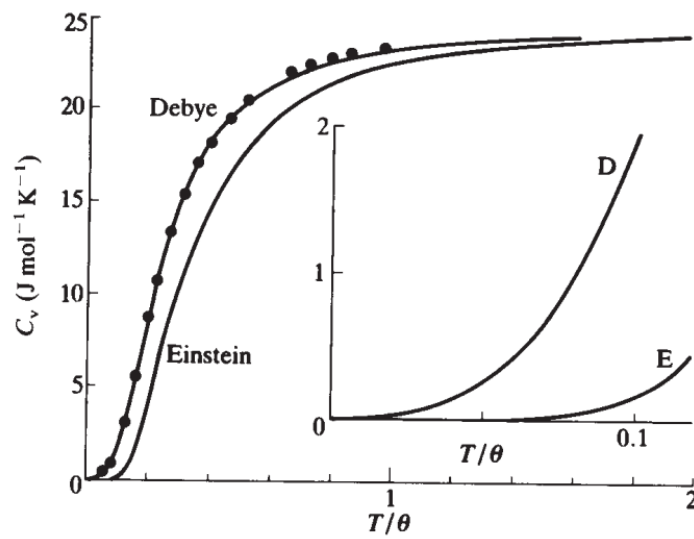
Figure 2.3: A comparison of heat capacities predicted for silver by Einstein and Debye models, including experimental data [16]. Temperatures are shown in terms of the Debye temperature, θ. Both models correctly converge on the Dulong-Petit law at high temperatures, but at lower temperatures the Debye model is clearly superior, correctly exhibiting T^3 dependence near absolute zero.

Debye's theory for specific heat considers the internal energy of a crystalline solid to result from the discrete vibrational modes of confined phonons, analogous to the model of a particle in an infinite potential well. Unlike the particle in a box, the vibrational frequencies are finite, since the phonons must propagate through the atomic lattice, and therefore have a minimum wavelength of two atomic spacings (Figure 2.4). [15]
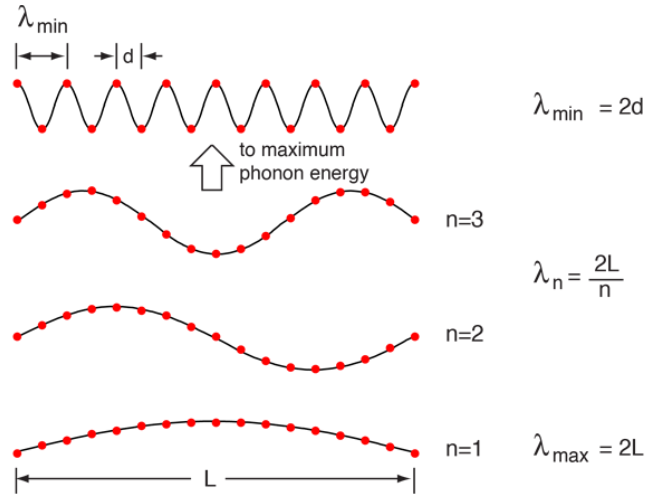
Figure 2.4: Schematic of the lowest and highest energy phonon vibrational modes conceivable for a 1 dimension atomic chain [17,18]. Analogous to the model of a particle confined to an infinite potential well, here the highest cut-off frequency (minimum wavelength and maximum phonon energy) occurs at two atomic spacings. The Debye model determines the energy sum of occupied vibrational states to predict material heat capacity.

The temperature and frequency corresponding to this highest order vibrational mode are termed the Debye temperature (θ_D) (Equation 2.15) and Debye frequency (ω_D) (Equation 2.16). The maximum wavelength (or lowest frequency vibrational mode) is the fundamental between the bounds of the crystal. Using the material speed of sound in determining phonon momentum, and integrating over the density of occupied vibrational states determined from Bose-Einstein statistics, total energy of the phonon vibrations can then be found which represents the internal energy, U. [19]

$$C_{V,\mathrm{m}}(T) = 3Rf_{\mathrm{D}}(T) \hspace{3cm} \text{Equation 2.13}$$

Where $f_{\mathrm{D}}(T)$ is the Debye function,

$$f_{\mathrm{D}}(T) = 3\left(\frac{T}{\theta_{\mathrm{D}}}\right)^3 \int_0^{\theta_{\mathrm{D}}/T} \frac{x^4 e^x}{(e^x - 1)^2}\,\mathrm{d}x \hspace{2cm} \text{Equation 2.14}$$

where $x = \hbar\omega/k_B T$, where $\hbar$ is the reduced Planck constant, ω is the phonon oscillation frequency and k_B is the Boltzmann constant.

$$\theta_{\mathrm{D}} = \frac{\hbar\omega_{\mathrm{D}}}{k_B} \hspace{3cm} \text{Equation 2.15}$$

$$\omega_{\mathrm{D}} = v_s \left(6\pi^2 \frac{N}{V}\right)^{1/3} \hspace{2.5cm} \text{Equation 2.16}$$

Where v_s is the phonon velocity or the speed of sound in the particular solid, N is the number of atoms in the solid and V is its volume. It should be noted that Debye's solid was a cube where phonon velocity is independent of the propagation direction or polarization (there 2 transversal and 1 longitudinal acoustic modes for crystals of two or more atoms). This assumption simplifies the algebraic definitions to one dimension, although phonon polarization can be accounted for using a

dispersion relation and derivatives of this method are still useful for modelling heat capacity and thermal conductivity [3,20]. Although Debye's model is generally less accurate at middling temperatures, correction terms and modifications can improve its predictions.

As a thematic successor to Debye's theory, in place of phonons, the Sommerfeld free electron model considers an ensemble of non-interacting electrons, and incorporates ideas of molecular orbital theory, electronic wave vectors, the Pauli exclusion principle and Fermi-Dirac statistics to express the internal energy, U as the sum of occupied electronic energy states. The electronic heat capacity is then given by Equation 2.17, where T_F is the Fermi temperature:

$$C_V = \frac{\pi^2}{2} \frac{T}{T_F} n k_B \qquad\qquad \text{Equation 2.17}$$

In reality, further contributions to U–for example due to electron-electron orbital interactions and nucleus-electron Coulombic interactions–mean that the Sommerfeld model has some key failings, particularly at higher temperatures. Nevertheless, it describes the electronic contribution to specific heat which is linear with temperature. [23] This can be combined with the phonon contribution to heat capacity for an improved description of c_p's temperature dependence. Often, the heat capacity curves for a material are expressed as; that is, the cubic and linear terms of Equation 2.7 and 2.11 are combined in Equation 2.18:

$$C_V = C_V^{electron} + C_V^{phonon} = \gamma T + AT^3 \qquad\qquad \text{Equation 2.18}$$

where γ and A are material-specific constants, and T is below the Debye and Fermi temperatures. Summing these terms certainly improves predictions of metal heat capacity, though falls short of general consistency largely on account of the omission of particle interactions. By imposing a periodic Coulombic potential to the Sommerfeld model, corresponding to the nuclei at the crystal lattice sites, the "nearly free electron model" is obtained. This gives rise to the arguments of Bloch's theorem, which mathematically describe the quantum states of an electron in a weak periodic potential, and correctly predicts the band structure of metallic materials. [25]

First principle, ab-inito models for a system's internal energy are based on quantum mechanical descriptions of the system, where quantum states are represented by a wavefunction, $|\psi\rangle$ (along with a move to Dirac notation and linear matrix algebra). The system's internal energy U is contained in the solutions to the Schrödinger equation (Equation 2.19).

$$\hat{\mathcal{H}}|\psi\rangle = E|\psi\rangle \qquad\qquad \text{Equation 2.19}$$

$$\hat{\mathcal{H}} = \hat{T} + \hat{V} + \hat{S} \dots \qquad\qquad \text{Equation 2.20}$$

The wavefunction is a complex and unknown function; however, approximate solutions to Equation 2.19 can be sought by building expressions for the Hamiltonian operator, $\hat{\mathcal{H}}$ (Equation 2.20), and for multi electron systems through methods of representing a many electron wavefunction as the product of single electron wavefunctions (Equation 2.21, the Hartree product).

$$\psi(\mathbf{r_1}, \mathbf{r_2}, ..., \mathbf{r_N}) \approx \psi_1(\mathbf{r_1})\psi_2(\mathbf{r_2}) ... \psi_N(\mathbf{r_N}) \qquad \text{Equation 2.21}$$

These single electron wavefunctions can be mathematically arranged in a matrix as a Slater determinant in order to correctly describe the electron's anti-symmetry properties and the Pauli exclusion principle. Without delving into further detail, it suffices to say that the terms of the solutions of the approximated Schrödinger equation provide the various contributions to internal energy, U, such as kinetic energy and electrostatic potentials. Further contributions to U can also be found by including their appropriate operator in the Hamiltonian; electron spin interactions for instance, which are responsible for magnetic ordering, can be accounted for by the addition of a spin operator, $\hat{S}$. [26]

These arguments are the basis for modern ab initio calculations such as the Hartree-Fock or self-consistent field method, where iterative calculations produce results which converge on some precise and hopefully accurate value. Advances in computational power mean these iterative calculations can be performed at great speed and on ever more complex atomic arrangements. Hartree-Fock methods have been at least partially superseded by Kohn-Sham equations and density functional theory (DFT), which sidesteps the difficulties in approximating the many electron wavefunction by dealing instead with its square, which is the electron density distribution. This electron density is spatially dependent, and is shaped by the potential energy landscape created by the atomic nuclei (which in turn are affected by the electron density distribution). The complex Coulombic and quantum mechanical interactions between electrons are considered in descriptions of exchange-correlation potentials [28,29], and their inclusion can improve predictions of the *ab-initio* calculations in DFT [22]. Though the scope and applications of DFT and time-dependent DFT go far beyond descriptions of heat capacity [21,22], determining electron density and orbital shape during inter- and intramolecular interactions, the energy and physical structure of a system's state is at its core, which must also encompass the nature of heat capacity.

All these varied theoretical models for determining the energy stored in a system, while certainly not comprehensive, should demonstrate that our understanding of heat capacity is intricately bound to our knowledge of internal energy and solid state physics; the theory of one requires a theory of the other. When the theory of heat capacity can describe the truth in every observable sense, most questions of condensed matter physics should be answerable. As such, continuing the measurement and fundamental investigation of heat capacity is hugely important to our understanding of matter at every scale, and measurements of c_p are essential to research at the frontiers of materials science and metallurgy in general. It correlates with crucial material properties from thermal conductivity and enthalpy, to crystal structure, electronic structure and fundamental particle interactions, and has major implications on engineering and industry, where metallurgical heat treatments are ubiquitous and temperature dependent properties must be known.

2.3. CALORIMETERS AND DIFFERENTIAL SCANNING CALORIMETRY

Experimental determination of heat capacity is broadly achieved through thermal analysis using a calorimeter. With its roots in the second half of the 18th century and Lavosier's *Elements of Chemistry* [24], calorimetry has evolved along with technology and electrification for repeated innovation in all aspects of its instrumentation: sensing; recording; isolation and controlled environments; standards and references; automation; and calculation have all progressed with the state of the art, with today's user end software simplifying much of the experimental process. Nevertheless, the fundamental functionality of the calorimeter is much the same: precise and accurate measurement of temperature and heat exchange during a chemical or physical process.

In modern differential scanning calorimeters (DSCs), through precisely controlled heating methods and monitoring of precise electric thermocouples, materials are subjected to dynamic temperature changes [27]. Cooling in these devices occurs through controlled heat dissipation, often aided by the flow of cold, inert gas in and around the sample chamber. Power-compensated DSCs use twin furnaces, where one is left empty or contains a reference material and one holds the sample, and the device sensors record the difference between the two during user defined heating and cooling programs. This differential approach improves sensitivity and signal fidelity, since the impact of the furnace on the signal is largely negated. Power-compensated DSCs (shown by a simple schematic in Figure 2.5) operate on this principle, while also regulating the heat supplied to the system such that a defined temperature change is realised in the sample.
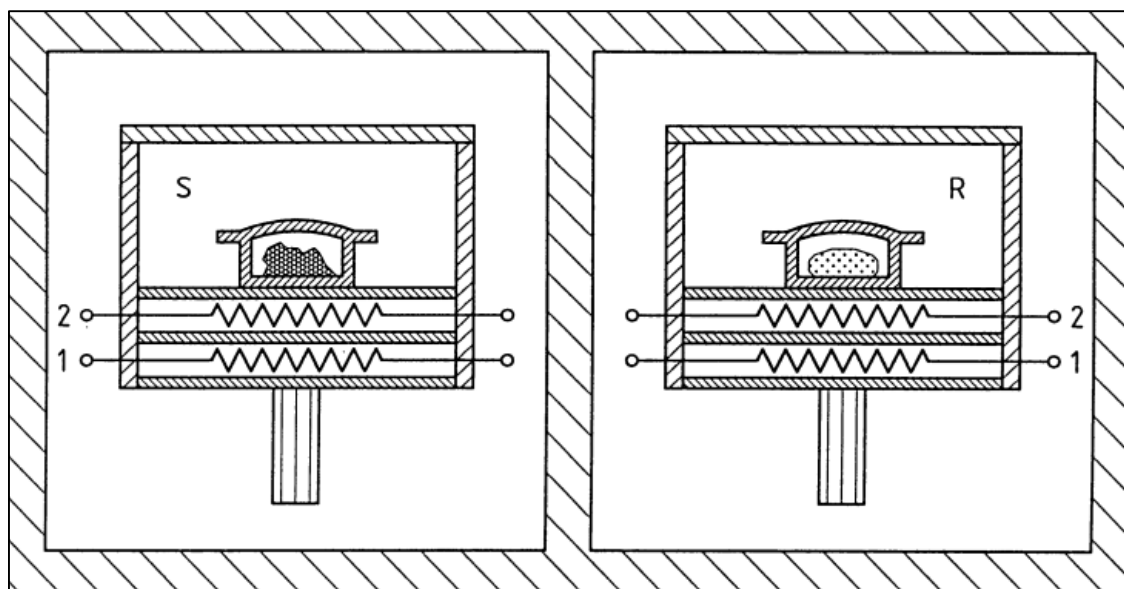
Figure 2.5: Simplified schematic model of the twin furnaces of a power compensated DSC [27]. "S" and "R" indicate the sample and reference furnaces, "2" labels the electric thermocouples and "1" labels the resistance heaters. The electrical current through "1" is regulated to elicit a defined temperature change, and the difference in power between the sample and reference sides is recorded for evaluation.

The resultant signal in Watts is temperature dependent, and describes precisely the heat supplied to the system during the programmed change. In principle this can be evaluated to determine *any*

thermally impactful material change, though the realities and sensitivities of these devices make the characterisation of some phenomena simpler than others. Outside of phase transitions, determining heat capacity from DSC measurements is fairly straight forward knowing the sample mass and programmed heating rate [30]. For metallurgy, and where metallic alloys are concerned in particular, the specific heat capacity is not the only significant parameter affecting the measured signal and in most cases heat can elicit rather more complicated material changes. Alloy properties can be significantly affected by temperature due to solid state diffusion and changes in the metal's microstructure [11]. Nevertheless, the heat capacity itself can be a very informative parameter in describing the nature of the metallic bonding and crystallographic structure of the material [16].

In the case of calorimetric measurement on metallic alloys, the arguments outlined in Section 2.1 become incomplete, due to additional enthalpy changes as a result of phase changes and solid state diffusion phenomena (e.g. precipitation, dissolution, grain coarsening, dislocation relaxation). These result in additional release or consumption of heat in the system while also changing the state of the alloy, and are highly dependent on the composition and diffusion kinetics in the material [11]. These enthalpy changes of course affect the heat supplied by the calorimeter and therefore the output signal. While solid state diffusion in metallic alloys occurs rapidly at temperatures near their melting point, for most mechanically relevant alloys, the rate of diffusion is significantly reduced at ambient temperatures. This means that temperature and thermal history are hugely impactful on an alloy's thermophysical properties. If sufficiently high heating and cooling rates are involved, diffusion phenomena at high temperatures can be reduced, simply as there is less time for diffusion to occur [31].

Due to the generally rapid diffusion kinetics in metals, the heating rates required to suppress such phenomena can be in the thousands or tens of thousands of degrees per second [32–34]. Useful access to such rates with a calorimeter is however limited by the physical conditions of the experimental setup because of how quickly and precisely heat must be transferred to and from the system. To reach these rapid rates, a major reduction in the system's thermal mass is necessary, which a move to micro electro-mechanical systems (MEMS) accomplishes, explained in more detail in Section 2.3. Briefly, precision circuit fabrication allows for the production of MEMS microcircuitry that mimics the twin furnaces of a conventional DSC, and offers high consistency between circuit sides, which is of critical importance for the performance of DSC's differential setup [35].

Aside from more rapid rates, the control offered by electrical heating and sensing allows more complex control of temperature program design. Using conventional DSC devices, temperature modulated DSC (TMDSC) proposed in 1993 [36] operates by modulating the normal linear heating rate with a superimposed sinusoidal function. If this is done at sufficiently low rate, and sufficiently low temperature oscillation amplitude [37], the reversible and irreversible parts of the sample heat flow can be separated out of the measurement. This allows for more precise analysis of the thermal processes occurring in the sample by helping to separate overlapping phenomena. Although the technique came under some scrutiny [37–40], it was successfully used to measure heat capacity [41].

A generalized theory of TMDSC along with a more advanced evaluation procedure was proposed in 2006 [42,43], and today it finds widespread use throughout materials science. Polymers and resins are frequently examined using TMDSC [44–48] since it can separate overlapping phenomena in the heat signal, for example around the glass transition. This provides much better clarity than conventional DSC curves for analysing the crystallisation and melting processes occurring [47–49], and has even been used to examine thermal degradation [50,51]. In combination with other thermal analysis techniques, for example dilatometry, thermal gravimetric analysis or laser calorimetry, characterisation can be even more effective [52] with tailored experiments to suit the material and phenomena in question.

2.4. MICRO-ELECTROMECHANICAL SYSTEMS (MEMS)

New technologies are of course indispensable for broadening the scope of what can be measured, and improving the accuracy, precision and control is essential for the best analysis and characterisation. Micro-electromechanical systems (MEMS) encompass a vast array of small electronic devices, and since their conception in the 1990s have been rapidly developing, with a lot of technological interest and several textbooks dealing specifically with MEMS [35,53–55]. They find numerous technological uses in scientific fields, with a few of the many examples being in biomedicine and biotechnology [56], as chemical sensors [53], as gyroscopes, accelerometers and pressure sensors in engineering, navigation and even smart phones and mobile consumer devices. They are popularly fabricated with technologies and process routes from the integrated circuit (IC) and silicon wafer industry, and can include actuators as well as thermally, magnetically, chemically or optically sensitive components.

Silicon and silicon nitride (SiN_x) membranes are frequently used since they offer good rigidity at thin film geometries and their precision processing is well established in the electronics industry, being suitable for some key fabrication techniques such as photolithography, reactive ion etching (RIE) and various methods of thin film deposition. Using these techniques, electrical traces and microcircuitry can be constructed on a silicon wafer substrate to produce batches of highly sensitive and highly consistent MEMS devices. The manufacture of one such MEMS sensor is described in [57] with a schematic figure, included here as Figure 2.6. There, by applying and patterning photoresistive layers, and depositing and etching layers of material, a Ni metal strip was constructed on a silicon nitride membrane. These strips were connected to metal contact pads to which electrical contacts were attached. The voltage and current through the strip could then be monitored to determine the characteristics of the system.
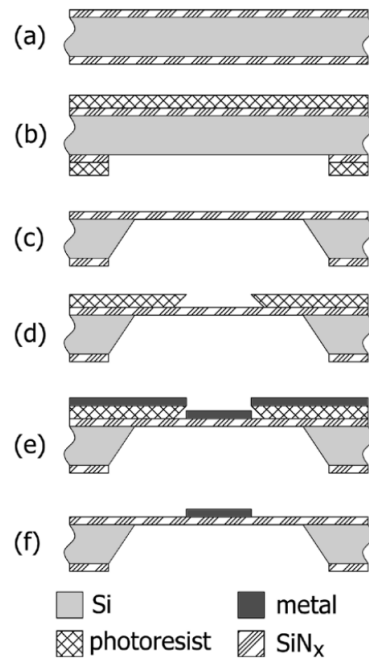
Figure 2.6: Schematic cross section of the process route for construction of a MEMS heating device [57]. Using a procedure of applying and patterning photoresist layers, etching and deposition, a metal strip is constructed on a silicon nitride membrane.

More complicated MEMS heaters have also been developed as solutions to the challenges of environmental transmission electron microscopy (ETEM); a contribution from 2008 [58] features the construction of a windowed measurement cell, its schematic cross section shown in Figure 2.7, and encapsulates a small volume in a serpentine gas channel between two silicon dies. Sample material can be placed in its center while gas flows around and past it at pressures over 1 bar. A serpentine Pt heater controlled the temperature, and electron transparent "viewing" windows in the silicon nitride membrane allowed for high resolution TEM characterization.
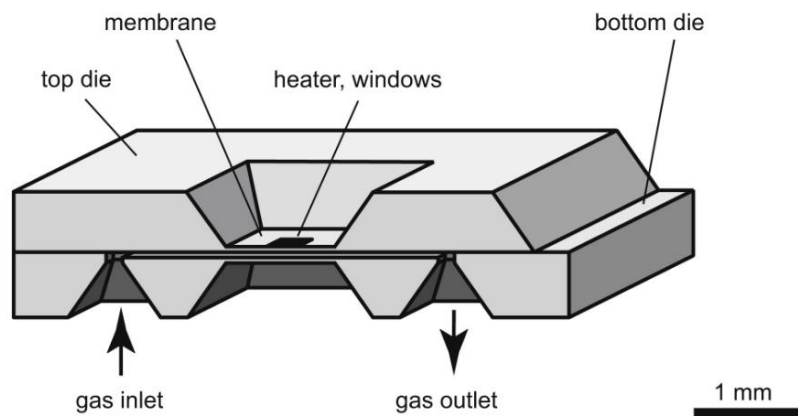
Figure 2.7: Schematic cross section of a MEMS chip for environmental TEM [58]. A long, serpentine gas channel is encapsulated between to silicon dies, along with a Pt heater. Gas flows through it and over sample material, enabling TEM characterisation at pressures over 1 bar.

Some of the more involved MEMS applications deal with microfluidics for "lab-on-a-chip" devices, which itself is an umbrella term for a broad array of MEMS-based experimental tools [59,60]. One

approach to this uses machined micro-channels in a substrate to direct microliter volumes of fluids along a MEMS membrane, tripping various sensors along its path. To overcome frictional forces of microfluidics, some driving force is needed [61], with one such solution being the incorporation of piezoelectric actuators [62,63]. PiezoMEMS devices see research for various actuator applications such as acoustic resonators, stress sensors, as levers and switches [64,65] and indeed for microfluidic pumps and microvalves [63,66].

Modern technologies can make use of MEMS devices wherever precision electronics can be exploited, hence its already numerous applications. Their development is multidisciplinary, their utilisation, broad, and their potential continues to increase. By integrating precise sensing for small samples with high temporal resolution, transient and metastable material states can be investigated in ways not otherwise possible for bulk samples. With surface and interfacial effects becoming more significant at this scale, MEMS experiments can be extremely useful in analysing micro- and nano-scale phenomena, and help drive material science to new heights.

2.5. FAST SCANNING CALORIMETRY

Modern calorimeters used for scientific analysis all involve a sample stage or container, and a furnace controlled by electronic heaters and thermocouples, but modern circuit fabrication capabilities have made such arrangements possible on a much smaller scale. With sufficiently small samples, calorimetry can be done at much higher rates with unprecedented precision [34]. The so-called fast scanning calorimetry (FSC) does nevertheless have its limitations which result from sensor materials, sensitivity of electrical components and the mechanisms of heat transfer [67].

The earliest fast scanning calorimeters using MEMS technology came about through the work of Denlinger et. al. in 1994 [68] and also Lai, Ramanth and L.H. Allen in 1995 [69], and described the construction of a thin film scanning micro-calorimeter. In [69], a silicon nitride membrane was manufactured with a thin film nickel heating element. Sample material, which were layers of deposited tin, was deposited to the opposite side of the membrane and calculated to be within 1 degree of the Ni heater. This means the Ni functions both as a resistance heater and a thermometer, and its temperature can be calculated from resistance values by measuring the voltage and current. With such an experimental setup the addenda heat capacity of the system is extremely low, allowing heating rates around 30,000 K s^{-1} to be realised. This is over 1000 times faster than conventional DSC methods [70] and sufficiently high to approach adiabatic conditions. Knowing the temperature and the heat output of the Ni heater, the temperature dependent heat flow curve could be evaluated to determine sample heat capacity and the enthalpy of fusion.

Development of similar thin film micro- or nano-calorimeters continued over the next decade [71–73], and in 2003 an influential work (by Olsen, Efremov, Zhang, Zhang and L.H. Allen) [57] shared the construction of the first differential-type scanning calorimeter based on MEMS technology (Figure

2.4). With a nickel strip still acting as the heater and thermometer, it featured twin heaters on separate circuits which function like the two DSC furnaces. This differential arrangement allows for better electrical precision, taking advantage of the consistency of manufacturing using photolithography and chemical vapour deposition [27,35,74]. Already at the that time, the authors discuss the sensor design for its effectiveness in TEM measurements and use it to characterise their samples ex-situ.

FSC has continued to be extensively used in the study of nucleation, metastable phase transitions and glass formation, where rapid kinetics have hindered characterisation with other calorimetry techniques. Polymers for instance have been widely investigated with FSC [75–78], as have more recently bulk metallic glasses (BMGs) [79–81]. Phase transformations for some BMGs can proceed much slower than conventional alloy systems, only compounding the advantages to characterisation offered by FSC's temporal resolution. A solid-solid phase transformation in a Au-based BMG was investigated in 2016 by FSC and revealed to in fact occur via an intermediate liquid state [82]. This was previously observed in polymeric colloidal particles, whose properties have many parallels to atomic ensembles (albeit with much slower kinetics). Where the rapid kinetics of metallic systems would normally obscure this mechanism, MEMS-based FSC in this case offered a unique means to detect this intermediate melting, which is thought to be a general feature of solid-solid phase transformations [82].

Alloy investigation can in general benefit greatly from the rapid temperature control possible using a MEMS-based approach. By nearing or exceeding the material's critical cooling and heating rates, nucleation mechanisms and even metastable states can be examined [32,83] for material characterisation at the frontiers of metallurgical investigation. Analysis is frequently done by observing trends in the measured curves as they are impacted by temperature, thermal history, and the specific material kinetics.

2.5.1. METTLER-TOLEDO FLASH DSC

Mettler-Toledo's contributions to the field of FSC have revolved around their commercial Flash DSC devices. Fundamentally a power-compensated differential scanning calorimeter, their Flash DSC 2+ is comprised of an isolated sensor support which is mounted with disposable MEMS chip sensors (Figure 2.8). These hold the sample material and contain the dual "furnaces" needed for DSC with electrical heaters and temperature sensors leading to electrical contact points. The aluminium sensor support (see Figure 2.8b) acts as a heat sink to stabilise temperature, and the whole measurement cell is cooled by inert gas flow (e.g. argon) through an intracooler. The chips are placed onto spring mounted gold pins which act as electrical contacts for the sensor electronics. The measurement cell is accessed by sliding back the insulated lid. If reaction with oxygen or other atmospheric components is a concern, an additional cover can be screwed over the mounted chip to prevent gas exchange with the surroundings and improve isolation. A microscope above the chip mounting area allows for samples to be placed directly on a mounted chip.
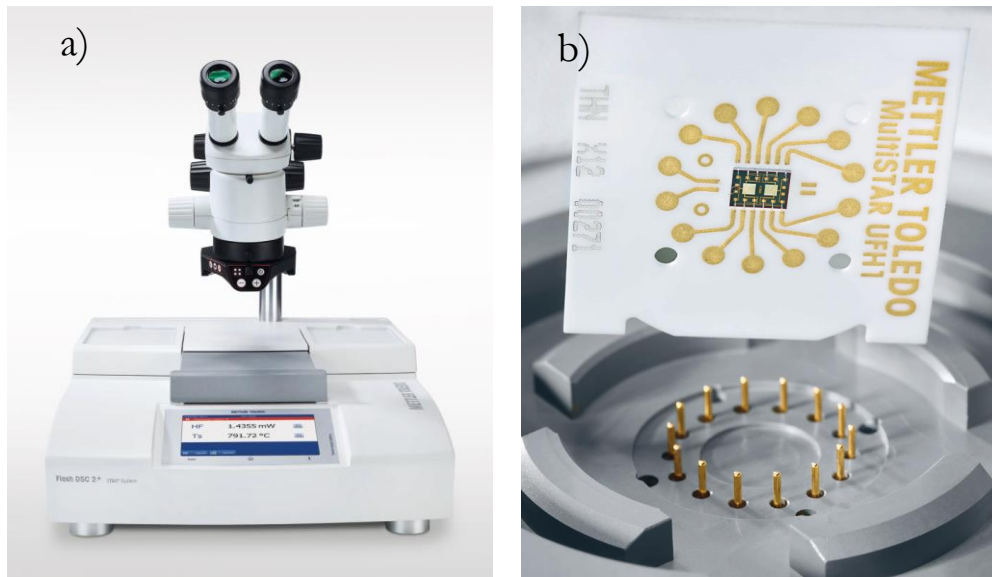
Figure 2.8: (a) a fast scanning calorimeter, the Mettler-Toledo Flash DSC 2+; (b) a MultiStar UFH 1 high temperature chip sensor where it mounts to the gold contact pins protruding from the sensor support [84]. The twin DSC furnaces can be seen in the middle of the sensor.

2.5.2. MULTISTAR UFS 1 AND UFH 1

Housed on a ceramic plate, the MultiStar UFS 1 and UFH 1 chip sensors comprise a silicon-nitride (SiN) membrane lain with electrical heaters and thermocouples. For both the DSC chip's "furnaces", these are arranged around the sample area, a centre region of the membrane which has a thermally conductive metal layer within the SiN. Since the membrane thickness, the electrical components and their arrangement, and the metal layer all differ, the two sensor types perform differently. A schematic of the UFS 1 sensor is shown in Figure 2.9 [84], and their key specifications are listed in Table 1 [85].

1. Ceramic plate
2. Silicon frame
3. Connecting wire
4. Resistance heater
5. Aluminum plate (sample area)
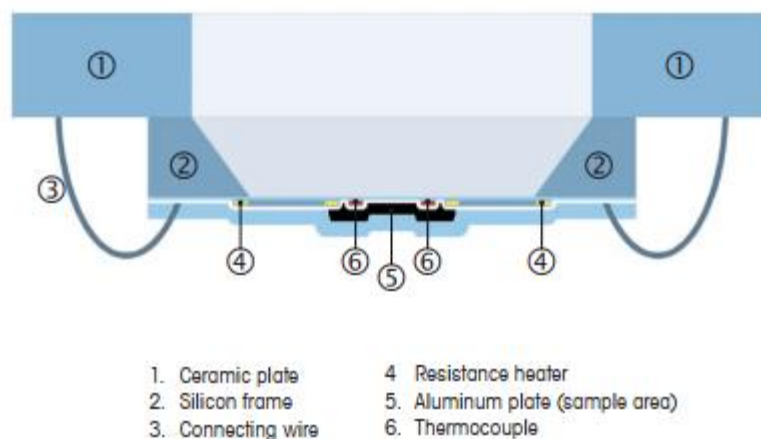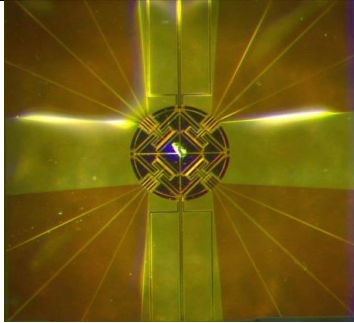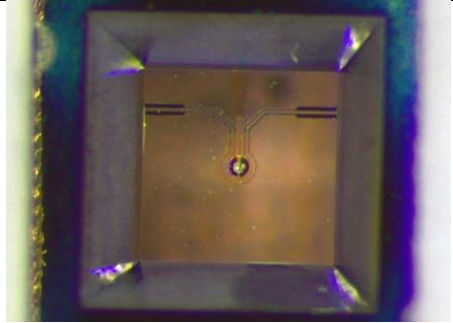6. Thermocouple

Figure 2.9: Schematic cross section of a MultiStar UFS 1 chip sensor [84]. Essentially similar to the DSC furnaces in Figure 2.5, electrical components are integrated into a SiN membrane on which a sample is placed.

Table 1: Technical details of the MEMS chip sensor used with the Mettler-Toledo Flash DSC 2+ fast scanning calorimeter [85].

	MultiStar UFS 1 (low temperature)	MultiStar UFH 1 (high temperature)
Membrane	Silicon nitride	Silicon/silicon nitride
Thermocouples	16	4
Signal time constant	1 ms	0.2 ms
Sample area dimensions	500 μm	100 μm
Sample mass	Polymers, Organics: 5-400 ng Metals: 100 ng-10 mg	Polymers, Organics: 5-100 ng Metals: 50-1,000 ng
Operating temperatures	–95 °C to +500 °C	–95 °C to +1000 °C
Cooling rates	–0.1 K s^{-1} to –4000 K s^{-1}	–0.1 K s^{-1} to –40,000 K s^{-1}
Heating rates	+0.1 K s^{-1} to +40,000 K s^{-1}	+0.1 K s^{-1} to +50,000 K s^{-1}
Max. heat flow signal	20 mW	20 mW
Noise	rms<0.5 μW (typical)	rms<0.5 μW (typical)
Sampling rate	Max. 10 kHz	Max. 10 kHz
Temperature resolution	2.5 mK	7.5 mK

2.5.3. MEASUREMENT OF THE SAMPLE-SENSOR SYSTEM

While the quoted specifications for the MEMS chips are broadly true, sample parameters such as mass and also geometry can have a significant impact on their baseline performance because of the comparative thermal mass of the sample and the sensor [70] (small addenda heat capacity from the sensor membrane). Systematic heat losses are also highly dependent on the sample and on the experimental conditions, e.g. the temperature and type of purge gas. Modelling the thermal gradients and temperature distribution of the sensor can have implications on ideal measurement conditions and be of value for certain precise examinations. Flat and thin samples have good thermal contact and are normally preferred for this reason, but a large interfacial contact with the membrane could potentially cause deleterious effects; stresses induced by quenching can perturb the resistivity of the membrane heaters, and in some cases, the SiN membrane may also be considered a potential contaminant (for example by diffusion into aluminium forming nitrides or silicides), though effects like this are dependent on the specific material. For these reasons, the following Chapter 3 discusses in some detail the experimental approaches to FDSC undertaken throughout this thesis' investigations, but many excellent accounts can be found in the literature, with several notable contributions from Christoph Schick et. al [70,86,87]. Characterisation through other means can also be very valuable, with

contemporary works making frequent use of microscopy techniques, and even nano-indentation, thermal imaging, and x-ray diffraction.

2.6. MEMS HEATERS FOR IN-SITU TRANSMISSION ELECTRON MICROSCOPY

Built for in-situ heating experiments within a TEM, Protochips Fusion: Select e-chip is another MEMS chip sensor with a SiN membrane. A 3x3 grid of holes is constructed in the membrane on which a sample is placed, shown in Figure 2.10. The heating is controlled by passing current through the membrane [89], and a calibration file relates the measured resistance to temperature [88,91]. The sensor is mounted to a holder and the sample can then be characterized wherever it lies over a hole using normal TEM characterization methods. From room temperature, up to 1200 °C can be reached with control of isothermal and dynamic temperature programs [88]. Examination of nano- and atomic-scale phenomena is then possible during heating [90].
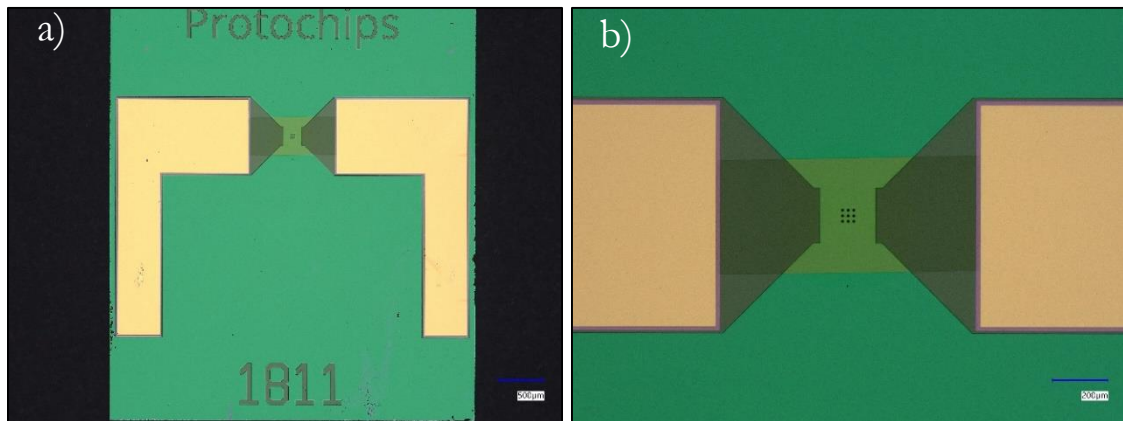

Figure 2.10: Light microscope images of the Protochips Fusion Select e-chip. (a) shows an overview of the whole chip sensor and b) showing the grid of 9 holes over which a sample would be placed.

Figure 2.11: Protochips Fusion Select holder for TEM, clearly showing the comb of electrical contacts touching the e-chip [88]

Melting is not a crucial for TEM characterisation, and so the scope of possible materials for such experiments is perhaps broader that of FSC, which relies on melting to establish efficient thermal contact with the sensor. Almost any electron transparent sample can be observed in the TEM; though image contrast and atomic mass must be taken into account, complex and varied metallic systems have been subject to in-situ TEM analysis using MEMS. From solid state batteries [92], to phase change materials [93], nanoparticles [94] and nanowires [95]. Nevertheless, sample preparation for such experiments present recurring and unique challenges which have often required innovative solutions. A focused ion beam (FIB) is normally the method of choice for sectioning appropriate pieces from the microscopic or macroscopic sample material.

Contrary to the FDSC sensors discussed, the temperature control and reporting for the Fusion Select e-chips is not so precise, relying on resistivity calibration files to determine the temperature of the sensor rather than an arrangement of heaters and thermocouples, and this being dependent on the electrical and thermal parameters of the sample-sensor system [96]. They are better provided for enabling in-situ TEM by their thinner membranes and holes [89]. Other MEMS sensor solutions have involved free standing cantilevers in the membrane to deal with the issue of occurring sample stresses [97].

3. MATERIALS, METHODOLOGY AND APPROACH

As a relatively young discipline, experiments using MEMS often present new and unique problems relating both to a system's chemical properties and to the physical practicality and feasibility of the experiment in question. Due to the delicate nature of microcircuitry, with MEMS chips designed to be highly sensitive, sample preparation and general measurement setup can have major impacts on the quality and performance of MEMS-based experiments. The high precision measurements of this thesis examine metallic systems, which offer diverse sample preparation options owing to their formability. In addition to the physical conditions of the experimental setup, experimental design and various analysis techniques help to ensure high quality measurements. This chapter covers in a general way the numerous approaches to sample preparation and measurement which were undertaken in the course of this thesis's investigations, though many excellent and comprehensive contributions can be found in the literature of the past two decades [70,86]. MEMS sensors are highly capable under the right circumstances, and optimising all aspects of experimental conditions is key to successful measurement and taking full advantage of our available technology.

3.1. SAMPLE

3.1.1. STARTING FORM

The morphological state of the sample material is crucial to its preparation and can be majorly impactful on the quality of MEMS-based experiments. Thin film deposition provides the ideal geometry for reducing thermal gradients and maximising thermal contact, and allows good control and uniformity for the sample; however, it is not universally appropriate. To study metallic alloys, it is normally desirable to prepare samples of appropriate size from the bulk material. Metallic foils can be sectioned with a scalpel, while powdered metals can be sampled by taking an individual particle. Metal ingots can be shaved to obtain sample sized material, though due to compositional variations resulting from casting, the homogeneity offered by melt spinning ingots into foil or atomizing into powders may be a better choice.

3.1.2. MELT SPINNING

Melt spinning creates a rapidly solidified thin metal ribbon from bulk material. The rapid solidification results in better homogeneity, a clear benefit for sample sizes below 100 μm, while the resulting foil ribbon is convenient for further sample preparation. As part of a collaborative work [98] (included in Chapter 10), melt spinning was performed at the Erich Schmidt Institute on a eutectic AlCu ingot, which was cast in-house at the Chair of Non-ferrous Metallurgy. Pieces of the cast ingot could be cut and inductively heated in a quartz tube under argon atmosphere. When fully molten, the alloy can be pressure ejected down through a small nozzle in the glass tube onto a large rotating copper wheel (Figure 3.1). The stream of molten metal rapidly solidifies as it contacts the copper wheel, and is flung

sideways into a collection hopper. If the nozzle diameter, ejection pressure, melt temperature and wheel speed are correctly balanced, several meters of continuous metal ribbon can be produced. While the procedure is relatively quick, a few attempts are normally required before finding the optimal ejection conditions to obtain the foil ribbons, and optimisation of processing parameters has been keenly investigated [99].
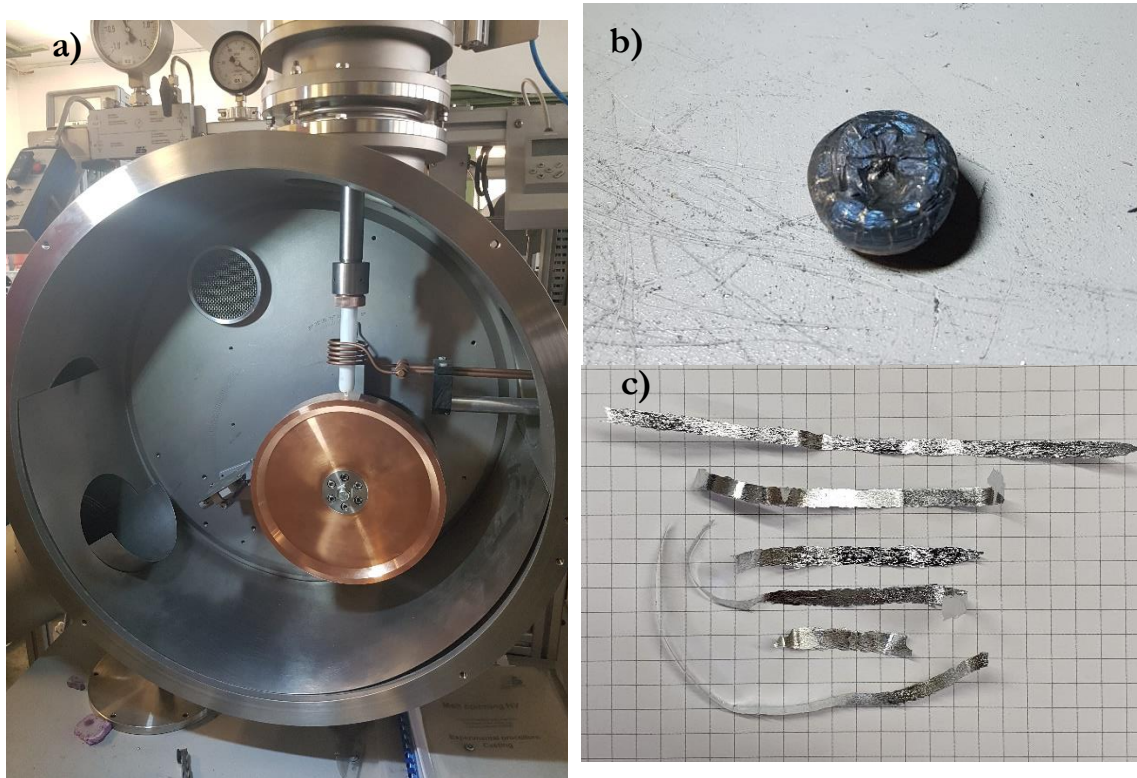

Figure 3.1: (a) shows the melt spinning apparatus with the rotating copper wheel in the centre, the induction heater and test tube furnace above this and the collection chute to the left. (b) shows a failed run, where the alloy melt was not ejected from the quartz tube and (c) shows the AlCu ribbons collected from a successful attempt.

3.1.3. POLISHING

To achieve electron transparent samples for use in a TEM, metallic foil can be electro-polished [100,101]. Small disks (normally 3 mm in diameter) are punched out from foil, or ground down to 120 µm from the bulk ingot, and electrochemically thinned. In twin jet electropolishing (JEP), a voltage is applied through a flat foil sample under an electrolyte flow (Figure 3.2). As the surface metal atoms continually dissolve via a redox reaction, eventually voids will appear in the foil causing trigger of a light sensor and stopping the applied voltage. The sample material adjacent to the foil holes gets extremely thin, being partially transparent to electrons and therefore suitable for TEM characterisation. The electrolyte, temperature, voltage, current density and sample morphology significantly impact the progress of the reaction, and therefore the quality of the electropolishing [102,103]. For this reason, some trials and fine tuning of these parameters may be required for sufficient quality samples. Aluminium is found to be well suited to jet electropolishing [103].
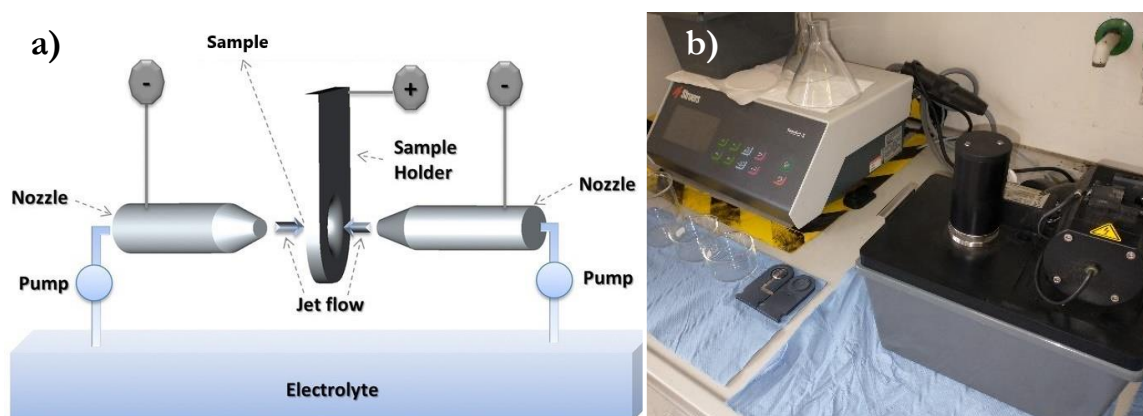
Figure 3.2: a) Schematic [104] and b) the utilised jet electro-polishing (JEP) apparatus for thinning foil samples like 3 mm discs. Twin jets of liquid electrolyte are applied to the sample along with a voltage to dissolve the metal and create voids in the foil. A light sensor terminates the reaction when the voids appear. Adjacent to these holes the material is electron-transparent.

If the disk surface is uneven before polishing, the transparent regions around the electro-polished voids may be negatively affected [105]. Melt spun foil of eutectic AlCu was found to suffer from this, so pieces of the ribbon were first polished using diamond grinding paper [98]. The 3 mm disks then punched out yielded better samples, as polishing a more even surface mean the electron transparent regions tend to cover a larger area, and sample preparation is more forgiving. Reaching electron transparency in this way is relatively non-invasive compared to ion polishing, and avoids FIB induced artefacts [106].

3.1.4. CUTTING AND SAMPLE SECTIONING

Samples can be precisely sectioned from foil using a scalpel under a microscope. A curved steel blade (No. 10 type) provides better control than a straight one, as the intended cut can be aligned with the blade tip in contact with the cutting surface. Firmly lowering the blade from this position down through the foil, depicted in Figure 3.3, performs the intended cut with relative ease. Precise sectioning methods become particularly relevant for samples destined for use in a TEM, since those samples require electron transparency found only adjacent to the foil's electropolished voids. Care should be taken to keep track of the region of interest during cutting, with image capture from the microscope being sometimes useful for this. As a cutting surface, microscopy glass slides are a convenient option as they are stable and easy to handle underneath a microscope; however, silicon glass can easily scratch under a steel blade creating particles which clutter the slide surface and potentially contaminates the sample material. Polished sapphire slides (30x50 mm) have proved to be a better cutting surface due their higher hardness. Finally, where consistency between sample geometry is a concern, scalpel sectioning can be wholly avoided by using metallic powders.
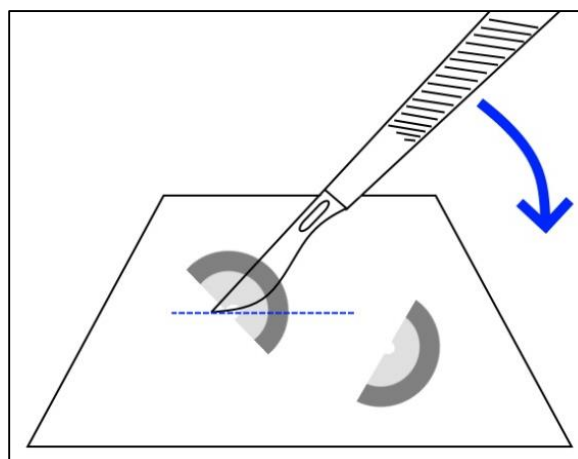
Figure 3.3: Schematic procedure for sectioning foils using a curved scalpel. Stabilising the scalpel by resting the tip on the cutting surface, the intended cut can be aligned. For samples destined for TEM, the edge of an electropolished void is desired for its electron transparency.

3.1.5. SAMPLE POSITIONING

To avoid damaging the fragile SiN membranes while manipulating the sample into the correct position on MEMS chip sensors, an animal hair stylus is used. Attaching a single strand of fine hair, e.g. from a watercolour paint brush, to a pen-like handle allows the dexterity to manipulate the sample under a microscope. The hair's flexibility prevents undue mechanical stress on the membrane, while its tapered end gives a precise point to push the sample around.

Wetting the membrane surface with a small amount of oil can also assist in sample positioning and improving thermal contact. Silicon oil is frequently used in FSC, though vegetable oils such as peanut oil are also possible providing they can be removed by heating to leave little to no residue. Due to the oil's viscosity, it acts somewhat like an adhesive, preventing the sample too-easily leaving the membrane surface, and can be useful in cases where the sample frequently jumps away on heating. Spherical powder of Al alloys was found to be particularly prone to sample hopping before the first melting can establish a mechanical contact with the sensor membrane. As the sensor heats and cools, its membrane visibly flexes, not unlike a drum skin. This, combined with the thermal expansion of metallic samples, means they were often found to jump away from their original position, and had to be manipulated back to the membrane's sample area using the hair stylus. Utilising a lower heating rate (50 K s^{-1} for example) to accomplish the first few melting-solidification cycles is preferable to reduce the need for repeated sample positioning.

3.2. SENSOR

3.2.1. PLASMA CLEANING

To remove potential contaminants such as carbon, plasma cleaning of the chips can be performed. A custom holder was machined to suit the dimensions of the FDSC chips and plasma cleaner, shown in Figure 3.4.

Figure 3.4: a) Plasma cleaner from Diener electronic GmbH with a custom holder for MultiStar FDSC 1 chip sensors. The holder (b), where chips are placed onto rubber O-rings and two small anchoring posts.

3.2.2. SPUTTERING AND COATINGS

The inherent flex and movement of the membrane and sample as a result of thermal expansion can change the heater resistivity and affect the measured signal [67,87], which may be impactful in particular cases, and should be considered in high precision measurements. In [87] a thin gold leaf between the sample and sensor is used to avoid these stresses. Sputtering and coatings may also be used to affect the sample-membrane interface, though have some potential to contaminate the sample. Graphite sputtering for example was performed on FDSC sensors to reduce wetting and therefore mechanical binding. Nanoparticle coatings also have the potential to reduce tension at the sample/membrane interface. Using a precision pipette, a small drop (e.g. 4 μl) of an appropriate dispersion was applied to the MEMS sensors and allowed to dry, leaving behind a solid residue of nanoparticles. The samples could then be placed as usual onto the sensor for measurement. These approaches of course introduce potential contaminants, and impact with the thermal gradients of the sample-sensor system, and these interactions should be considered in each case.

3.3. FDSC EXPERIMENTAL DESIGN AND ANALYSIS

3.3.1. THE TEMPERATURE PROGRAM

While sample preparation should be given full attention, still more important are the strategies of experimental design and evaluation. For FDSC, with cyclic temperature programs so easy to implement, experiments can quickly generate dozens of equivalent curves. These can be averaged to greatly reduce noise in the signal. Averaging 3-10 cycles was found to be most effective, as long as the curve consistency is sufficient, since the majority of the possible noise reduction is achieved in this range. Metals are often well suited to such experiments, certainly for investigations on precipitation and heat treatments, since the sample state can be repeatedly reproduced and measured with the appropriate temperature program. Collections of curves can then be quickly compared to examine

trends in sample heat flow to analyse the underlying kinetics. The interrupted quench programs detailed by Milkereit et al. [31] are an excellent example of this approach to experiment design, where the continuous cooling precipitation (CCP) diagram. While the program's specifics are wholly dependent on the system of study, some features can be generally applicable to classes of materials (e.g. glass formers [80]), or to the parameter of interest (e.g. undercooling [107]).

Minimising high temperature operation can be beneficial for sample and sensor stability, as high temperatures fatigue the sensor and will eventually cause damage [108], requiring a fresh sensor. Avoiding needless repetitions can be useful here, where consistency between curves is sufficient, as can programming short isothermal segments (e.g. 0.01 s). Below ~850 °C, the stability of the UFH 1 sensors was found to be very good, and generally well sufficient to complete an intended suite of measurements.

3.3.2. THE HEAT FLOW SIGNAL

During a temperature increase, the heaters of the MEMS sensor are activated, dependent on the sample's thermal mass and the programmed rate. However, since heat is lost continually from the system (e.g. to the cold inert gas, through the membrane and sensor support or as radiation), the FSC heaters must also compensate for that, even during isothermal and cooling segments. These heat losses are temperature dependent and unique to the sample-sensor system, meaning a blank correction using an empty sensor is not possible [70,109,110]. For FDSC, the signal from the power differential, ϕ_{diff} can be written as Equation 3.1: where ϕ_{loss} are the systematic heat losses; m is sample mass; c_p is specific heat capacity and β is heating rate.

$$\phi_{\text{diff}} = m \cdot c_p \cdot \beta + \phi_{\text{loss}}$$
Equation 3.1

The heat loss term is said to be independent of heating rate, and so becomes less impactful at rapid scanning rates. Nevertheless, to achieve better precision of absolute measurement, these heat losses should be measured and accounted for. Approaches to heat loss correction are described in the publications of Chapters 6 [111] and 7 [112], and also in the literature [70,110,113]. They consist of measurements which negate the impact of the sample term in the heat flow: by using very low heating rate to minimise the sample's impact on the measured heat flow; or by averaging measurements of equal and opposite scanning rate, from the argument these should be symmetrical (with an average heat flow of zero), except for the heat losses [110].

Equation 3.1 holds true providing that no other heat impactful changes occur. In reality, various system dependent phase transformations can cause additional time dependent enthalpy changes, adding an additional contribution to the sample term of the power differential (Equation 3.2) [70,114], where α is the conversion and Δh is the enthalpy change of the process.

$$\phi_{\text{diff}} = m \cdot (c_p + \frac{d\alpha}{dT}\Delta h) \cdot \beta + \phi_{\text{loss}}$$
Equation 3.2

It is often this term which the temperature program seeks to manipulate for scientific study.

3.3.3. THE COOLING RATE

The maximum achievable cooling rate depends on (in addition to the heat capacity of the sample-sensor system) the thermal gradients and heat exchange with the gas environment, and so is highly dependent on the gas's type and temperature [70]. Small samples of low thermal mass can more easily have their temperature changed due to their higher surface-to-volume ratio. Helium for example removes heat extremely quickly due to its higher thermal conductivity, but at higher temperatures actually overwhelms the compensative heating power of the FDSC MEMS sensor [67]. This reduces maximum operating temperature (e.g. to 180 °C [70], and for this reason nitrogen or argon are normally used. mixtures with helium can be used to increase the environment's cooling potential and maximum cooling rate.

Since it is the temperature difference between the sample and the surroundings causing the systematic heat losses responsible for cooling, the cooling rate diminishes as the sample temperature approaches the gas and sensor support temperature. This effect can become significant at higher cooling rates exceeding 10,000 K s^{-1} and certain analyses may be limited by this aspect.

3.3.4. TEMPERATURE CALIBRATION AND THERMAL LAG

Measurement on high purity metals provide the perfect means for precise temperature calibration, since they have a single melting temperature, although any definite thermal transformation can be similarly used [70]. Multiple calibrating events can be used to improve the temperature correction to a temperature-dependent function [31,70,109]. For example, a small amount of pure indium placed on top of the sample, or on the reference side of the sensor, will melt at 156.6 °C; this can be used to correct the temperatures reported be the device, which may be off by a few degrees due to thermal lag [86,114]. For MEMS heaters like that of the Flash DSC 2+, thermal lag is highly affected by the membrane-sample contact, and its impact on a transformation's measured onset temperature can be described by Equation 3.3 [86]: where β is heating rate; τ_{lag} is the thermal lag; T_{on} is the reported onset temperature; and $T_{on,0}$ is the true onset temperature.

$$T_{on} = T_{on,0} + \tau_{lag} \cdot \beta \qquad \qquad \text{Equation 3.3}$$

Higher heating rates and larger samples increase the thermal lag and temperature gradients in the system [33,115]. A recent investigation on thermal lag by Schawe [114] reported a non-linear dependence of melting onset with heating rate for low sample masses, and explained this using a heat flow model.

3.3.5. CORRELATING WITH OTHER THERMAL ANALYSIS TECHNIQUES

It is also frequently useful to examine the sample material with any of the numerous other thermal analysis (TA) methods; conventional DSC, for instance can be used to directly compare to equivalent FSC measurements and to extend the range of investigated heating and cooling rates [116]. TM-DSC can be useful for separating overlapping processes, while any number of material characteristics could warrant the use of broader thermal characterisation methods to monitor for example electrical, optical, magnetic, mechanical, or dimensional changes [117–120].

3.4. THERMODYNAMIC AND KINETIC SIMULATION

Simulations based on a CALPHAD approach (CALculation of PHAse Diagrams) can be particularly valuable in predicting difficult to measure parameters, or correlating experimental results with thermodynamic and kinetic calculations. FactSage was used to determine equilibrium heat capacity curves for the eutectic Al-Si system in Chapter 7 [112]. Non equilibrium material states can also be simulated for metallic alloys using software such as MatCalc; a kinetic calculation software with a database of physiochemical properties and several functions for time dependent heat treatments. Yield strength curves [8], phase contents [6], to diffusion phenomena impacted by dislocations and solute trapping may be object to simulation. Such calculations can be performed quickly and aid in the design and interpretation of experiment. With heat capacity, heating rate and associated enthalpy changes of the evolving system, the time dependent heat flow may be simulated far from equilibrium and can inform DSC and FDSC measurements [121]. Thermal vacancies can also be considered in CALPHAD calculations by their Gibbs energy contribution [13], or in the case of MatCalc software by FSAK vacancy dynamics [12].

3.4.1. SIMULATIONS OF DYNAMIC THERMAL VACANCY CONCENTRATIONS

Using MatCalc, vacancy concentration was predicted in aluminium for a variety of thermal histories, with some of the results included in Figure 3.5.
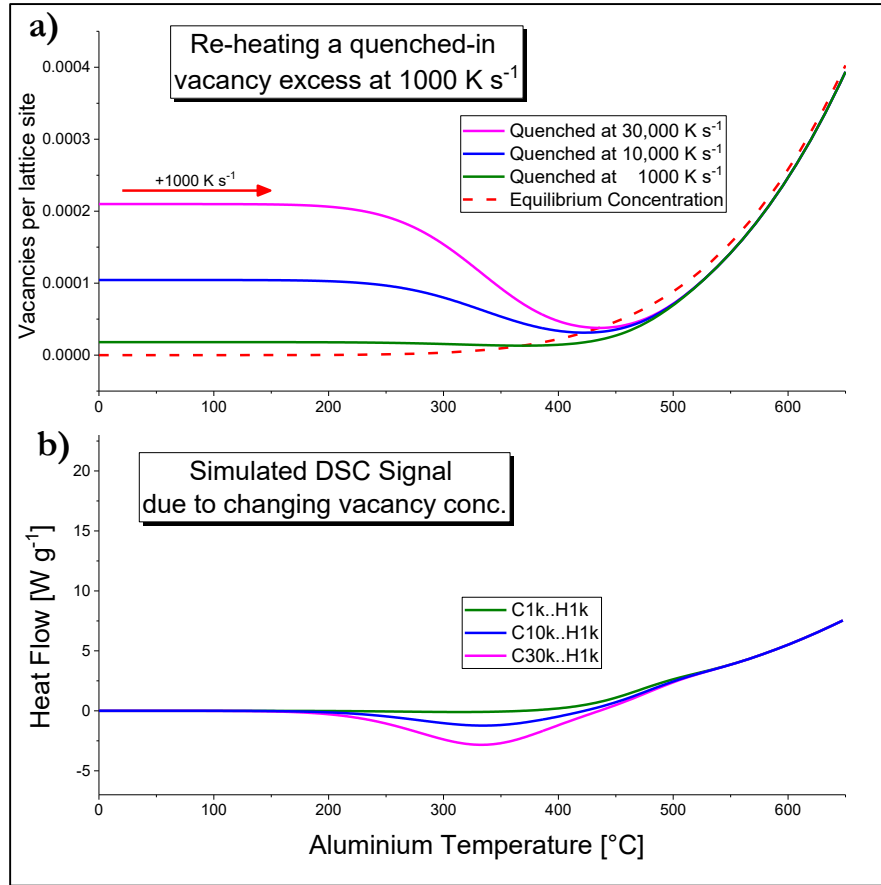
Figure 3.5: a) after rapid quenching to establish a thermal vacancy excess, vacancy concentration of Al is plotted on heating at 1000 K s⁻¹. Once temperature increases above ~200 °C, solid state diffusion proceeds at appreciable rates and the vacancy defects are mobile in the lattice. They annihilate at sinks such as free surfaces and dislocation jogs, and this process is exothermic. b) shows the simulated heat flow curve due to vacancy generation and annihilation, converted from their concentration gradient according to Equation 3.4.

MatCalc, among other things, can implement FSAK vacancy dynamics [12] to model various sources and sinks for vacancies and predict dynamic vacancy concentration. Parameters such as formation enthalpy and entropy, migration enthalpy, or even solute trapping are used to obtain the temperature dependent rate of diffusion. Parameters like grain size, dislocation density or dislocation loop size are used to determine a mean-free-path to a vacancy source/sink. In this way, the thermodynamic driving force and the diffusion-limited kinetics of vacancies can be evaluated to determine their time- and temperature-dependent concentration.

From the rate of change of vacancies, a DSC heat flow signal (ϕ_{HF} in W g⁻¹) was determined (Figure 3.5b) according to Equation 3.2: where $\frac{d[Vac]}{dT}$ is the changing vacancy concentration; $\frac{dT}{dt}$ is the heating rate; ΔH_{vac} is the vacancy formation enthalpy; and M_{Al} is the molar mass of aluminium.

$$\phi_{HF} = \left(\frac{d[Vac]}{dT}\right)\left(\frac{dT}{dt}\right)\frac{\Delta H_{vac}}{M_{Al}}\left[\frac{K\,J\,mol}{K\,s\,mol\,g}\right] \qquad \text{Equation 3.4}$$

In fact, many experiments were conducted using FDSC in attempts to experimentally detect the vacancy annihilation peak predicted in Figure 3.5b, without obtaining conclusive results. At typical FDSC sample sizes of 100 to 300 ng, the actual magnitude of the exothermic annihilation is on the order of tens of nano Joules. Such a signal is at the limit of the sensitivity of the device, and as such is easily obscured by any number of other effects. Seeking to isolate the annihilation effect in the signal and increase precision certainly contributed to improving experimental approach; however, verifying the annihilation effect however demands an irrefutable level of consistency in the heat flow signal. Meanwhile, relaxation of mechanical stresses (e.g. at the membrane interface) or even non-vacancy defects generated in the sample by rapid quenching can sufficiently perturb the measured heat flow [89,97] to obscure the annihilation peak in the signal.

3.5. SURFACE IMAGING TECHNIQUES

Some assessment of the sample can also be made through surface imaging techniques, and visual impression of the sample-sensor system is often useful for further analysis. Visible light microscopy, as well as showing the sample position over the membrane's sample area, can give a measure of the sample's size and geometry [122]. For geometrically simple sample shapes, such as spherical powder or evenly flat foils, it is feasible to obtain an approximate mass estimation. To prevent damaging the membrane and wires protruding from the FDSC chip sensors they can be lain upon a simple rubber O-ring (~20 mm) on the microscope stage.

Scanning electron microscopy (SEM) can also be a valuable tool for sample assessment, ex-situ, showing microstructural detail in the sample [123]. Without damaging the chip sensor's functionality, it can be mounted inside to the sample stage on a rubber O-ring. Securing with conductive copper tape helps to reduce charging, but cannot be wholly avoided. Plasma cleaning and graphite sputter coating the sensor can also be beneficial here, as the graphite coating help to conduct away any charge buildup. A sample's internal microstructure can also be examined by embedding the chip sensor in resin and grinding down until the polished surface coincides with the sample cross section [34,122].

3.6. IN-SITU TEM

In-situ electron microscopy experiments can be carried out using Protochips Fusion Select e-chips (MEMS chip sensors) inside a Thermo Fisher Scientific™ Talos F200X scanning transmission electron microscope. After thinning, sectioning, and placing an electron transparent sample above the holes of the MEMS sensor membrane, the e-chip is mounted to the Protochips holder and inserted into the TEM. From here, all normal characterisation methods are possible, while also being able to manipulate the sample temperature and heating rate to monitor material changes as they happen. Chapter 8's publication [124] discusses one such experiment.

First taking an overview of the whole grid of holes at low magnification, the region of interest (ROI) is chosen depending on the observable sample featured. A hole partially covered by the sample should be electron transparent (providing the polishing and sample sectioning is properly performed), and the sample edge provides a good reference point for further characterisation. Bright field and dark field TEM (BF-TEM and DF-TEM), high angle annular dark field (HAADF), high resolution TEM and STEM (HR-TEM and HR-STEM), selected area electron diffraction (SAED) and energy-dispersive x-ray spectroscopy (EDS) can all be implemented at static and dynamic temperatures to monitor compositional and crystallographic changes by observing size and contrast differences. Image stability is crucial for some of these methods, so faster rates and higher temperatures can limit the characterisation possibilities. EDS elemental mapping for instance could take 20 minutes, so a static temperature is required for best sample stability (room temperature is the lowest possible with the Protochips Fusion holder). For such small samples, electron beam damage can significantly impact the sample state [125], as can heating near the melting point, resulting in numerous effects including coalescence and thinning of the sample ROI [126]. Attention to the design of the experiment's temperature programs as well as the characterisation procedure can help in making the most out of the sample and the various imaging techniques.

3.7. IN-SITU X-RAY DIFFRACTION WITH A SYNCHROTRON

One of the central tools in crystallographic characterisation is that of x-ray diffraction (XRD), where the angles and intensities in diffraction patterns are analysed to determine the three-dimensional electron density of a sample, and thereby its crystal structure. To make such analysis on dynamic crystal structures, high temporal resolution is needed, which is only possible with high intensities. Synchrotron facilities are able to produce x-rays at high intensities by accelerating electrons; a change in electron velocity involves the emission of a photon, whose energy corresponds to the change in electron momentum [128]. A high concentration of electrons is accelerated around a bend, and the resultant photons are focused into a narrow beam line, into which a sample is placed for characterisation. The utility of synchrotron radiation as an extremely brilliant source of x-rays encompasses structural characterisation in all disciplines, from molecular biology to metallurgical phase transformations, and remains a vital tool which drives our understanding of structure and transient states. [129]

Using a modified sensor support, in-situ XRD can be performed in a synchrotron using Mettler-Toledo's Flash DSC 2+ with a setup like that shown in Figure 3.7. The mounted chip is positioned outside of the device, via a cable extension, into the path of the beamline. The x-ray beam passes through the sample and membrane. Argon gas flow at ambient temperature reduces the oxygen vapour pressure near the sample. With no intracooler, sub-ambient temperatures are not possible, but rapid heating and cooling can still be accomplished. An electronic trigger is sent by the FDSC at a chosen point in the temperature program and is read by the Pilatus detector which begins recording. The extremely high temporal resolution offered by the Pilatus detector, coupled with the high intensity of

incident x-rays, mean rapid structural changes can be depicted and analysed from the x-ray diffraction (XRD) pattern. In combination with FDSC, XRD is a potent method for examining microstructural changes as they happen, and can be extremely revealing with regards to nucleation mechanisms and phase transformations [127].

Figure 3.7: Experimental setup for the in-situ synchrotron measurements, showing the measurement cell where the chip is mounted outside of the FDSC device and in the path of the beamline.

4. BIBLIOGRAPHY

[1] P.W. Atkins, J. de Paula, Atkins' physical chemistry, ninth ed., Oxford University Press, Oxford, New York, 2010.

[2] Saunders, CALPHAD (Elsevier Science of Phase Diagrams): A Comprehensive Guide: A comprehensive guide, Transferred to digital print, Pergamon, [Lieu de publication non identifié], 1998.

[3] Y.N. Zhuravlev, M.V. Aleinikova, D.V. Korabelnikov, AB Initio calculations of thermodynamic parameters of lithium, sodium and potassium peroxides, Russ Phys J 55 (2012) 622–628. https://doi.org/10.1007/s11182-012-9858-6.

[4] M. Grujicic, G. Cao, R.S. Miller, Computer Modeling of the Evolution of Dendrite Microstructure in Binary Alloys During Non-isothermal Solidification, Journal of Materials Synthesis and Processing 10 (2002) 191–203. https://doi.org/10.1023/A:1023022214920.

[5] T.J. Chen, X.K. Yang, H. Xue, G.L. Bi, X.Z. Zhang, R.G. Guan, Mixing process and nucleation of an Al-Si alloy during controlled diffusion solidification with simultaneous mixing and effect of mixing rate, J Mater Sci 57 (2022) 3018–3040. https://doi.org/10.1007/s10853-021-06730-3.

[6] P. LANG, T. Wojcik, E. POVODEN-KARADENIZ, A. FALAHATI, E. KOZESCHNIK, Thermo-kinetic prediction of metastable and stable phase precipitation in Al–Zn–Mg series aluminium alloys during non-isothermal DSC analysis, Journal of Alloys and Compounds 609 (2014) 129–136. https://doi.org/10.1016/j.jallcom.2014.04.119.

[7] S.P. B.S., R. V.B., H.K. K.C., Numerical simulation of precipitate evolution in ferritic–martensitic power plant steels, Calphad 36 (2012) 1–7. https://doi.org/10.1016/j.calphad.2011.10.006.

[8] J. Kreyca, A. FALAHATI, E. KOZESCHNIK, Modelling Yield Strength in an A6061 Aluminium Alloy, MSF 879 (2016) 1014–1018. https://doi.org/10.4028/www.scientific.net/MSF.879.1014.

[9] K. Gururaj, S. Pal, Influence of dislocation density and grain size on precipitation kinetics on P92 grade steel, Materials Today: Proceedings 18 (2019) 1364–1374. https://doi.org/10.1016/j.matpr.2019.06.602.

[10] A. Nicholas Grundy, E. Povoden, T. Ivas, L.J. Gauckler, Calculation of defect chemistry using the CALPHAD approach, Calphad 30 (2006) 33–41. https://doi.org/10.1016/j.calphad.2005.11.004.

[11] D.A. Porter, K.E. Easterling, Phase transformations in metals and alloys, secondnd ed., Chapman & Hall, London, New York, 1992.

[12] F.D. Fischer, J. Svoboda, F. Appel, E. Kozeschnik, Modeling of excess vacancy annihilation at different types of sinks, Acta Materialia 59 (2011) 3463–3472. https://doi.org/10.1016/j.actamat.2011.02.020.

[13] A. Obaied, I. Roslyakova, M. To Baben, Including state-of-the-art physical understanding of thermal vacancies in Calphad models, Sci Rep 12 (2022) 13385. https://doi.org/10.1038/s41598-022-16926-5.

[14] G.F. Liptrot, J.J. Thompson, G.R. Walker, Modern physical chemistry, Unwin Hyman, London, 1982.

[15] C. Kittel, Introduction to solid state physics, eighth. ed., [repr.], Wiley, Hoboken, NJ, 20]13.

[16] H.P. Myers, Introductory solid state physics, Second edition, CRC Press; Taylor & Francis, Boca Raton, London, 1997.

[17] D.V. Schroeder, An Introduction to Thermal Physics, Pearson new international edition, Pearson, Harlow, 2014.

[18] R. Nave, Phonons and the Debye specific heat. http://hyperphysics.phy-astr.gsu.edu/hbase/Solids/phonon.html (accessed 23 July 2022).

[19] U. Piespergen, Chapter 3 Heat Capacity and Debye Temperatures, in: Semiconductors and semimetals: A treatise, Elsevier, Acad. Press, Amsterdam [u.a.], Heidelberg, 1966, pp. 49–60.

[20] C. Jeong, S. Datta, M. Lundstrom, Full dispersion versus Debye model evaluation of lattice thermal conductivity with a Landauer approach, Journal of Applied Physics 109 (2011) 73718. https://doi.org/10.1063/1.3567111.

[21] J. Li, P.-F. Liu, C. Zhang, X. Shi, S. Jiang, W. Chen, H. Yin, B.-T. Wang, Lattice vibrational modes and phonon thermal conductivity of single-layer GaGeTe, Journal of Materiomics 6 (2020) 723–728. https://doi.org/10.1016/j.jmat.2020.04.005.

[22] T. Hadji, H. Khalfoun, H. Rached, Y. Guermit, A. Azzouz-Rached, D. Rached, DFT study with different exchange-correlation potentials of physical properties of the new synthesized alkali-metal based Heusler alloy, Eur. Phys. J. B 93 (2020) 1–10. https://doi.org/10.1140/epjb/e2020-10204-5.

[23] E.H. Sondheimer, The mean free path of electrons in metals, Advances in Physics 50 (2001) 499–537. https://doi.org/10.1080/00018730110102187.

[24] A.L. Lavoisier, Elements of chemistry, in a new systematic order: containing all the modern discoveries, first ed., Dover Publications, New York, 1965 (1790).

[25] Mutasem Odeh, About the Quantum Mechanics of the Electrons in Crystal Lattices, 2018. https://courses.physics.ucsd.edu/2018/fall/physics211a/topic/bloch.pdf.

[26] J.C. Slater, Magnetic Effects and the Hartree-Fock Equation, Phys. Rev. 82 (1951) 538–541. https://doi.org/10.1103/PhysRev.82.538.

[27] G.W.H. Höhne, W.F. Hemminger, H.-J. Flammersheim, Differential Scanning Calorimetry, Springer Berlin Heidelberg, Berlin, Heidelberg, 2003.

[28] Sham, Exchange and correlation in density-functional theory, Phys. Rev. B Condens. Matter 32 (1985) 3876–3882. https://doi.org/10.1103/physrevb.32.3876.

[29] E.P. Wohlfarth, XLIX. The influence of exchange and correlation forces on the specific heat of free electrons in metals, The London, Edinburgh, and Dublin Philosophical Magazine and Journal of Science 41 (1950) 534–542. https://doi.org/10.1080/14786445008561118.

[30] R.L. Danley, New heat flux DSC measurement technique, Thermochimica Acta 395 (2002) 201–208. https://doi.org/10.1016/S0040-6031(02)00212-5.

[31] B. Yang, B. Milkereit, Y. Zhang, P.A. Rometsch, O. Kessler, C. Schick, Continuous cooling precipitation diagram of aluminium alloy AA7150 based on a new fast scanning calorimetry and interrupted quenching method, Materials Characterization 120 (2016) 30–37. https://doi.org/10.1016/j.matchar.2016.08.016.

[32] J.E.K. Schawe, J.F. Löffler, Existence of multiple critical cooling rates which generate different types of monolithic metallic glass, Nat Commun 10 (2019) 1337. https://doi.org/10.1038/s41467-018-07930-3.

[33] B. Yang, A.S. Abyzov, E. Zhuravlev, Y. Gao, Schmelzer, J. W. P., C. Schick, Size and rate dependence of crystal nucleation in single tin drops by fast scanning calorimetry, The Journal of Chemical Physics 138 (2013) 54501. https://doi.org/10.1063/1.4789447.

[34] B. Yang, Q. Peng, B. Milkereit, A. Springer, D. Liu, M. Rettenmayr, C. Schick, O. Keßler, Nucleation behaviour and microstructure of single Al-Si12 powder particles rapidly solidified in a fast scanning calorimeter, J Mater Sci 56 (2021) 12881–12897. https://doi.org/10.1007/s10853-021-06096-6.

[35] A.S. Sedra, K.C. Smith, Microelectronic Circuits: International Student Edition, fifthth ed., Oxford University Press, New York, 2004.

[36] M. Reading, D. Elliott, V.L. Hill, A new approach to the calorimetric investigation of physical and chemical transitions, Journal of Thermal Analysis 40 (1993) 949–955. https://doi.org/10.1007/BF02546854.

[37] J. Schawe, Principles for the interpretation of modulated temperature DSC measurements. Part 1. Glass transition, Thermochimica Acta 261 (1995) 183–194. https://doi.org/10.1016/0040-6031(95)02315-S.

[38] J. Schawe, A comparison of different evaluation methods in modulated temperature DSC, Thermochimica Acta 260 (1995) 1–16. https://doi.org/10.1016/0040-6031(95)90466-2.

[39] A.A. Lacey, C. Nikolopoulos, M. Reading, A mathematical model for Modulated Differential Scanning Calorimetry, Journal of Thermal Analysis 50 (1997) 279–333. https://doi.org/10.1007/BF01979568.

[40] Z. Jiang, C.T. Imrie, J.M. Hutchinson, An introduction to temperature modulated differential scanning calorimetry (TMDSC): a relatively non-mathematical approach, Thermochimica Acta 387 (2002) 75–93. https://doi.org/10.1016/S0040-6031(01)00829-2.

[41] B. Wunderlich, A. Boller, I. Okazaki, K. Ishikiriyama, Heat-capacity determination by temperature-modulated DSC and its separation from transition effects, Thermochimica Acta 304-305 (1997) 125–136. https://doi.org/10.1016/S0040-6031(97)00184-6.

[42] J. Schawe, T. Hütter, C. Heitz, I. Alig, D. Lellinger, Stochastic temperature modulation: A new technique in temperature-modulated DSC, Thermochimica Acta 446 (2006) 147–155. https://doi.org/10.1016/j.tca.2006.01.031.

[43] M. Schubnell, C. Heitz, T. Hütter, S. Sauerbrunn, Schawe J.E.K., A multifrequency temperature-modulated technique for DSC, American Laboratory 38 (2006) 18–26.

[44] J.M. Hutchinson, Studying the Glass Transition by DSC and TMDSC, J Therm Anal Calorim 72 (2003) 619–629. https://doi.org/10.1023/A:1024542103314.

[45] C.A. Gracia-Fernández, S. Gómez-Barreiro, J. López-Beceiro, J. Tarrío Saavedra, S. Naya, R. Artiaga, Comparative study of the dynamic glass transition temperature by DMA and TMDSC, Polymer Testing 29 (2010) 1002–1006. https://doi.org/10.1016/j.polymertesting.2010.09.005.

[46] M.L. Di Lorenzo, R. Androsch, A.M. Rhoades, M.C. Righetti, Analysis of Polymer Crystallization by Calorimetry, in: C. Schick, N. Koga, S. Vyazovkin (Eds.), Handbook of Thermal Analysis and Calorimetry Recent Advances, Techniques and Applications Ed. 2, Elsevier, 2018, pp. 253–299.

[47] Z. Qiu, M. Komura, T. Ikehara, T. Nishi, DSC and TMDSC study of melting behaviour of poly(butylene succinate) and poly(ethylene succinate), Polymer 44 (2003) 7781–7785. https://doi.org/10.1016/j.polymer.2003.10.045.

[48] A. Menyhárd, J. Varga, G. Molnár, Comparison of different -nucleators for isotactic polypropylene, characterisation by DSC and temperature-modulated DSC (TMDSC) measurements, J Therm Anal Calorim 83 (2006) 625–630. https://doi.org/10.1007/s10973-005-7498-6.

[49] G.B. McKenna, S.L. Simon, The glass transition: its measurement and underlying physics, in: S.Z.D. Cheng (Ed.), Handbook of thermal analysis and calorimetry, first. ed., Elsevier, Amsterdam, 2002, pp. 49–109.

[50] M. Varma-Nair, B. Wunderlich, Non isothermal heat capacities and chemical reactions using a modulated DSC, Journal of Thermal Analysis 46 (1996) 879–892. https://doi.org/10.1007/BF01983608.

[51] Q. Lu, B. Zhang, M. Li, B. Zuo, D.L. Kaplan, Y. Huang, H. Zhu, Degradation mechanism and control of silk fibroin, Biomacromolecules 12 (2011) 1080–1086. https://doi.org/10.1021/bm101422j.

[52] J.E. Schawe, S. Pogatscher, J.F. Löffler, Thermodynamics of polymorphism in a bulk metallic glass: Heat capacity measurements by fast differential scanning calorimetry, Thermochimica Acta 685 (2020) 178518. https://doi.org/10.1016/j.tca.2020.178518.

[53] S.D. Senturia, Microsystem Design, Springer US, Boston, MA, 2001.

[54] S.E. Lyshevski, Nano- and micro-electromechanical systems: Fundamentals of nano- and microengineering, secondnd ed., CRC Press, Boca Raton, Fla., 2005.

[55] N. Maluf, An introduction to microelectromechanical systems, Artech House, Boston, London, 2000.

[56] Q. Zhou, Y. Zhang, MEMS Technology for Biomedical Imaging Applications, MDPI - Multidisciplinary Digital Publishing Institute, [Erscheinungsort nicht ermittelbar], 2019.

[57] Eric A. Olson, Mikhail Yu. Efremov, Ming Zhang, Zishu Zhang, Leslie H. Allen, The design and operation of a MEMS differential scanning nanocalorimeter for high speed heat capacity measurements of ultrathin films, J. of Microelectromechanical Systems (2003) 355–364. https://doi.org/10.1109/JMEMS.2003.811755.

[58] J.F. Creemer, S. Helveg, G.H. Hoveling, S. Ullmann, A.M. Molenbroek, P.M. Sarro, H.W. Zandbergen, Atomic-scale electron microscopy at ambient pressure, Ultramicroscopy 108 (2008) 993–998. https://doi.org/10.1016/j.ultramic.2008.04.014.

[59] N. Islam, S. Saye, MEMS Microfluidics for Lab-on-a-Chip Applications, in: N. Islam (Ed.), Microelectromechanical Systems and Devices, InTech, 2012.

[60] J.L. Garcia-Cordero, A.J. Ricco, Lab-on-a-Chip (General Philosophy), in: D. Li (Ed.), Encyclopedia of microfluidics and nanofluidics: With 152 tables, Springer, New York, NY, 2008, pp. 962–969.

[61] D. Mark, S. Haeberle, G. Roth, F. von Stetten, R. Zengerle, Microfluidic Lab-on-a-Chip Platforms: Requirements, Characteristics and Applications, in: S. Kakaç, B. Kosoy, D. Li, A. Pramuanjaroenkij (Eds.), Microfluidics Based Microsystems, Springer, Dordrecht, 2010, pp. 305–376.

[62] X. Zhu, E.S. Kim, Microfluidic motion generation with acoustic waves, Sensors and Actuators A: Physical 66 (1998) 355–360. https://doi.org/10.1016/S0924-4247(97)01712-3.

[63] C.H. Ahn, J.-W. Choi, Microfluidic Devices and Their Applications to Lab-on-a-Chip, in: B. Bhushan (Ed.), SPRINGER handbook of nanotechnology, thirdrd ed., Springer Verlag, Berlin, Heidelberg, 2010, pp. 503–530.

[64] R.G. Polcawich, J.S. Pulskamp, S. Bedair, G. Smith, R. Kaul, C. Kroninger, E. Wetzel, H. Chandrahalim, S.A. Bhave, Integrated PiezoMEMS actuators and sensors, in: Sensors, 2010 IEEE, Kona, HI, IEEE, 2010, pp. 2193–2196.

[65] T. Pensala, J. Kiihamaki, J. Kyynarainen, J. Dekker, S. Gorelick, P. Pekko, T. Pernu, O. Ylivaara, F. Gao, D. Morits, Wobbling Mode AlN-Piezo-MEMS Mirror Enabling 360-Degree Field of View LIDAR for Automotive Applications, in: 2019 IEEE International Ultrasonics Symposium (IUS), Glasgow, United Kingdom, IEEE, 10/6/2019 - 10/9/2019, pp. 1977–1980.

[66] M. Nafea, A. Nawabjan, M.S. Mohamed Ali, A wirelessly-controlled piezoelectric microvalve for regulated drug delivery, Sensors and Actuators A: Physical 279 (2018) 191–203. https://doi.org/10.1016/j.sna.2018.06.020.

[67] J.E.K. Schawe, S. Pogatscher, Material Characterization by Fast Scanning Calorimetry: Practice and Applications, in: C. Schick, V. Mathot (Eds.), Fast scanning calorimetry, Springer International Publishing Switzerland, [Cham], op. 2016, pp. 3–80.

[68] D. Denlinger, E. Abarra, K. Allen, P. W. Rooney, M. T. Messer, S. K. Watson, F. Hellman, Thin film microcalorimeter for heat capacity measurements from 1.5 to 800 K, undefined (1994).

[69] S.L. Lai, G. Ramanath, L.H. Allen, P. Infante, Z. Ma, High-speed (10 4 °C/s) scanning microcalorimetry with monolayer sensitivity (J/m 2), Appl. Phys. Lett. 67 (1995) 1229–1231. https://doi.org/10.1063/1.115016.

[70] C. Schick, V. Mathot (Eds.), Fast Scanning Calorimetry, Springer International Publishing; Imprint; Springer, Cham, 2016.

[71] Efremov, Schiettekatte, Zhang, Olson, Kwan, Berry, Allen, Discrete periodic melting point observations for nanostructure ensembles, Phys. Rev. Lett. 85 (2000) 3560–3563. https://doi.org/10.1103/PhysRevLett.85.3560.

[72] Lai, Guo, Petrova, Ramanath, Allen, Size-Dependent Melting Properties of Small Tin Particles: Nanocalorimetric Measurements, Phys. Rev. Lett. 77 (1996) 99–102. https://doi.org/10.1103/PhysRevLett.77.99.

[73] S.L. Lai, G. Ramanath, L.H. Allen, P. Infante, Heat capacity measurements of Sn nanostructures using a thin-film differential scanning calorimeter with 0.2 nJ sensitivity, Appl. Phys. Lett. 70 (1997) 43–45. https://doi.org/10.1063/1.119299.

[74] E. Iervolino, A.W. van Herwaarden, F.G. van Herwaarden, E. van de Kerkhof, P. van Grinsven, A. Leenaers, V. Mathot, P.M. Sarro, Temperature calibration and electrical characterization of

the differential scanning calorimeter chip UFS1 for the Mettler-Toledo Flash DSC 1, Thermochimica Acta 522 (2011) 53–59. https://doi.org/10.1016/j.tca.2011.01.023.

[75] N. Lindemann, J.E.K. Schawe, J. Lacayo-Pineda, Kinetics of the glass transition of styrene-butadiene-rubber: Dielectric spectroscopy and fast differential scanning calorimetry, J Appl Polym Sci 138 (2021) 49769. https://doi.org/10.1002/app.49769.

[76] S. Adamovsky, A. Minakov, C. Schick, Scanning microcalorimetry at high cooling rate, Thermochimica Acta 403 (2003) 55–63. https://doi.org/10.1016/S0040-6031(03)00182-5.

[77] I. Kolesov, D. Mileva, R. Androsch, C. Schick, Structure formation of polyamide 6 from the glassy state by fast scanning chip calorimetry, Polymer 52 (2011) 5156–5165. https://doi.org/10.1016/j.polymer.2011.09.007.

[78] J.E.K. Schawe, Influence of processing conditions on polymer crystallization measured by fast scanning DSC, J Therm Anal Calorim 116 (2014) 1165–1173. https://doi.org/10.1007/s10973-013-3563-8.

[79] S. Pogatscher, P.J. Uggowitzer, J.F. Löffler, In-situ probing of metallic glass formation and crystallization upon heating and cooling via fast differential scanning calorimetry, Appl. Phys. Lett. 104 (2014) 251908. https://doi.org/10.1063/1.4884940.

[80] F. Spieckermann, I. Steffny, X. Bian, S. Ketov, M. Stoica, J. Eckert, Fast and direct determination of fragility in metallic glasses using chip calorimetry, Heliyon 5 (2019) e01334. https://doi.org/10.1016/j.heliyon.2019.e01334.

[81] N. Neuber, M. Frey, O. Gross, J. Baller, I. Gallino, R. Busch, Ultrafast scanning calorimetry of newly developed Au-Ga bulk metallic glasses, J. Phys. Condens. Matter 32 (2020) 324001. https://doi.org/10.1088/1361-648X/ab8252.

[82] S. Pogatscher, D. Leutenegger, J.E.K. Schawe, P.J. Uggowitzer, J.F. Löffler, Solid-solid phase transitions via melting in metals, Nat Commun 7 (2016) 11113. https://doi.org/10.1038/ncomms11113.

[83] B. Zhao, B. Yang, A.S. Abyzov, J.W.P. Schmelzer, J. Rodríguez-Viejo, Q. Zhai, C. Schick, Y. Gao, Beating Homogeneous Nucleation and Tuning Atomic Ordering in Glass-Forming Metals by Nanocalorimetry, Nano Lett. 17 (2017) 7751–7760. https://doi.org/10.1021/acs.nanolett.7b03952.

[84] Mettler-Toledo Group, Flash DSC 2+ Brochure, 2018.

[85] Mettler-Toledo, Flash DSC 2+ User Manual, 2019.

[86] C. Schick, R. Androsch, Fast Scanning Chip Calorimetry, in: C. Schick, N. Koga, S. Vyazovkin (Eds.), Handbook of Thermal Analysis and Calorimetry Recent Advances, Techniques and Applications Ed. 2, Elsevier, 2018, pp. 47–102.

[87] C. Schick, T.A. Mukhametzyanov, B.N. Solomonov, Fast Scanning Calorimetry of Organic Materials from Low Molecular Mass Materials to Polymers, rev. and adv. in chem. 11 (2021) 1–72. https://doi.org/10.1134/S2079978021010064.

[88] Protochips, Fusion Select Components, 2022. https://www.protochips.com/products/fusion/fusion-select-components/ (accessed 7 June 2022).

[89] J. Damiano, D.P. Nackashi, S.E. Mick, A MEMS-based Technology Platform for in-situ TEM Heating Studies, Microscopy and Microanalysis 14 (2008) 1332–1333. https://doi.org/10.1017/S1431927608088363.

[90] Z. Ying, J. Diao, S. Wang, X. Cai, Y. Cai, H. Liu, N. Wang, Revealing high temperature stability of platinum nanocatalysts deposited on graphene oxide by in-situ TEM, Materials Characterization 170 (2020) 110706. https://doi.org/10.1016/j.matchar.2020.110706.

[91] P.D. Edmondson, Report on the Installation and Preparedness of a Protochips Fusion in-situ Heating Holder for TEM, Office of Scientific and Technical Information (OSTI), 2017.

[92] M. Hammad Fawey, V.S.K. Chakravadhanula, M.A. Reddy, C. Rongeat, T. Scherer, H. Hahn, M. Fichtner, C. Kübel, In situ TEM studies of micron-sized all-solid-state fluoride ion batteries: Preparation, prospects, and challenges, Microsc. Res. Tech. 79 (2016) 615–624. https://doi.org/10.1002/jemt.22675.

[93] M. Singh, C. Ghosh, P. Kotula, J. Watt, H. Silva, C.B. Carter, Direct Observation of Phase Transformations in Ge-Sb-Te Materials, Microsc Microanal 26 (2020) 1418–1420. https://doi.org/10.1017/S1431927620018036.

[94] K. Tiwari, K. Biswas, Transmission Electron Microscopy Investigation of Phase Transformation Behavior of Alloy Nanoparticles, in: K. Biswas, S. Sivakumar, N. Gurao (Eds.), Electron Microscopy in Science and Engineering: Alloy Nanoparticles, Springer, Singapore, 2022, pp. 103–116.

[95] S.B. Alam, C.R. Andersen, F. Panciera, A.A.S. Nilausen, O. Hansen, F.M. Ross, K. Mølhave, In situ TEM modification of individual silicon nanowires and their charge transport mechanisms, Nanotechnology 31 (2020) 494002. https://doi.org/10.1088/1361-6528/ababc8.

[96] L.F. Allard, W.C. Bigelow, M. Jose-Yacaman, D.P. Nackashi, J. Damiano, S.E. Mick, A new MEMS-based system for ultra-high-resolution imaging at elevated temperatures, Microsc. Res. Tech. 72 (2009) 208–215. https://doi.org/10.1002/jemt.20673.

[97] M.A. Haque, M. Saif, Application of MEMS force sensors for in situ mechanical characterization of nano-scale thin films in SEM and TEM, Sensors and Actuators A: Physical 97-98 (2002) 239–245. https://doi.org/10.1016/S0924-4247(01)00861-5.

[98] P. Dumitraschkewitz, M.A. Tunes, C.R. Quick, D.S.R. Coradini, T.M. Kremmer, P. Ramasamy, P.J. Uggowitzer, S. Pogatscher, MEMS-Based in situ electron-microscopy investigation of rapid solidification and heat treatment on eutectic Al-Cu, Acta Materialia 239 (2022). https://doi.org/10.1016/j.actamat.2022.118225.

[99] V.I. Tkatch, A.I. Limanovskii, S.N. Denisenko, S.G. Rassolov, The effect of the melt-spinning processing parameters on the rate of cooling, Materials Science and Engineering: A 323 (2002) 91–96. https://doi.org/10.1016/S0921-5093(01)01346-6.

[100] D. Landolt, Fundamental aspects of electropolishing, Electrochimica Acta 32 (1987) 1–11. https://doi.org/10.1016/0013-4686(87)87001-9.

[101] A. Méndez-Vilas, J. Díaz (Eds.), Microscopy: Science, technology, applications and education. TEM specimen preparation techniques, Formatex Research Center, Badajoz, 2010.

[102] B.J. Kestel, Improved Methods and Novel Techniques for Jet Electropolishing of TEM Foils, MRS Proc. 199 (1990). https://doi.org/10.1557/PROC-199-51.

[103] N. Ünlü, Preparation of high quality Al TEM specimens via a double-jet electropolishing technique, Materials Characterization 59 (2008) 547–553. https://doi.org/10.1016/j.matchar.2007.04.003.

[104] H.K. Zhang, F. Long, Z. Yao, M.R. Daymond, Novel techniques of preparing TEM samples for characterization of irradiation damage, J. Microsc. 252 (2013) 251–257. https://doi.org/10.1111/jmi.12085.

[105] Delstar, ELECTROPOLISHING: A User's Guide to Applications, Quality Standards and Specifications, 2003. https://www.delstar.com/assets/pdf/epusersguide.pdf?r=false (accessed 25 July 2022).

[106] X. Zhong, C.A. Wade, P.J. Withers, X. Zhou, C. Cai, S.J. Haigh, M.G. Burke, Comparing Xe+ pFIB and Ga+ FIB for TEM sample preparation of Al alloys: Minimising FIB-induced artefacts, J. Microsc. 282 (2021) 101–112. https://doi.org/10.1111/jmi.12983.

[107] B. Yang, Y. Gao, C. Zou, Q. Zhai, A.S. Abyzov, E. Zhuravlev, Schmelzer, J. W. P., C. Schick, Cooling rate dependence of undercooling of pure Sn single drop by fast scanning calorimetry, Appl. Phys. A 104 (2011) 189–196. https://doi.org/10.1007/s00339-010-6100-7.

[108] Q. Cheng, X. Han, I. Kaban, I. Soldatov, W.H. Wang, Y.H. Sun, J. Orava, Phase transformations in a Cu–Zr–Al metallic glass, Scripta Materialia 183 (2020) 61–65. https://doi.org/10.1016/j.scriptamat.2020.03.028.

[109] E. Zhuravlev, C. Schick, Fast scanning power compensated differential scanning nano-calorimeter: 1. The device, Thermochimica Acta 505 (2010) 1–13. https://doi.org/10.1016/j.tca.2010.03.019.

[110] E. Zhuravlev, C. Schick, Fast scanning power compensated differential scanning nano-calorimeter: 2. Heat capacity analysis, Thermochimica Acta 505 (2010) 14–21. https://doi.org/10.1016/j.tca.2010.03.020.

[111] C.R. Quick, J. Schawe, P.J. Uggowitzer, S. Pogatscher, Measurement of specific heat capacity via fast scanning calorimetry—Accuracy and loss corrections, Thermochimica Acta 677 (2019) 12–20. https://doi.org/10.1016/j.tca.2019.03.021.

[112] Cameron R. Quick, Phillip Dumitraschkewitz, Jürgen E. K. Schawe, Stefan Pogatscher, Fast Differential Scanning Calorimetry to Mimic Additive Manufacturing Processing: Specific Heat Capacity Analysis of Aluminium Alloys, Journal of Thermal Analysis and Calorimetry (under review) (2022).

[113] P. Cebe, B.P. Partlow, D.L. Kaplan, A. Wurm, E. Zhuravlev, C. Schick, Using flash DSC for determining the liquid state heat capacity of silk fibroin, Thermochimica Acta 615 (2015) 8–14. https://doi.org/10.1016/j.tca.2015.07.009.

[114] J.E. Schawe, Temperature correction at high heating rates for conventional and fast differential scanning calorimetry, Thermochimica Acta 698 (2021) 178879. https://doi.org/10.1016/j.tca.2021.178879.

[115] S. van Herwaarden, E. Iervolino, F. van Herwaarden, T. Wijffels, A. Leenaers, V. Mathot, Design, performance and analysis of thermal lag of the UFS1 twin-calorimeter chip for fast scanning calorimetry using the Mettler-Toledo Flash DSC 1, Thermochimica Acta 522 (2011) 46–52. https://doi.org/10.1016/j.tca.2011.05.025.

[116] D. ZOHRABYAN, B. Milkereit, C. Schick, O. Kessler, Continuous cooling precipitation diagram of high alloyed Al-Zn-Mg-Cu 7049A alloy, Transactions of Nonferrous Metals Society of China 24 (2014) 2018–2024. https://doi.org/10.1016/S1003-6326(14)63307-0.

[117] S.Z.D. Cheng (Ed.), Handbook of thermal analysis and calorimetry, 1st ed., Elsevier, Amsterdam, 2002.

[118] C. Schick, N. Koga, S. Vyazovkin (Eds.), Handbook of Thermal Analysis and Calorimetry Recent Advances, Techniques and Applications Ed. 2, Elsevier, 2018.

[119] M. Nijman, A. Hammer, E. Hempel, N. Jing, R. Riesen, J.E.K. Schawe, M. Schubnell, C. Wrana, Thermal Analysis in Practice: Tips and Hints, 2016. https://www.mt.com/int/en/home/library/applications/lab-analytical-instruments/thermal-analysis-tips-and-hints.html (accessed 17 August 2022).

[120] M.E. Brown (Ed.), Introduction to Thermal Analysis: Techniques and Applications, Springer International Publishing, Cham, 20.

[121] A. FALAHATI, J. WU, P. LANG, M.R. AHMADI, E. POVODEN-KARADENIZ, E. KOZESCHNIK, Assessment of parameters for precipitation simulation of heat treatable

aluminum alloys using differential scanning calorimetry, Transactions of Nonferrous Metals Society of China 24 (2014) 2157–2167. https://doi.org/10.1016/S1003-6326(14)63327-6.

[122] Q. Peng, B. Yang, B. Milkereit, D. Liu, A. Springer, M. Rettenmayr, C. Schick, O. Keßler, Nucleation Behavior of a Single Al-20Si Particle Rapidly Solidified in a Fast Scanning Calorimeter, Materials 14 (2021). https://doi.org/10.3390/ma14112920.

[123] S. Heiland, B. Milkereit, K.-P. Hoyer, E. Zhuravlev, O. Kessler, M. Schaper, Requirements for Processing High-Strength AlZnMgCu Alloys with PBF-LB/M to Achieve Crack-Free and Dense Parts, Materials 14 (2021). https://doi.org/10.3390/ma14237190.

[124] M.A. Tunes, C.R. Quick, L. Stemper, D.S.R. Coradini, J. Grasserbauer, P. Dumitraschkewitz, T.M. Kremmer, S. Pogatscher, A Fast and Implantation-Free Sample Production Method for Large Scale Electron-Transparent Metallic Samples Destined for MEMS-Based In Situ S/TEM Experiments, Materials 14 (2021). https://doi.org/10.3390/ma14051085.

[125] O. El-Atwani, J.A. Hinks, G. Greaves, S. Gonderman, T. Qiu, M. Efe, J.P. Allain, In-situ TEM observation of the response of ultrafine- and nanocrystalline-grained tungsten to extreme irradiation environments, Sci Rep 4 (2014) 4716. https://doi.org/10.1038/srep04716.

[126] L. Zhang, M. Sui, L. Zhang, K. Hu, D. Li, In situ TEM observations on morphological instability of ultrathin Pb films, Materials Science and Engineering: A 379 (2004) 1–6. https://doi.org/10.1016/j.msea.2003.08.126.

[127] H. Fröck, C. Rowolt, B. Milkereit, M. Reich, W. Kowalski, A. Stark, O. Kessler, In situ high-energy X-ray diffraction of precipitation and dissolution reactions during heating of Al alloys, J Mater Sci 56 (2021) 19697–19708. https://doi.org/10.1007/s10853-021-06548-z.

[128] H. Wiedemann, Synchrotron Radiation, in: H. Wiedemann (Ed.), Particle accelerator physics, Springer study ed., Springer, Berlin, Heidelberg, New York, Barcelona, Hong Kong, London, Milan, Paris, Singapore, Tokyo, 2003, pp. 647–686.

[129] P. Willmott, An introduction to synchrotron radiation: Techniques and applications, Second edition, John Wiley & Sons, Inc, Hoboken, NJ, 2019.

5. APPROACH AND EXAMINED QUESTIONS

Choosing to investigate metallic systems with general relevance to material science applications, the scope of possible materials is very broad. The operating conditions of MEMS chips do narrow down the feasible substances, particularly for FSC measurements where sample melting is ideally done to establish good thermal contact with sensor. This excludes higher melting alloy systems from reliable study with FSC. For in-situ TEM experiments, sample melting is not necessary for measurement, although observation of this transformation can be valuable to the material analysis.

In technological applications, metallic alloys almost always exist in non-equilibrium conditions, and a large concern of their research is in controlling and optimising the material state for the best performance. FSC and in-situ TEM offer high precision measurements at strong, non-equilibrium conditions, with such measurements being highly relevant to metallurgical fields both at fundamental and technological levels.

Al alloys, with a melting point somewhere below 660 °C, are well suited to the FSC apparatus, and their characterisation is extremely relevant to materials sciences. Metal additive manufacturing in particular involves very rapid temperature changes in its processing, and therefore can be usefully investigated by FSC. Moreover, pure metallic substances, which are readily available with well-defined thermophysical properties, can be measured for comparisons, calibrations, and to give an honest account of experimental design. In Chapters 6 and 7, pure lead and pure aluminium were employed as standards for results evaluation, and eutectic AlSi was investigated for specific material implications. The FSC experiments carried out are demonstrative in their experimental approach for reproducible, high precision measurements. Meanwhile, the results on heat capacity have particular relevance in understanding metallurgical changes at processing conditions far from equilibrium, with potential implications in computer modelling and simulation as well as processing parameters for additive manufacturing.

Sectioning of electron transparent samples for TEM experiments is normally accomplished using a focused ion beam (FIB) to perform precise cuts. On metals this results in some degree of ion implantation contaminating the sample, and creates defects and dislocations in the crystal lattice. Instead, Chapter 8 imitates the sample preparation techniques used in FDSC by preparing samples by hand, using a scalpel under a microscope. A sample of aluminium alloy is prepared in this way, placed upon a MEMS chip sensor for in-situ TEM, and characterised during a simulated paint bake heat treatment by BF-TEM, using the LAADF detectors, and by SAED and EDX methods. Particular attention in the manuscript is given to the sample preparation, with the cutting and placement procedure shown step-wise over several photos. This method is much faster than FIB preparation, Chapter 8's sample taking just 20 minutes to prepare from the electropolished disk and place on the MEMS sensor, and the avoidance of implantation contamination makes it an attractive option for metallurgical investigations.

6. Heat Capacity Measurements on Pure Lead via FDSC with UFS 1 Chip Sensors

With metallic systems gaining increasing interest in fast scanning calorimetry, particularly since the introduction of the commercially available high temperature calorimeter the Mettler-Toledo Flash DSC2+, it becomes more important to establish standardised procedures for common measurements. While specific heat capacity (c_p) measurements have been established on conventional DSC for decades, the particularities of MEMS-based experiments mean these methods are not suitable for fast scanning calorimetry. The following work describes and develops an optimal methodology for high precision heat capacity measurements on metallic systems. Using high purity lead, it is shown that without the proposed corrections to the measured heat flow, c_p cannot be evaluated. Further discussed are optimum parameters for obtaining a good c_p prediction, of which sample mass is found the most influential, and these hope to guide and improve future explorations on other metallic systems. The capability of fast differential scanning calorimetry in measuring heat flow and c_p far from equilibrium offers new experimental data for a rejuvenation in thermal analysis, and this publication explores the precision achievable using corrections to the measured heat flow and averaging multiple repetitions. A range of sample masses are investigated at a few different rates to assess the impact on the MEMS sensor's performance and inform similar experiments.

This work also helped to develop an experimental approach to examine the effects of vacancy defects in the heat flow signal. Such effects are small, even when involving high vacancy concentrations, and near the limit of the device's sensitivity; as such, the investigations into consistency and high precision aided the design of a feasible methodology. Experiments in this direction were run in parallel, and further informed by CALPHAD-based kinetic simulations using MatCalc.

Measurement of Heat Capacity via Fast Scanning Calorimetry—Accuracy and Loss corrections*

This study explores specific heat capacity (c_p) measurements via fast scanning calorimetry, with a focus on correcting measured heat flow by accounting for temperature dependent heat losses. Using MultiSTAR-UFS1 sensors with the Mettler-Toledo Flash-DSC 2+, c_p of Pb (99.998% purity) was measured in dependence of the sample mass and scanning rate. Masses from 0.3 to 5 µg were evaluated at rates of 100, 1000 and 2000 K s^{-1} in the temperature range -20 to 320 °C. Two correction methods are shown and compared to c_p results without corrections. Heat loss corrections are mandatory when measuring c_p, but are in particular important for low masses and rates. High consistency was found between the two proposed correction procedures giving good confidence in their viability. A slight but consistent overestimation of c_p compared to literature casts uncertainty upon the determined sample mass. Whilst the systems under study in this work encompass only pure Pb, the arguments and procedures of the shown method of c_p determination are applicable to any system in the absence of physical transformations.

6.1. Introduction

A non-adiabatic chip calorimeter based on a MEMS chip consisting of a heater and thermometer can be used for measurements in a wide heating and cooling rate range beyond the maximum scanning rate limit of conventional DSC. High heating rates can be achieved due to the low heat capacity of the measuring system. The non-adiabatic mode means that the sensor is surrounded by cold gas. This enables a fast heat reduction of the sensor and sample and consequently high cooling rates. This technique was developed by Christoph Schick in the last 20 years [1,2,3,4,5] and the technique is used for practically all kinds of metastable materials like polymers, metallic alloys, organic polymorphic substances, inorganic glass-formers, bio-based materials etc. An overview can be found in Ref. [7]. This paper is dedicated to Christoph Schick on the occasion of his 65th birthday.

Because of the small sample size in case of the fast scanning chip calorimetry, quantitative calorimetric measurements were not possible in the early time of this technique. The first problem was the determination of the sample size. For this the use of thermal effects has been recommended [8,9,10,11]. The first extensive investigations for quantitative determination of thermodynamic properties were performed by Cebe et al. [12,13,14] on polymer systems using the Flash DSC from Mettler-Toledo.

This technique is also used to study the metastable phase behavior in metallic alloys [15,16,17,18,19,20,21,22]. Particularly, the high heating rate makes it possible to study the thermodynamic properties of the metastable phases [23].

In this paper we study the accuracy and reproducibility of specific heat capacity measurements on the example of solid lead (Pb) via Fast Differential Scanning Calorimetry (FDSC) using the Mettler-Toledo

Flash-DSC 2+. Different possibilities of accounting for heat loss corrections and the influence of sample mass and applied rates are discussed.

6.2. METHODS

6.2.1. FDSC MEASUREMENTS

Experiments were performed on the Mettler-Toledo Flash-DSC2+ using conditioned and temperature-corrected MultiSTAR UFS 1 sensors. The sensor support temperature of the FDSC was set at 233 K using a Huber intracooler TC90. The furnace was purged with Ar of 5N purity at a flow rate of 60 ml min^{-1}.

For the Flash DSC 2+ the conditioning procedure has three tasks: The heating of the sensor to a certain temperature, a test for functionality and the determination of the electrical resistance of the heater. To do this the sensor support should be thermally equilibrated. This means the intracooler is switched off for at least 5 hours and the gas (Ar) flows before the conditioning procedure is applied. The temperature correction procedure measures the voltage of the thermocouples with respect to the sensor support temperature, Tss. For this procedure Tss has to be the ready temperature (here 233 K) and the gas has to be Ar (for UFH 1 sensors) and Ar or N_2 (for UFS 1 sensors). After correction different gasses can be used.

For exploring the potential to determine cp via FDSC, high purity Pb-foil (99.998 %) was chosen as a test material. The enthalpy of melting was measured at 100 K s^{-1}, in the interval 25 to 400 °C, and repeated 11 times. The first of these measurements was always rejected, since it is the least consistent. The remaining curves were used to produce an average melting peak, the integration of which yielded the average enthalpy of melting, ΔH_m. Sample mass (m_{FDSC}) was calculated using the enthalpy of fusion of Pb ($\Delta H_{fus}^{Pb} = 4.81\ kJ\ mol^{-1}$) and its molar mass ($A_r^{Pb} = 207.2\ g\ mol^{-1}$) from Smithell's Metals Reference Book [6], according to Eq. (6.1).

$$m_{FDSC} = \Delta H_m \times \frac{A_r^{Pb}}{\Delta H_{fus}^{Pb}} \qquad\qquad \text{(Eq. 6.1)}$$

FDSC samples were prepared by cutting a Pb-foil of 100 µm under a stereomicroscope to small pieces with weights of 0.3 to 5 µg. Table 6.1 depicts the exact weights and the used sensors.

Table. 6.1. Sample name, exact weights and the used sensors

Pb sample	Mass [µg]	UFS1 Sensor ID #
Pb0.3	0.286	XEN C17 42965
Pb1.3	1.26	XEN C17 42962
Pb2.6	2.56	XEN C17 42963
Pb5.3	5.26	XEN C17 42960

For all experiments to determine the specific heat capacity the samples were heated or cooled between -20 °C and 320 °C. Samples underwent simple heating-cooling cycles with heating rates of 100, 1000

and 2000 K s^{-1}. Each heating-cooling rate was cycled 11 times, and the ten most consistent curves were implemented. Before conversion to c_p, the measurement curves were shifted in the temperature to adjust for the observed melting onset of the lead samples at 100 K s^{-1}, which is normally a minor temperature correction in the order of a few °C.

6.2.2. HEAT FLOW SIGNAL ANALYSIS

In the conventional DSC the heat capacity of the sample is significantly lower than the furnace. Consequently, the behavior of the furnace can be widely corrected from the measuring curve by subtraction of the black curve measured without a sample [24]. In the case of FDSC measurements the situation is completely different. For the measurement of the bulk behavior of a gold based bulk metallic glass alloy the critical sample mass, at which the surface influence on the thermal behavior can be neglected, is in the order of 1 μg [10]. At such conditions the heat capacity of the sample is in the order of the heat capacity of the active zone of the FDSC sensor and consequently the empty sensor cannot be used as a blank curve. Due to the relatively large temperature difference between the hot sensor and the cold surrounding gas, the thermal losses between sample and reference side of the differential calorimeter cannot be completely compensated. Thus the measured heat flow can be described by

$$\phi = m \cdot c_p \cdot \beta + \phi_1 \qquad \text{(Equation 6.2)}$$

Where m is sample mass, c_p is specific heat capacity of the sample, β is heating rate and ϕ_1 is the heat loss function, which is in a good approximation independent of the scanning rate [8,12]. This relationship provides two straightforward ways to evaluate the heat loss function and thereby determine the actual heat flow into the sample, both of which are employed and compared in this work. The first method to find the heat loss function uses a low heating rate to minimize the sample term in Eq. 6.2, and thereby approximate the measured heat flow to the loss function (Eq. 6.3) [7].

$$\phi_{\beta \to 0} = \phi_1 \qquad \text{(Equation 6.3)}$$

Since this method utilizes a low rate to determine the correction function, it is termed here the *slow-rate correction*. Note that the heat losses are not necessarily equal on heating and cooling, and so a separate slow-rate correction function is found for heating and cooling, and these are separately applied to the measured heating and cooling scans at higher rates.

Conversely, at high heating rate the contribution of the heat loss function to the measured heat flow will be relatively small, meaning the measured heat flow more closely resembles the sample heat flow.

The second method uses the average heat flow from heating and cooling to determine the heat loss function (Eq. 6.4, 6.5), and is referred to as the *symmetry correction*.

$$\boldsymbol{\phi}_{avg} = \frac{(m \cdot c_p \cdot \beta + \boldsymbol{\phi}_{1,h}) + (m \cdot c_p \cdot (-\beta) + \boldsymbol{\phi}_{1,c})}{2} \qquad \text{(Equation 6.4)}$$

$$\boldsymbol{\phi}_{avg} = \frac{\boldsymbol{\phi}_{1,h} + \boldsymbol{\phi}_{1,c}}{2} = \boldsymbol{\phi}_1 \qquad \text{(Equation 6.5)}$$

where $\boldsymbol{\phi}_{1,h}$ and $\boldsymbol{\phi}_{1,c}$ are the heat loss functions for the heating and cooling measurement, respectively.

The calculated loss function can now be used to correct the heat flow, and the conversion to specific heat accomplished by dividing by the programmed heating rate and the sample mass (Eq. 6.6).

$$\frac{\boldsymbol{\phi} - \boldsymbol{\phi}_1}{m \cdot \beta} = c_p \qquad \text{(Equation 6.6)}$$

The latter procedure was recommended by Zhuravlev and Schick [8].

6.3. RESULTS

6.3.1. MEASURED CURVES AND C_P CONVERSION WITHOUT CORRECTION

Shown in Figure 6.1 are the measured heat flow curves from simple heating-cooling cycles at three different rates for four different masses. At each rate the heating-cooling segments were measured over 11 cycles, and the 10 most consistent curves are displayed and used in further calculations. "H100" denotes the measured heating cycles at 100 K s^{-1} and "C100" the cooling cycle measurements at 100 K s^{-1}. Similarly, those labelled 1000 and 2000 denote measurements at rates of 1000 and 2000 K s^{-1}. This convention is used throughout the figures to differentiate between the multitude curves. Good reproducibility is evinced by the consistency of the measured curves. The measured heat flow increases with increasing mass and rate (since more power is needed to achieve heating in those cases). Also worthy of note is the impact of the initial thermal stabilization on the measured heat flow, causing a perturbation at the beginning of the scanning run (at low temperatures for heating segments and at high temperatures for cooling segments). Due to the increased thermal lag this switching behavior of the heat flow becomes greatly exaggerated at higher masses and rates, and has a clear and noticeable impact on the range of useful results.
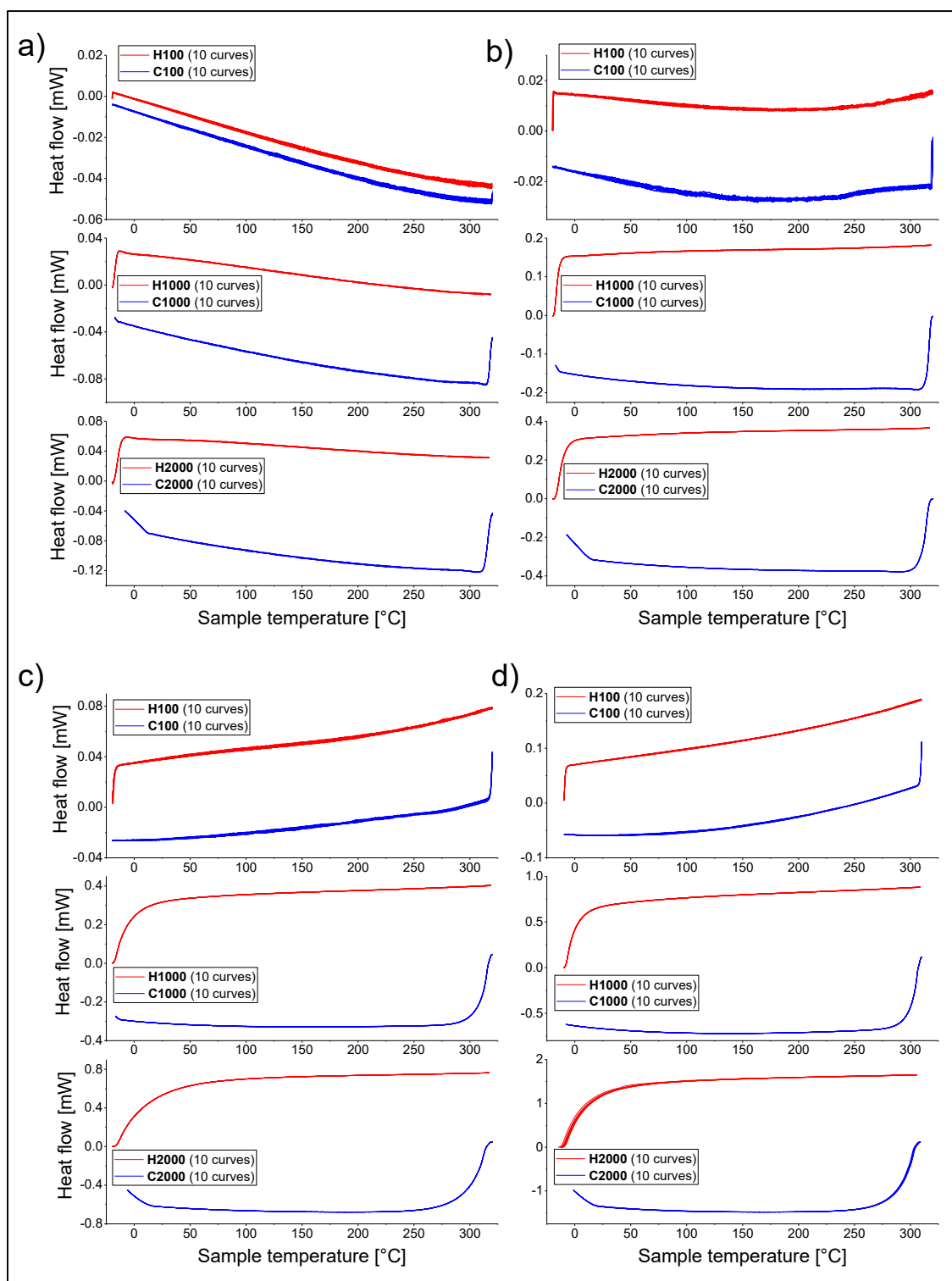
Figure 6.1: Measured raw data heat flow curves for Pb masses Pb0.3 (a), Pb1.3 (b), Pb2.6 (c) and Pb5.3 (d) at linear heating and cooling rates of 100, 1000 and 2000 K s^{-1}. Ten curves are displayed at each rate to show reproducibility. At higher rates and masses, the levelling of the machine affects a wider temperature range.

In Figure 6.2, a single heat flow curve was taken from each of those measured above (1 heating and 1 cooling curve from each mass and rate) and converted to c_p, dividing by heating rate and sample mass. It is clear from Figure 6.2 that measurements at 100 K s^{-1} show no correlation to literature data, and in all cases the sample of lowest mass, Pb0.3, has the poorest resemblance to the expected values. The samples of larger mass perform better at the elevated rates 1000 and 2000 K s^{-1}, particularly on heating scans, though still fall short of usefully describing c_p. Interestingly, the H1000 curve for mass Pb1.3 in Figure 6.2 (b) correlates very well with the literature prediction, however since this accuracy is not found in any other case the result is considered remarkable, but appears to a result by chance. It is clearly shown then, that direct evaluation of the measured heat flow curves cannot determine the heat capacity without correction procedures.
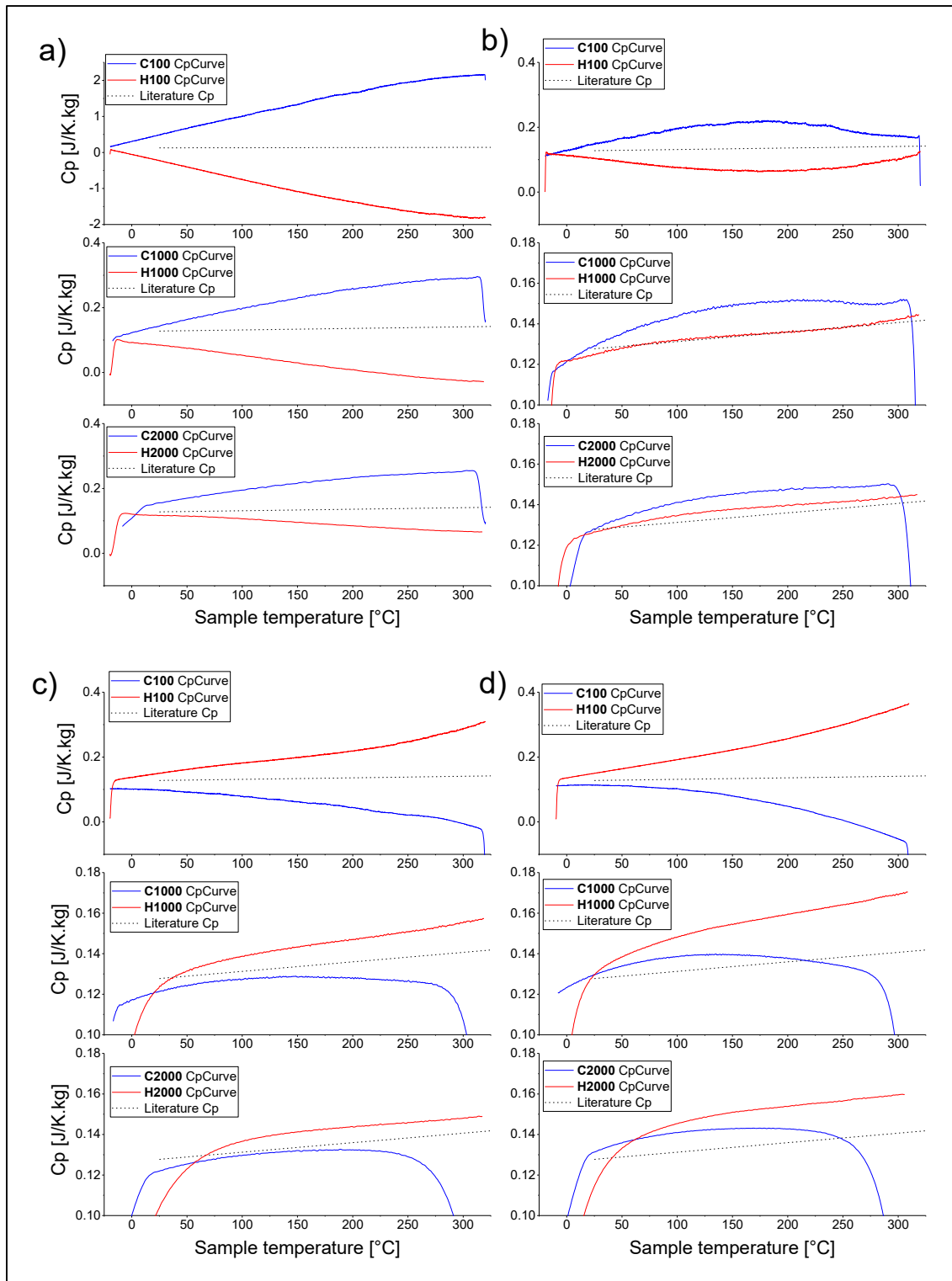
Figure 6.2: Specific heat capacity curves calculated from raw data for samples Pb0.3 (a), Pb1.3 (b), Pb2.6 (c) and Pb5.3 (d), presented as in Figure 6.1. A single sample curve from each linear heating and cooling rate was used in the conversion to specific heat capacity, and is compared to [6]. Low rate measurements show no correlation to literature expectation, and the smallest sample mass Pb0.3 is worst in all cases. The larger masses at higher rates fare better (note the smaller scales) though leave great room for improvement. The aforementioned stabilisation effects are also strongly visible here, clearly impacting the range of useful results.

6.3.2. PROCEDURE OF HEAT LOSS CORRECTIONS VIA SLOW-RATE AND SYMMETRY APPROACHES

According to Equations 6.2 and 6.3, the heat flow measured at sufficiently low rate can be approximated to only the heat losses. Since the slow-rate employed in this work (1 K s^{-1}) is two orders of magnitude lower than the slowest rate of interest, the sample effects are also 2 orders of magnitude lower and this is certainly sufficiently low to use such a curve as a base line. Figures 6.3 and 6.4 show the implementation of the slow-rate correction method by producing the loss correction curves (Fig. 6.3) and subtracting them from the measured heat flow data (Fig. 6.4) for the relevant mass. First, heating and cooling scans at 1 K s^{-1} are separately averaged using the most consistent curves from the results. These are in fact already the loss correction curves, however before using them in any summation it is pertinent to remove signal noise by smoothing. To check that smoothing has not removed any real signal artefact, a smooth assessment is performed by subtracting the actual curves by their smoothed counterparts. The result shows what has been removed in the smoothing operation and should only be low intensity noise oscillations, which is indeed the result in Fig. 6.3(c) (note the μW scale). The smoothed averages produced are then subtracted from the sample's heat flow data at higher rates to produce the slow-rate heat loss corrected heat flow. The heating scans are subtracted by the heating slow-rate correction curve, and the cooling scans are subtracted by the cooling slow-rate correction curve.
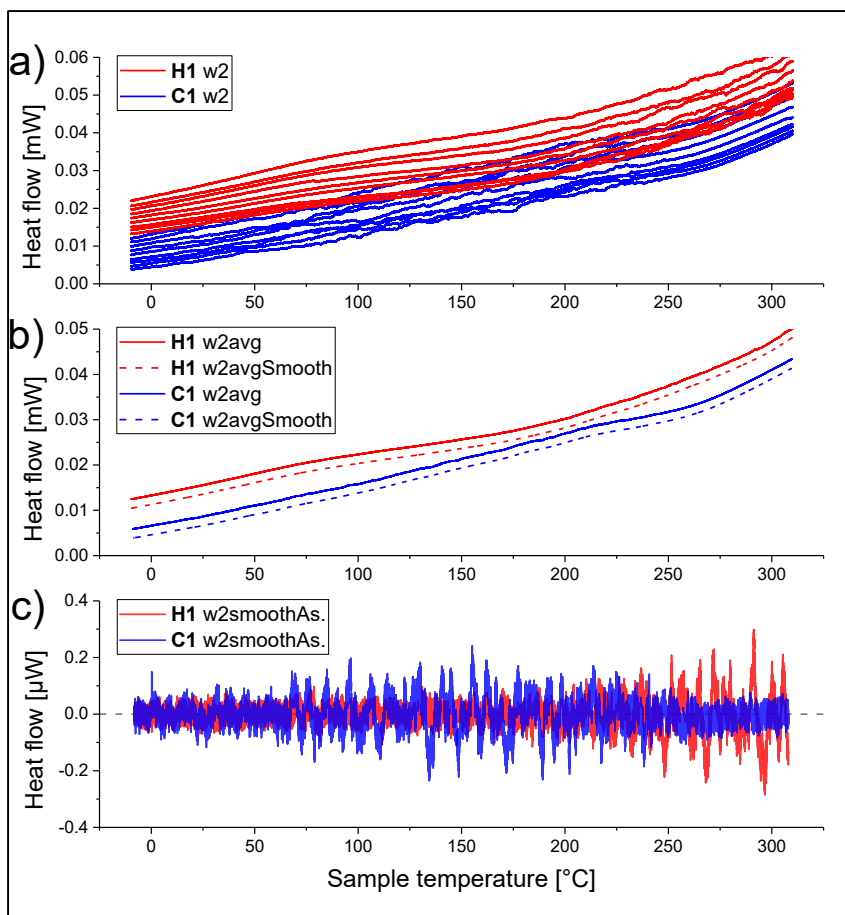
Figure 6.3: Formation of the slow-rate loss correction curves for sample Pb2.6. (a) the measured curves at 1 K s^{-1}, (b) the average of the heating and cooling scans and their 1000-point smoothed counterparts, and (c) the smoothing assessed by subtraction of the smoothed curve from the unsmoothed average.
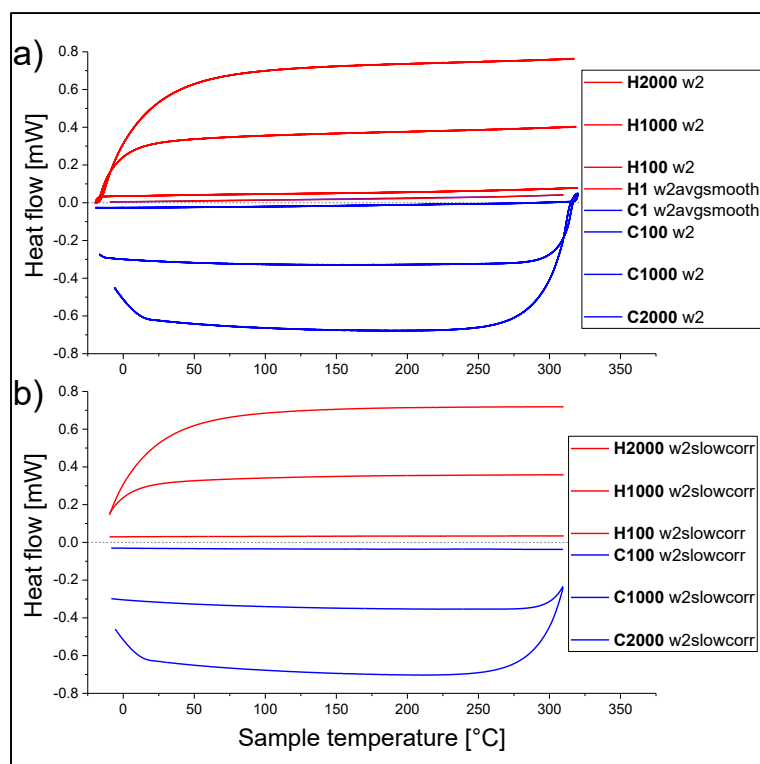
Figure 6.4: Slow-rate correction applied to sample Pb2.6. (a) shows the 10 measured curves at individual rates before the subtraction of the slow-rate loss correction curve, and in (b) the slow-rate subtraction is performed to all individual curves and then the corrected curves are averaged at each respective rate.

Figure 6.5 shows the production and implementation of the symmetry correction curves for sample Pb2.6 at the three rates of interest. Contrary to the slow-rate correction, the symmetry correction method uses a different correction curve for each rate measured. To produce the symmetry loss-correction curve (see Eq. 6.4) the total average of the heating and cooling scans at the same rate is found, displayed in green in the left part of Fig. 6.5 (a-c). This correction curve is then subtracted from the average heating and average cooling scans, separately. This yields the symmetry corrected heat flow (see right part of Fig. 6.5 (a-e)). Due to the averaged nature of the loss correction curve, the symmetry corrected heat flow for heating and cooling scans are in fact equal and opposite in magnitude. Since the heating and cooling rates are also equal and opposite in magnitude, conversion to c_p produces two identical curves. Therefore, only one of the curves is needed to calculate the symmetry corrected c_p curve.
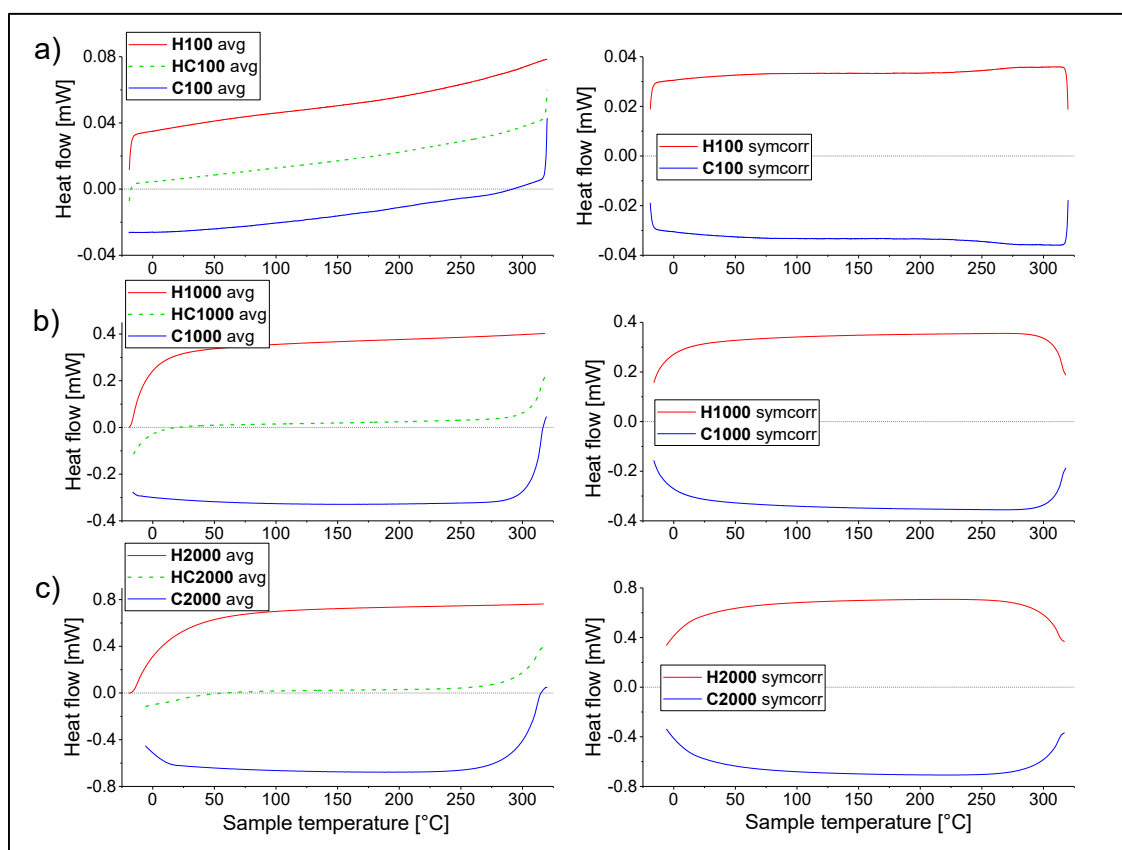
Figure 6.5: Symmetry correction method applied to Pb2.6 at a) 100, b) 1000 and c) 2000 K s⁻¹. The left panels show the average of the measured heating and cooling scans, and their average which is the symmetry loss-correction curve (marked as "HCxxx avg" in the legend). The heating scans always show positive heat flow, and cooling scans always negative. The right panels show the result of subtracting the symmetry correction from the measured heat flow. Note that the subtraction yields two identical curves of opposite sign, therefore only one need be evaluated to obtain the corrected c_p curve.

6.3.3. CORRECTED C_P CURVES

Having applied the various curve corrections to the measured heat flow, conversion to c_p was then performed by dividing by heating rate and sample mass according to Eq. (6.5). The results are presented in Fig. 6.6, using similar scaling to Fig. 6.2, and show an all-round huge improvement on the uncorrected results. The 100 K s⁻¹ curves show the most significant improvement in terms of magnitude, and all the curves show improved linearity after the corrections. Interestingly there is little to distinguish either of the correction methods as superior, though this actually lends reliability to the results. Since both slow-rate and symmetry correction methods aim to determine the real sample heat flow, they should theoretically be identical, and this is more or less what is observed. Furthermore, this consistency between correction methods helps provide an explanation for the overestimation of the c_p, which is noticeable in all of the below figures: as both methods give highly consistent results, the methodology of the corrections seems sound; if the heat flow corrections are not accountable for the overestimation, then it must be introduced in the c_p conversion; if the programmed heating rate is indeed the real heating rate, the only remaining influential parameter is the sample mass. The sample

mass was determined from an average melting peak at 100 K s^{-1}, using $\Delta H_{fus}^{Pb} = 4.81\ kJ\ mol^{-1}$ as stated in [2]. Providing this is accurate, the underestimation of the sample mass must be introduced during the measurement and evaluation of the melting peak.
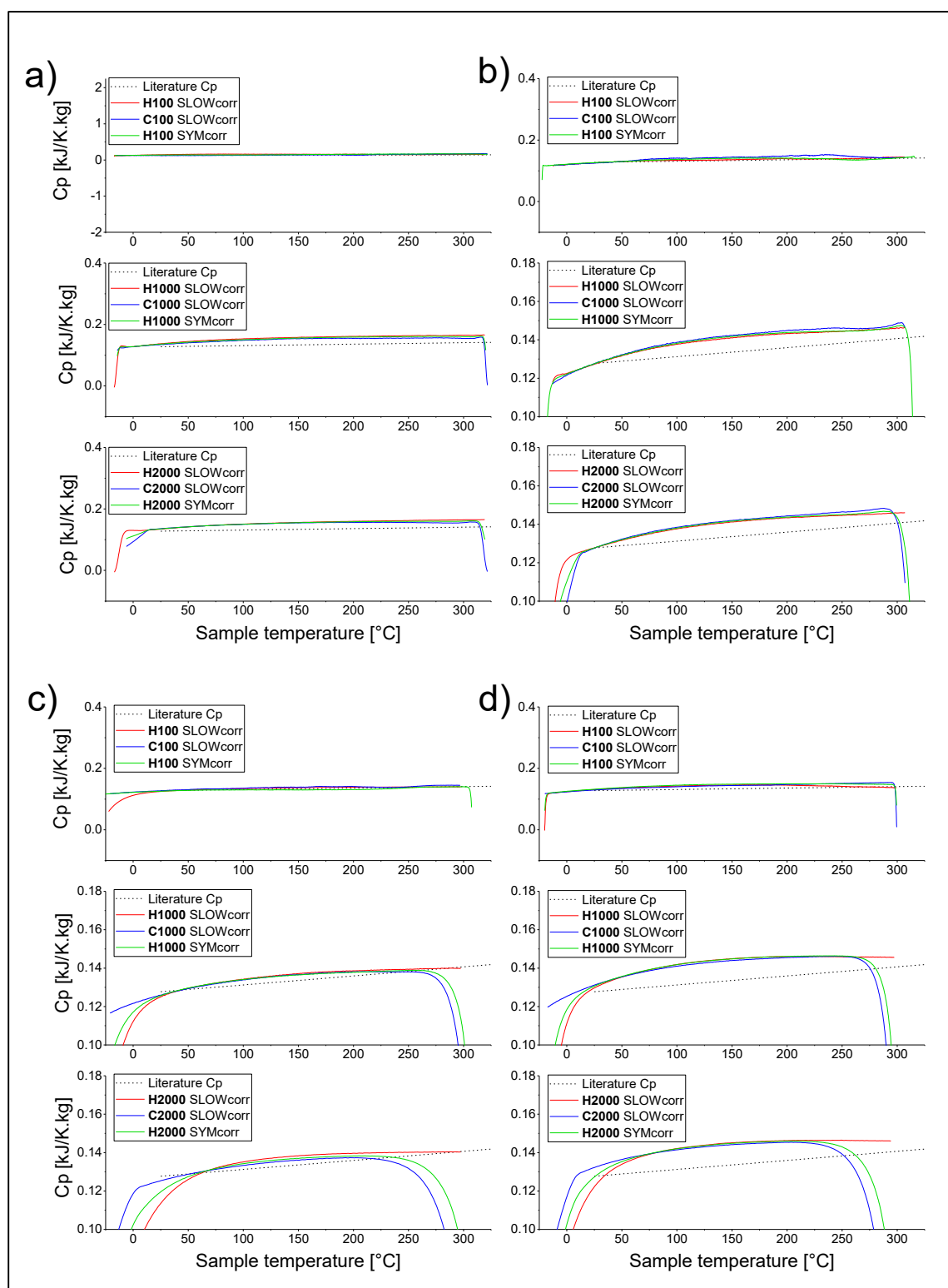
Figure 6.6: Specific heat capacity curves calculated after the proposed heat flow correction methods for all masses at all rates. Plots (a), (b), (c) and (d) show masses Pb0.3, Pb1.3, Pb2.6 and Pb5.3 respectively. Rates of 100, 1000 and 2000 K s^{-1} are shown successively in each three plot group. The dotted literature line is produced from [6]. Scaling of each plot matches that of the raw data specific heat curves in Figure 6.2. Both slow-rate and symmetry corrections yield very consistent results and show enormous improvement on calculated c$_p$ in the absence of corrections. Best results are observed for mass Pb2.6, though in all cases better linearity is achieved. At higher masses and rates, thermal lag reduces the effective range of results to approximately 50-200 °C.

6.4. DISCUSSION

Beyond the numerical comparisons of c_p for the various samples and scanning rates to the literature, the results gathered present several elements for further discussion in the context of deriving some general optimization rules that can be applied to similar experiments on different systems. The programmed parameters (heating rate and temperate range), the uncertainty of the mass determination, optimum sample mass and the correction method must all be considered to achieve the most accurate c_p result.

The near-identical results from the corrected c_p curves lend credence to both the symmetry and slow-rate correction procedures, even more so than had one been superior in matching the literature expectation. In each measurement instance (given mass and rate), the actual loss function will of course be the same, but the mathematical procedure by which it is calculated differs between the two methods. Whilst there is always a slight overestimation of c_p, the consistence between the methods validates the reliability and practical applicability of both. And, as mentioned before, if the loss correction is not at fault for the overestimation then the determined sample mass used in the c_p conversion (Eq. 6.6) is most likely the culprit. An improvement on the mass determination might be achieved by evaluating the mass at a variety of heating rates, not just 100 K s^{-1} used here, or perhaps determining the mass through means other than the melting peak.

Since both methods are shown to be a sound choice for predicting c_p, when seeking to study a different system either correction procedure could be implemented; however, since the symmetry correction does not require slow-rate measurements, it is less time consuming and is likely preferred for most systems. However, in case of transformations, the slow-rate determination of the baseline may be more appropriate.

Figure 6.7 shows the calculated c_p values at 150 °C for the four masses at each rate, and allows comparison between the various measurement parameters. Each point in Fig. 6.7 corresponds to an individual mass and rate, and is the average of the three c_p values produced from the symmetry and slow-rate corrections. Since the two methods give largely similar values in each case, and the c_p curves are all stable and consistent at this temperature, it is appropriate to compare their averages in this manner. One thing is abundantly clear from this diagram: sample mass has a profound effect on the accuracy of the end result. Sample Pb2.6 produces good results, however at higher and lower mass, divergence from the literature value becomes significant. The divergence at low mass (Pb0.3) likely originates from its low heat flow and high signal to noise ratio. This exaggerates the inconsistencies and impact of baseline effects in the signal, and therefore interferes with accurate enthalpy determination for the melting peak. Note that divergence at high mass is only expressed by one point in Fig. 6.7 and less clear. A probable factor in the accuracy reduction may be the impact of thermal lag and temperature gradients within the sample, which become increasingly exaggerated at higher mass. Whilst the Pb system studied showed 2.56 μg to be close to optimum mass, other metallic systems may differ. The sample's physical size could be part of the reason for Pb2.6's suitability, in which case

other systems would differ according to their density. Furthermore, experiments using the new UFH 1 high temperature sensors would certainly exhibit different optimum mass conditions, and a variety of samples would need investigation to determine the most suitable mass.

The second conclusion that can be drawn from Fig. 6.7 concerns heating rate. In each case, 100 K s^{-1} is seen to be the least consistent. Whilst these inconsistencies are not so significant for Pb1.3, 2.6 and 5.3, for the lowest mass Pb0.3 a large separation of this result is seen compared to those at higher rate. This separation is likely also caused by the small magnitude of the heat flow of the sample compared to the sensor baseline and the worse signal to noise ratio. For c_p measurement of small sample masses (e.g. thin films [25]), it would be best to avoid low heating rates and employ the symmetry correction, along with a very careful determination of the sample mass. So, while a higher sample signal can be achieved at higher heating rate, this also increases the impact of thermal lag in the system and exaggerates the aforementioned stabilization effects. A rate of 1000 K s^{-1} appears a good compromise between these factors for the UFS1 sensors. To compensate for the impact of these stabilization effects on the range of useful results, the temperature range of the measurement can be increased. The possible temperature range is limited however by the chip sensor's operational range, and the melting point of the sample. It is of course possible to heat through and beyond the melting point, or even collect data on the liquid sample, though this may reduce consistency in the system. Also, the solidification peaks can appear over a broad temperature range, and so reduce the effective result range in that manner.
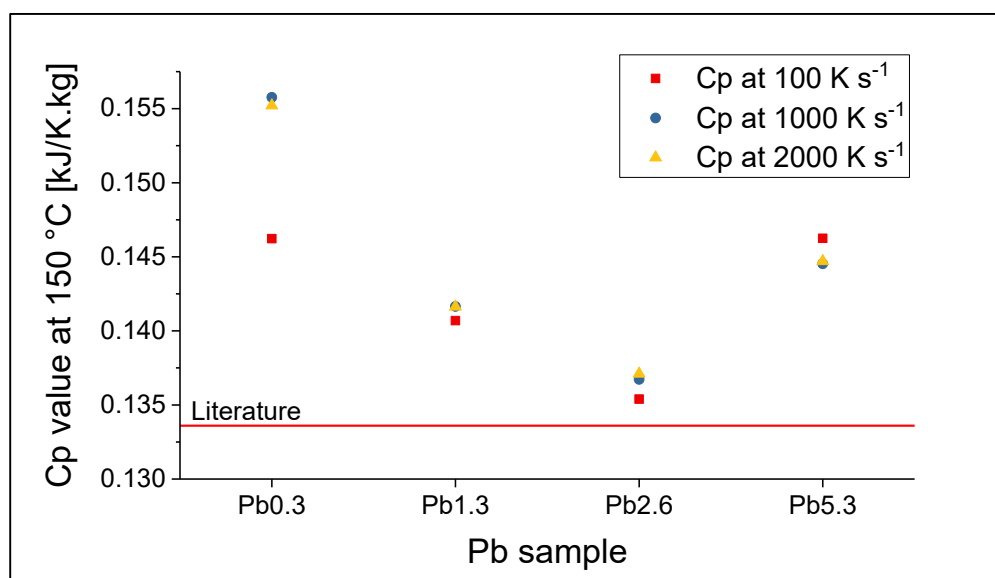

Figure 6.7: Sample mass versus c_p at 150 °C for the four samples at 100, 1000 and 2000 K s^{-1} compared to [6]. Each point is an average of the three results from the symmetry and slow-rate corrections on heating and cooling from Fig. 6.6. The sample Pb2.6 achieves the best results, while high and low masses show higher divergence from the literature value of c_p.

6.5. CONCLUSIONS

In summary, FDSC can be efficiently used to measure specific heat capacity when appropriate heat loss corrections and measurement parameters are applied:

- Both the symmetry and slow-rate correction methods of the heat loss give similar results. Such corrections are in particular important at low sample masses and rates.

- The sample mass shows a stronger influence on the determined c_p-value, than the used heating rate. Intermediate sample masses (2.6 μg for Pb) show the best correlation with literature values for c_p.

- Slight, but consistent overestimation of c_p suggests a small inaccuracy in mass determination.

In the study pure Pb was used, but the applied strategy can serve as a guideline for determining c_p in any other system.

6.6. REFERENCES

[1]   S.A. Adamovsky, A.A. Minakov, C. Schick, Scanning microcalorimetry at high cooling rate, Thermochim. Acta 403 (2003) 55–63.

[2]   A.A. Minakov1, D.A. Mordvintsev, C. Schick, Melting and reorganization of poly(ethylene terephthalate) on fast heating (1000 K/s), Polymer 45 (2004) 3755–3763.

[3]   E. Zhuravlev, C. Schick, Fast scanning power compensated differential scanning nano-calorimeter: 1. The device, Thermochim. Acta 505 (2010) 1-13.

[4]   E. Zhuravlev, V. Madhavi, A. Lustiger, R. Androsch, C. Schick, Crystallization of polyethylene at large undercooling, ACS Macro Lett., 5 (2016) 365-370.

[5]   E. Tarani, D.G. Papageorgiou, C. Valles, A. Wurm, Z. Terzopoulou, D.N. Bikiaris, C. Schick, K. Chrissafis, G. Vourlias, Insights into crystallization and melting of high density polyethylene/graphene nanocomposites studied by fast scanning calorimetry, Polymer Testing 67 (2018) 349-358.

[6]   W. F. Gale, T. C. Totemeir (Eds.), Smithell's Metals Reference Book (8th edition), Elsevier Inc., Burlington, 2004.

[7]   C. Schick and V.B.F. Mathot (Eds.), Fast Scanning Calorimetry, Springer 2016, https://doi.org/10.1007/978-3-319-31329-0.

[8]   E. Zhuravlev, C. Schick, Fast scanning power compensated differential scanning nano-calorimeter: 2. Heat capacity analysis, Thermochim. Acta 505 (2010) 14-21.

[9]   J.E.K. Schawe, Influence of processing conditions on polymer crystallization measured by fast scanning DSC, J. Thermal. Anal. Calorim. 116 (2014) 1165-1173.

[10]   [S. Pogatscher, D. Leutenegger, A. Hagmann, P.J. Uggowitzer, J.F. Löffler, Characterization of bulk metallic glasses via fast differential scanning calorimetry, Thermochim. Acta 590 (2014) 84-90.

[11]   J. E.K. Schawe, S. Pogatscher, Material Characterization by Fast Scanning Calorimetry: Practice and Applications, In: C. Schick and V.B.F. Mathot (Eds.), Fast Scanning Calorimetry, Springer (2016), p. 3-80, https://doi.org/10.1007/978-3-319-31329-0_1

[12]   P. Cebe, B.P. Partlow, D.L. Kaplan, A. Wurm, E. Zhuravlev, C. Schick, Using flash DSC for determining the liquid state heat capacity of silk fibroin, Thermochim. Acta 615 (2015) 8–14.

[13]   P. Cebe, D. Thomas, J. Merfeld, B.P. Partlow, D. L. Kaplan, R.G. Alamo, A. Wurm, E. Zhuravlev, C. Schick, Heat of fusion of polymer crystals by fast scanning calorimetry, Polymer 126 (2017) 240-247

[14] D. Thomas, E. Zhuravlev, A. Wurm, C. Schick, P. Cebe, Fundamental thermal properties of polyvinyl alcohol by fast scanning calorimetry, Polymer 137 (2018) 145-155

[15] J. Orava, A. L. Greer, B. Gholipour, D. W. Hewak, C. E. Smith, Characterization of supercooled liquid $Ge_2Sb_2Te_5$ and its crystallization by ultrafast-heating calorimetry, Nat. Mater. 11 (2012) 279–283.

[16] J.Q.Wang, N.Chen, P.Liu, Z.Wang, D.V.Louzguine-Luzgin, M.W.Chen, J.H.Perepezko, The ultrastable kinetic behavior of an Au-based nanoglass, Acta Mater. 79 (2014) 30-36.

[17] S. Pogatscher, P. J. Uggowitzer, and J. F. Löffler, In-situ probing of metallic glass formation and crystallization upon heating and cooling via fast differential scanning calorimetry, App. Phys. Lett. 104 (2014) 251908

[18] S. Pogatscher, D. Leutenegger, J. E. K. Schawe, P. J. Uggowitzer, J. F. Löffler, Solid-solid phase transitions via melting in metals, Nat. Commun. 7 (2016) 11113

[19] B. Chen, J. Momand, P.A. Vermeulen, B.J. Kooi, Crystallization Kinetics of Supercooled Liquid Ge−Sb Based on Ultrafast Calorimetry, Cryst. Growth Des. 16 (2016) 242−248

[20] P.A. Vermeulen, J. Calon, G.H. ten Brink, B.J. Kooi, Combining Ultrafast Calorimetry and Electron Microscopy: Reversible Phase Transformations in SeTeAs Alloys, Cryst. Growth Des. 18 (2018) 3668−3673

[21] J.H. Perepezko, T.W. Glendenning, J.-Q. Wang, Nanocalorimetry measurements of metastable states, Thermochimica Acta 603 (2015) 24–28

[22] H. Weber, J. Orava, I. Kaban, J. Pries, A.L. Greer, Correlating ultrafast calorimetry, viscosity, and structural measurements in liquid GeTe and Ge15Te85, Phys. Rev. Mat. 2 (2018) 093405.

[23] G. Kurtuldu, K.F. Shamlaye, J. F. Löffler, Metastable quasicrystal-induced nucleation in a bulk glass-forming liquid, PNAS 115 (2018) 6123–6128.

[24] G.W.H. Höhne, W. Hemminger, H.-J. Flammersheim, Differential Scanning Calorimetry: An Introduction for Practitioners, Springer (2003).

[25] J. Yu, Z. Tang, F. Zhang, H. Ding, Z. Huang, Heat capacity of copper thin films measured by micropulse calorimeter, ICNMM 2008, Darmstadt, Germany, June 23-25 2008.

7. HEAT CAPACITY MEASUREMENTS ON AN ALUMINIUM ALLOY VIA FDSC WITH UFH 1 CHIP SENSORS

This publication examines the heat capacity of pure aluminium and a eutectic AlSi12 alloy during rapid temperature changes up to 30,000 K s^{-1}. The high temperature UFH 1 sensors are used, and high precision and reproducibility is and achieved by implementing a correction to the measured heat flow. The correction accounts for the systematic heat losses and is found from low heating rate measurements. The experiments on AlSi12 alloy indirectly reveal the microstructural changes occurring during rapid processing by their impact on apparent heat capacity. Apparent heat capacity curves are chosen for the material assessment since they have more general scientific relevance than just the specific sample heat flow. Furthermore, these curves may be more accurately considered as the heat flow curves normalized to heating rate and sample mass, and contains contribution from specific heat capacity and other thermophysical processes. In this way, rapid precipitation mechanisms and kinetics can be conveniently examined by FDSC, and in combination with other characterisation techniques could be extremely revealing for instance for metal additive manufacturing (MAM).

Fast Differential Scanning Calorimetry to Mimic Additive Manufacturing: Specific Heat Capacity Analysis of Aluminium Alloys*

Eutectic AlSi12, commonly used in casting and in additive manufacturing, is investigated with Fast Differential Scanning Calorimetry to determine the impact of different cooling rates from the liquid state upon the apparent specific heat capacity on subsequent heating. A heat flow correction strategy is developed and refined for the reliable and precise measurement of sample heat flow using chip sensors, and assessed by the evaluation of results on pure (99.999 %) aluminium. That strategy is then applied to the study of the AlSi12 eutectic alloy, and rate-dependent perturbations in the measured apparent specific heat capacity are discussed in terms of Si supersaturation and precipitation. Several cooling rates were implemented from -100 to $-30,000$ K s^{-1}, and subsequent heating ranged from $+1000$ to $+30,000$ K s^{-1}. After rapid cooling, a drop in AlSi12 apparent specific heat capacity is found on heating above ~400 °C, even at rates of $+10,000$ K s^{-1}, a result which has high relevance in metal additive manufacturing where similarly fast temperature cycles are involved. Literature data, temperature modulated DSC and CALPHAD simulations on the heat capacity of AlSi12 are used to provide comparative context to the results from Fast Differential Scanning Calorimetry.

7.1. INTRODUCTION

A well-established technique to measure the thermodynamics and kinetics of phase transformations in various materials is Differential Scanning Calorimetry (DSC). However, the addenda heat capacity and the resulting thermal lag of conventional DSC apparatus limits the scanning rates to several hundred Kelvin per minute [1,2]. This is too slow for studying the solidification of many technical processes like injection moulding, welding and laser sintering at realistic rates. To increase the applicable scanning rate range for heating and cooling by more than 4 decades, the non-adiabatic chip-based Fast DSC (FDSC) was developed [3–5]. An example which demonstrates the potential of this technique is discussed by Cebe et.al. [6,7]. There, the specific heat capacity of silk fibroin was successfully measured in the melt far above its normal decomposition temperature, since the heating rate of FDSC was high enough to shift decomposition to higher temperatures. For determination of the specific heat capacity, this was coupled with a method for heat loss correction [6,8–12].

The major advantages of FDSC originate from the high heating and cooling rates possible compared to conventional DSC. These capabilities have fostered particular interest in the polymer and glass communities since the advent of FSC in the nineties [13], as kinetic-based crystallisation effects can be investigated with relative ease over a much broader range of temperature rates [14]. The ability to implement such a broad range of cooling rates means that the impact of thermal treatments can be investigated in great depth and detail. These capabilities also hold many advantages for investigation of metallic systems, whose properties vary due to microstructural or phase content differences brought

about either by mechanical or thermal manipulation. FSC provides an opportunity to control a sample's state through implementation of user defined temperature programs. Mettler-Toledo's fast scanning calorimeter, the Flash DSC 2+ launched in 2019, covers temperatures from –100 to +1000 °C and rates of –40,000 to +50,000 K s^{-1} and has great potential to study many materials in all fields of science. Metallic materials have been investigated with FSC in several contexts in materials science, including bulk metallic glasses (BMG) [15–18] and additive manufacturing [19–21] as well as nucleation and crystallisation [22,23].

The high heating and cooling rates possible when using the Flash DSC 2+ with the MultiStar UFH 1 sensors hold some particular relevance for metal additive manufacturing (AM), since the associated processing techniques (e.g. in laser powder bed fusion (LPBF)) implement temperature changes in the tens of thousands of Kelvin per second [24]. Calorimetric measurement at such rates is only possible using FSC. Current approaches for assessment in AM often rely on mechanical testing of printed parts [25,26] or on metallographic [25] investigations of, for example, single scan tracks [27,28]. Single scan tracks are produced when the laser melts the powder bed in a line, and are then cut, polished and analysed. They require only a small amount of alloy powder to produce while still providing insight on the nature of the melt pool and suitable scanning parameters; however, direct insight into thermo-physical properties during the process is rarely given. FSC measurements have already provided some insight into precipitation mechanisms at high undercooling for example in the works by Yang et al. [21] and Zhuravlev et al. [20]. Other contemporary research in AM is based on computational modelling and simulations. For this, heat capacity data is typically implemented with temperature dependent equilibrium data, as measured via conventional DSC methods, or even as a single fixed value. FSC analysis on the other hand allows direct calorimetric measurement at process-comparable cooling rates, and therefore can provide measurements at highly relevant non-equilibrium conditions.

Recently, the authors reported on experiments and correction methods to determine the heat capacity of pure Pb (99.999 %) using the low temperature MultiStar UFS 1 chip sensor [9]. However, the high temperature UFH 1 chip sensors constitute a redesign with a thinner membrane, smaller heated area, and gold instead of aluminium to withstand higher temperatures. This demands a reassessment of optimal measurement parameters. The most obvious of these is the lower sample mass required versus the UFS 1 chip sensors, which helps to achieve much faster heating and cooling rates. Beyond this, according to the user manual for the Flash DSC 2+, UFH 1 sensors tend to have shorter lifespans before breakage, particularly when operating at high temperatures. Experiment design should ideally take this into account to best utilise the chip sensors.

The present work explores a methodology of precise, reproducible heat capacity measurements with the high temperature MultiStar UFH 1 chip sensors, the basis of which revolves around measuring and correcting for systematic heat losses. For the determination of such measurement strategy, pure aluminium is studied. To demonstrate application of this strategy in practice, we study the AlSi12 alloy common in casting and AM. The present work focuses on precise measurements of AlSi12 powder

and determination of the effect of different cooling and heating rates upon the measured heat capacity. The results use the fact that the resultant curves are not simply the materials c_p, but the superposition of the heat capacity and any other thermal effects at that moment, to draw conclusions about the material changes involved during rapid processing.

7.2. EXPERIMENTAL

7.2.1. CALPHAD CALCULATIONS

The equilibrium heat capacity of AlSi12 was calculated with FactSage 8.0 [29] via the Equilib module and the function builder using the light metal alloy database FTlite 2020 [30].

7.2.2. FAST DIFFERENTIAL SCANNING CALORIMETRY

The FDSC analysis was performed using a Mettler-Toledo Flash-DSC 2+ equipped with an intracooler on conditioned and corrected MultiStar UFH 1 high temperature sensors under an argon flow of 80 mL min^{-1}. The sensor support temperature was set to –90 °C.

7.2.3. MATERIALS

Aluminium foil was obtained from Alfa Aesar (Karlsruhe, Germany) at 99.9996% purity and 38±7 μm thickness. AlSi12 powder (aluminium with 12 wt% silicon) was sourced from inspire AG (Zurich, Switzerland).

7.2.4. FDSC SAMPLE PREPARATION

Samples of pure aluminium were prepared from 38 μm foil using a scalpel to cut an appropriately sized piece (~50 μm) and positioned using a hair stylus. The sample was then melted and solidified several times to achieve a consistent interface and provide good thermal contact with the sensor. The sample preparation for AlSi12 simply required isolating a single particle of the alloy powder usually used for AM and positioning it on the sensor. A very small quantity of a silicon oil spread on the sensor's sample area aided in achieving the ideal sample position and helped to stop the sample jumping away during first heating. The silicon oil is vaporized during the first heating program [31], where the sample is again melted and solidified several times.

7.2.5. SLOW-RATE HEAT FLOW CORRECTION

Building on the work in [9], where the necessity of heat loss correction was demonstrated, two approaches for determining the system's heat losses were considered. One, the so-called symmetry correction, uses a symmetric heating and cooling program to evaluate the temperature dependant heat loss curve. However, this approach is only suitable without the occurrence of irreversible transitions in a sample that could impact the heat flow (e.g. in a super saturated solid solution). Since the present work should not only be suitable for pure metals (i.e. here Al), but also for alloys (i.e. here the eutectic AlSi12), the symmetry approach was rejected in favour of the slow-rate approach for heat loss

determination. Equation (7.1) relates the measured heat flow ($\phi(T)$) to the sample mass (m), the specific heat capacity ($c_p(T)$), the heating rate (β) and the systematic heat losses ($\phi_{loss}(T)$) [10].

$$\phi(T) = m \cdot c_p(T) \cdot \beta + \phi_{loss}(T) \qquad (7.1)$$

The slow-rate approach approximates the heat flow at a very low rate, e.g. +1 K s⁻¹, to represent the systematic heat losses, turning Equation (7.1) into (7.2) [9,10].

$$\phi_{\beta=1\,K\,s^{-1}}(T) \approx \phi_{loss}(T) \qquad (7.2)$$

This approximation is further validated when considering the comparative magnitude of the sample signal in the slow- and rapid heating scans. That is, the sample contribution in the 1 K s⁻¹ slow scan is 3-4 magnitudes smaller than in the rapid rate curves [9, 10], causing a negligible error of less than 0.1 %.

Having determined the heat loss function, the measured heat flow can then be corrected according to Equation (7.3). Dividing by the programmed heating rate and the determined sample mass then yields the heat capacity curve.

$$\phi(T) - \phi_{loss}(T) = m \cdot c_p(T) \cdot \beta \qquad (7.3)$$

7.2.6. MASS DETERMINATION FOR FDSC SAMPLES

For the measurements on pure aluminium, the sample mass was determined by the ratio between the melting enthalpy ΔH and the specific enthalpy of fusion Δh_{fus}:

$$\frac{\Delta H}{\Delta h_{fus}} = m \qquad (7.4)$$

The melting enthalpy is determined by integration of the uncorrected heat flow curve during melting and $\Delta h_{fus} = 397\ J\,g^{-1}$ is the specific enthalpy of fusion of aluminium [32]. The sample mass is 64 ng.

Similarly, Equation (7.4) was used to determine the AlSi12 sample mass from the integrated melting peak measured via FDSC, taking the specific enthalpy of fusion $\Delta h_{fus}^{AlSi12} = 560\ J\,g^{-1}$ [33]. For the two samples measured, the melting peak from an uncorrected heating segment at +1000 K s⁻¹ was integrated and yielded masses of 100 ng and 26 ng.

7.2.7. TEMPERATURE MODULATED DSC

Temperature Modulated DSC (TMDSC) was introduced by Reading et al in 1993 [34]. The goal was to separate "reversing" and "non-reversing" heat flow by superimposing the conventional temperature program with a periodic (sinusoidal) temperature perturbation. The technical but weak physical definition of the term "reversing heat flow" was subject to some controversy [35–37]. Despite these discussions, TMDSC was used for measurement of the heat capacity [38]. A generalized theory of

TMDSC was given 2006 [39]. It was shown that reversing heat flow is the sensible heat flow (driven by external temperature change) for quasi-static conditions. To fulfil such a condition, it was proposed to substitute the single frequency temperature modulation with a frequency spectrum by stochastic modulation [39]. Furthermore, an advanced evaluation procedure was proposed [39,40]. This modulation technique was commercialized as TOPEM by Mettler-Toledo.

The TOPEM measurements were performed in a temperature range between 25 and 550 °C with an underlying heating rate of 1 K min^{-1}. Sapphire measurements are used for calibrating the heat capacity. To avoid eventual reactions with the crucible, 30 μl alox-crucibles with lid (typical mass: 150 mg) are used. The maximum mass difference between the pans of the sample, sapphire and reference was about ±0.5 mg. The related heat capacity error was not compensated.

The modulation function was defined by the minimum and maximum switching time of 50 and 60 s and a step height of ± 1 K. The sampling distance was 0.1 s. The measurements were performed using a DSC 1 from Mettler-Toledo equipped with FRS 6 sensor. The mass of the studied AlSi12 powder sample was 27.5 mg. The high density and high thermal conductivity of metals mean masses of 30-60 mg are appropriate for decent signal strength without considerable thermal lag [41]. The following evaluation parameters are used: Evacuation Window 400s, Sample Response Parameter 2, Instrumental response parameter 60.

7.2.8. APPARENT HEAT CAPACITY

The heat flow into a sample during a DSC measurement contains two components, the sensible heat flow, ϕ_s, and the latent heat flow, ϕ_l:

$$\phi = \phi_s + \phi_l = m\, c_p\, \beta + m\, \Delta h_l\, \frac{d\xi}{dt} \qquad (7.5)$$

where Δh_l is the specific enthalpy of a latent thermal process and ξ is the internal order parameter related to the latent process. The sensible heat flow is driven by the external temperature change β and is proportional to c_p. The latent heat is driven by the change of the internal order parameter ξ and is proportional to Δh_l.

Equation (7.5) is used to define the apparent specific heat capacity that includes sensible and latent properties:

$$c_{p,a} = \frac{\phi}{m\,\beta} = c_p + \Delta h_l\, \frac{d\xi}{dT} \qquad (7.6)$$

In the case of TOPEM measurements, the sensible and latent heat flow can be assumed to be the reversing and non-reversing heat flow, respectively.

7.3. RESULTS

7.3.1. C_p DETERMINATION OF PURE ALUMINIUM

In order to develop a measurement strategy for AlSi12, preliminary investigations were performed on pure Al due to its well-known thermal properties and easy interpretation since any non-equilibrium effects are negligible within the expected resolution. Figure 7.1 shows heat flow curves during heating measured by FDSC, and the implemented temperature program The temperature program was cycled 5 times (Fig. 7.1a shows two cycles), and the measured heat flow for the slow heating segment (+1 K s^{-1}) and the faster heating segment (+5000 K s^{-1}) are displayed in (b) and (c), respectively. The plots clearly show an incremental increase in the measured heat flow with each iteration: approximately 4-5 µW at 500 °C after 5 measurement cycles. This is significantly higher than the expected drift of the sensor (<5 µW per hour according to the user manual). In addition to sensor drift, this behaviour can be caused by the change in thermal contact. For the determination of the heat capacity, the effects of these changes should be minimised. This can be done by: i) programming short isothermal segments; ii) reducing the number of superfluous measurement runs; and iii) by using the lowest maximum temperature feasible to achieve the desired results. Moreover, when the heat loss correction curve is measured as-near-as-possible to the heat scan intended for analysis, we can surmise that the impact of such gradual changes has been minimised. It is these considerations that influenced the design of the used temperature programs, as exemplified in Figure 7.1a. The slow-rate heat step (label "2") records the heat flow correction curve, after an 0.1 second isothermal step, the sample is cooled at a rate which defines the system's microstructure, and after another 0.1 s the sample is heated at the rate intended for analysis (label "6"). Cycling this time-temperature program, and implementing the slow-rate correction to the heat flow only adjacent measurement segments, provides a reliable recipe for precise heat flow measurements. By changing the implemented heating and cooling rates, the impact of such conditions on the measured heat flow may be mapped out and understood, the results of which can be seen in Figure 7.3 for that of pure aluminium, and continued in later figures to that of AlSi12. A final note on the temperature programs implemented for pure aluminium is that, aside from the initial melting-solidification programs to achieve good sample-sensor contact, the sample remained in the solid state; that is, the heat capacity measurement programs' maximum temperature was 10 degrees below the sample melting point. The pure Al melting point onset was used to correct the curves' recorded temperature.
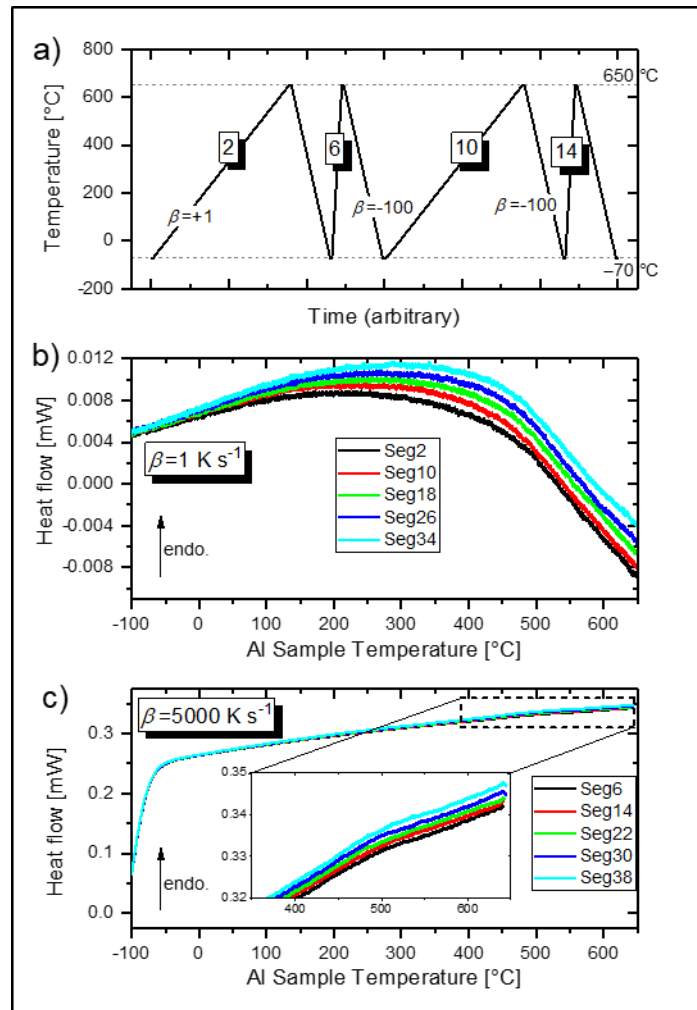
Figure 7.1: Measurements on pure Al provide justification for the structure of the implemented temperature programs. Two repeat units of the implemented temperature program are shown in a), while the heat flow measured on heating at +1 K s^{-1} and +5000 K s^{-1} are shown in b) and c). Readers should note that the absolute value of the measured heat flow changes with subsequent heat scans. As such, the slow-rate heat loss correction curve should be repeatedly re-measured for each analysed heating scan.

To further examine the influence of the heat flow drift on the heat capacity determination, heat capacity curves are determined from the data in Figure 7.1b,c in three ways and presented in Figure 7.2: a) without heat loss corrections; b) subtracting only the first +1 K s^{-1} heat loss curve; and c) always subtracting the most recent +1 K s^{-1} heat loss curve. For clarity in comparison, the 250-650 °C range is shown, while the complete curves are included Figure 7.3. With no heat flow corrections as in Fig. 7.2a, the determined heat capacity curves are not parallel to the literature values [32]. Additionally, there is a perturbation above ~500 °C which further differs the results from the literature data. Applying a correction to the heat flow by subtracting the heat flow of the initial +1 K s^{-1} segment (Fig. 7.2b) both reduces these perturbations and brings the curves parallel to the literature data. Both (a) and (b) however still exhibit the incremental changes observed in the raw data of Figure 7.1 with successive cycles. Correcting the heat flow by instead subtracting the most recent +1 K s^{-1} heat loss measurement from each +5000 K s^{-1} segment eliminates these incremental changes, with all c_p curves

lying on top of one another. The correction method of Figure 7.2c is then employed for all further c_p measurements.
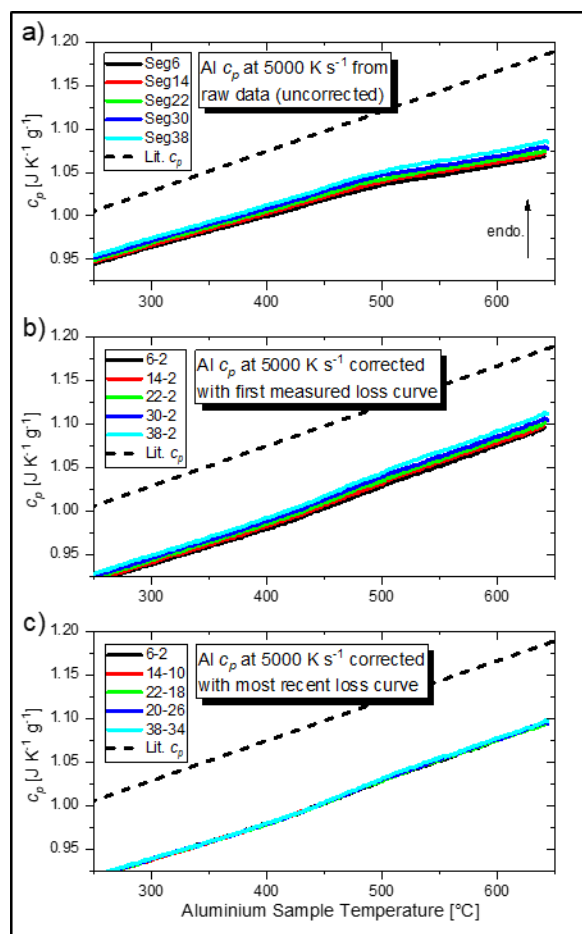

Figure 7.2: Specific heat capacity curves for pure aluminium using the data from Figure 7.1. For visual clarity, the 250-650 °C range is shown, while Figure 7.3 shows the complete corrected c_p curves. Panel (a) shows the heat capacity determined on heating at +5000 K s^{-1} with no heat flow correction, (b) shows the heat capacity determined when subtracting only the first +1 K s^{-1} segment to account for heat losses, while (c) shows the heat capacity determined when the heat flow for each +5000 K s^{-1} segment is corrected by subtracting the heat flow of the most recent +1 K s^{-1} segment.

Employing the outlined measurement strategy of slow-rate heat flow correction, the heat capacity of pure aluminium is measured on heating at rates of 1000, 5000, 10 000 and 30 000 K s^{-1}, and is presented in Figure 7.3 a, b, c and d, respectively. As expected, the noise of the heat capacity signal decreases with increasing the scanning rate due to the improved signal-to-noise ratio. Due to the thermal lag of the system the temperature at which the measuring system reaches steady state conditions increases with increasing scanning rate. The intermediate rates at +5000 and +10,000 K s^{-1} occupy a fair middle ground with excellent reproducibility, meaning the inherent noise is simple to reduce with curve averaging. Since the measured curves are all ~10 % lower than the literature values, the determined mass of 64 ng is likely ~10 % higher than the true value for this sample, though it was found to fluctuate up to 2 or 3 nanograms.
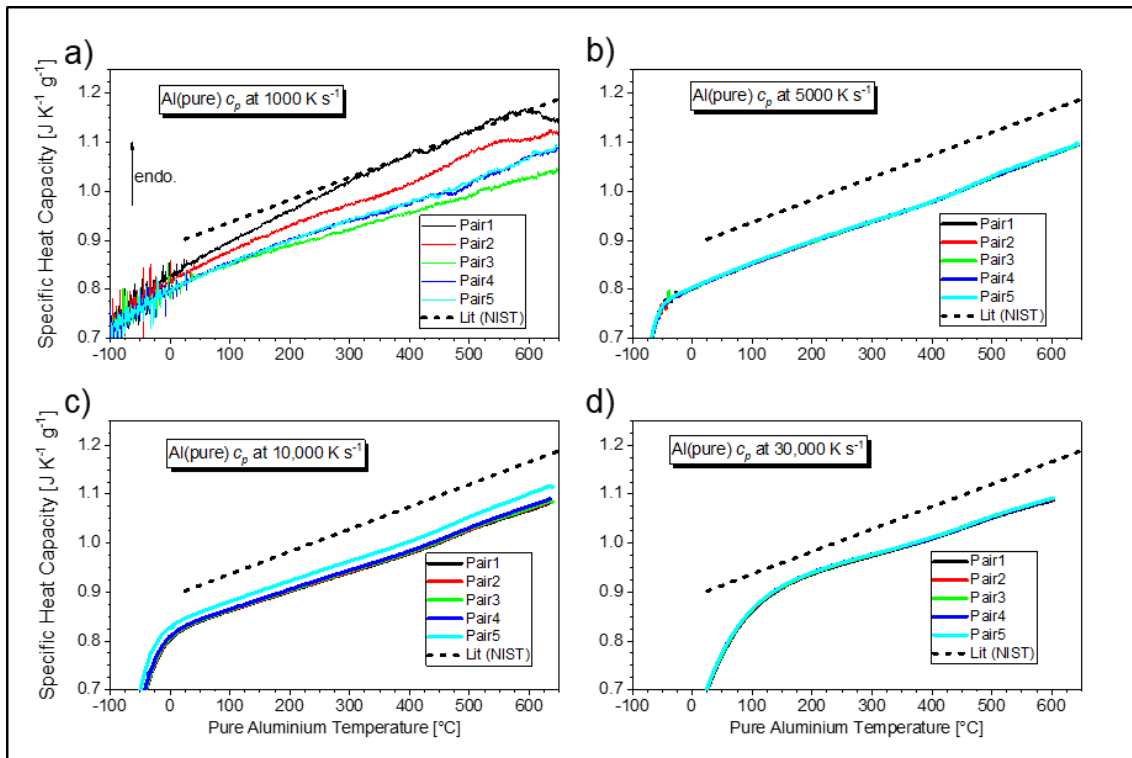
Figure 7.3: Specific heat capacity curves for pure Al determined from slow-rate corrected heat flow on heating at a) 1000 K s^{-1}; b) 5000 K s^{-1}; 10,000 K s^{-1} and d) 30,000 K s^{-1}. The mass was determined as 64 ng by integrating the sample's melting peak and curve temperature has been adjusted to match the literature melting temperature for Al [32].

7.3.2. APPLICATION TO AlSi12 POWDER FOR ADDITIVE MANUFACTURING

Figure 7.4 shows a schematic of the temperature programs implemented on the AlSi12 powder, and follows the same method as that employed for pure Al. For the measurements on AlSi12, the cooling step was implemented from the liquid state to better mimic AM processing. The relationship between the cooling rate and the alloy's microstructure can be analysed by means of the subsequent heating measurement. Quantitative heat capacity measurements here allow small differences in the microstructure to be indirectly detected. The maximum temperature was chosen as 800 °C, which ensured complete melting even at the highest heating rate (+30,000 K s^{-1}). The heating and cooling rates were chosen to evaluate their impact on apparent heat capacity from near-equilibrium to AM-relative rates (+1000 K s^{-1} to +30,000 K s^{-1} and −100 to −30,000 K s^{-1}). Thermal lag in FSC has been investigated on several metallic systems and is in the range between 0.2 ms and a few milliseconds [18, 42], with the 100 ms being more than enough time to reach thermal equilibrium.
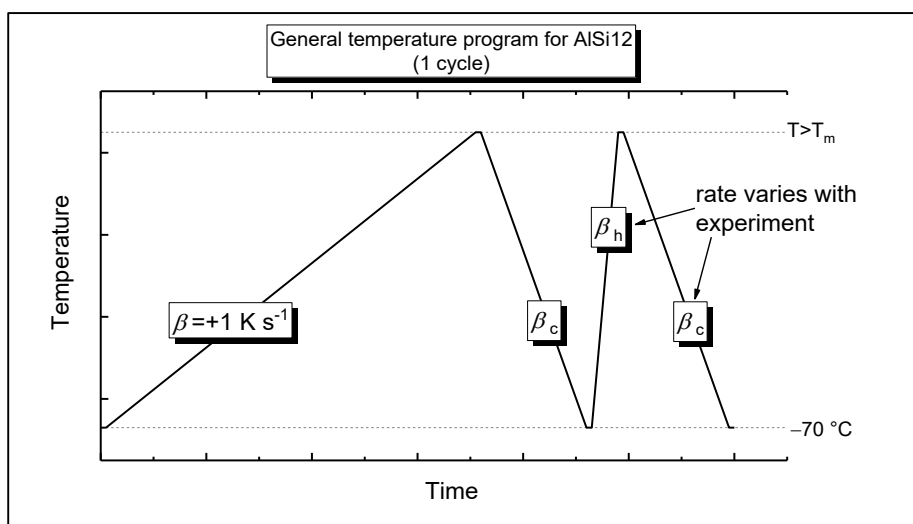
Figure 7.4: The general temperature program followed for the experiments on AlSi12. The +1 K s^{-1} heat segment is subtracted from the faster (β_h) heating segment to provide the slow-rate corrected heat flow. This figure's temperature cycle is implemented at least 2 times for each investigated rate, and the slow-rate correction as described in Section 7.3.1 is performed for each cycle. Further repetitions were implemented if inconsistencies were found in the resultant curves. The corrected heat flow curves are then averaged and divided by heating rate and sample mass to determine the heat capacity curves.

The influence of cooling and heating rate on the measured heat capacity is shown in Figure 7.5 for two sample sizes on two different sensors. Panels (a) and (c) show results on a 100 ng sample at a heating rate of 10,000 K s^{-1} after cooling at various rates and at varied heating rates after cooling at 30,000 K s^{-1}, respectively. Panels (b) and (c) show similar plots for a 26 ng sample. The evaluation procedure to produce the curves is the same as for pure aluminium. Since fairly high consistency was found in the measurements on pure Al, and to avoid unnecessary measurements which age the chip sensor, the temperature program was generally cycled twice. For measurements where less consistency was found between individual cycles, such as those involving lower heating or cooling rates, the temperature program was repeated up to 8 times, from which the curves most consistent with the rest of the data were selected for averaging. The shorthand labels used in the figure legends refer to the programmed cooling and heating rates ("β_c" and "β_h" in Figure 7.4); for example, "C1kH10k" denotes a cooling rate of −1000 K s^{-1} and a subsequent heating rate of +10,000 K s^{-1}. The slow heating step at 1 K s^{-1} is the heat loss measurement and is a permanent feature of all temperature programs.
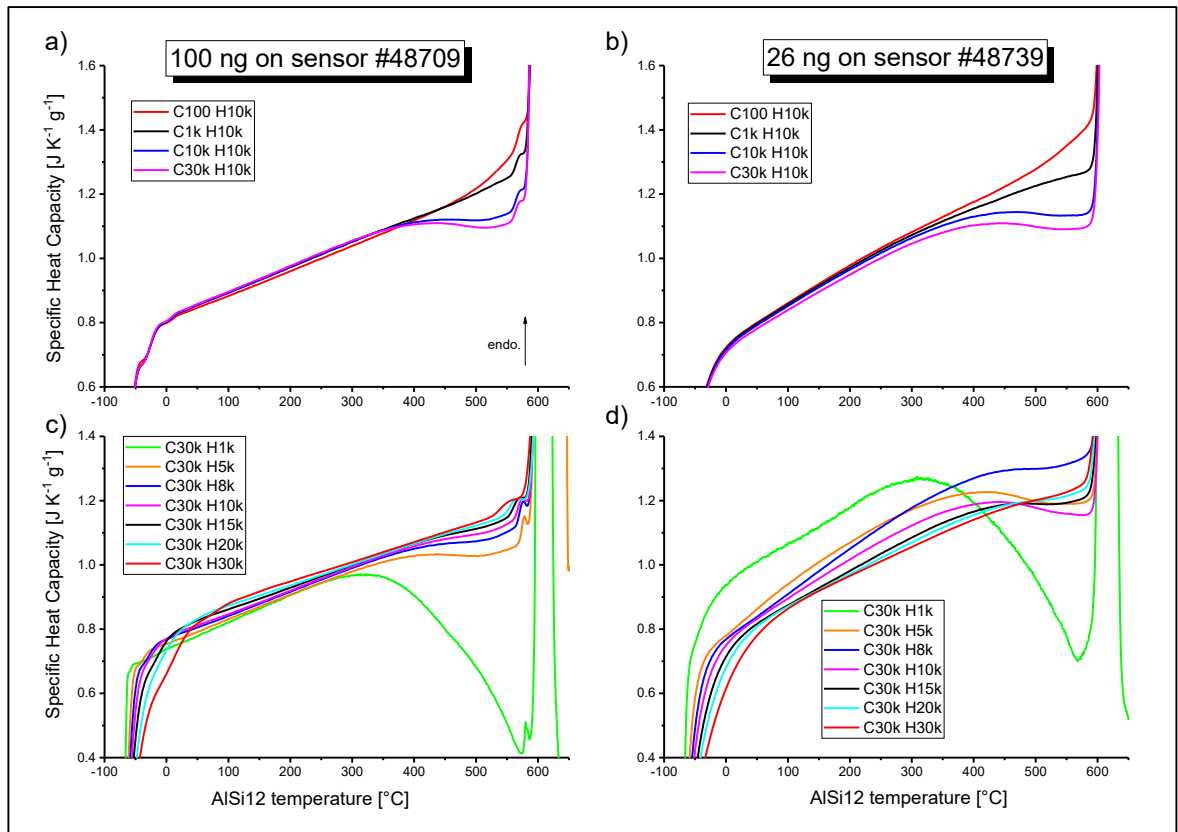
Figure 7.5: Apparent heat capacity curves on heating 2 samples of AlSi12 with various thermal histories. Panels (a) and (b) compare the measured heat capacity on heating at +10,000 K s^{-1} after different prior cooling rates for a 100 ng and 26 ng sample, respectively, while (c) and (d) compare the measured heat capacity on heating the same respective samples at various rates after a prior cooling of –30,000 K s^{-1}. The distinct drop in apparent heat capacity above ~400 °C is present only for thermal histories involving a rapid prior cooling, is reduced for faster heating rates, and is attributed to the exothermic decomposition of the super saturated solid solution produced upon rapid cooling. The 26 ng sample in (d) sees significant inconsistencies across different heating rates, though nevertheless follows the same trend of faster heating rates corresponding to a smaller apparent c_p drop. The upward inflection of the C100H10k curves (red) before the onset of melting may be due to the dissolution of silicon that precipitated during the –100 K s^{-1} cooling step, prior.

An obvious feature of the curves in Figure 7.5 is the depression in apparent heat capacity above ~400 °C. As expected, the 100 ng sample shows better consistency than the 26 ng sample. Importantly in (d), although not immediately clear from the plot, the same trend in apparent heat capacity depression is found as that seen in (c). The gradient variations seen in (c) and (d) both follow a trend of increasing gradient with slower heating rate. Beyond this, slower heating rates also have slightly higher melting onset temperatures. Finally, panels (a) and (b) see a slight upward inflection shortly before melting for curves measured after the slowest cooling rate (C100 H10k, red).

Finally, to provide some context and evaluate the accuracy and reliability of the collected FDSC data, Figure 7.6 compares heat capacity curves from TOPEM measurements and a FactSage calculation for AlSi12 to the FDSC results. The "C100 H10k" curve of the 100 ng sample is included for comparison and is the FDSC measurement examined involving minimal Si precipitation. It correlates well to the simulated and TOPEM heat capacity curves. The TOPEM curve of the AlSi12 AM powder is a fair

match at lower temperature, but shows a feature at 400-500 °C, possibly an indirect effect of the dissolution and precipitation occurring at that time.
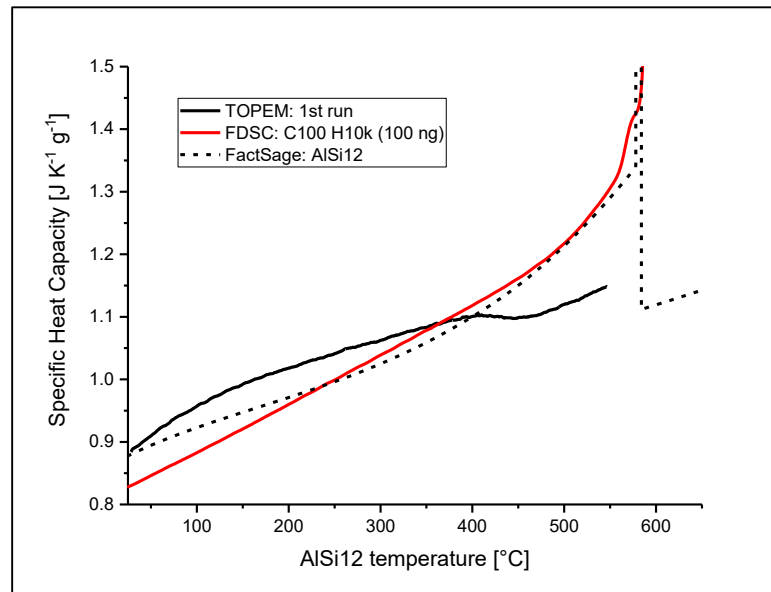

Figure 7.6: Heat capacity values are shown in context by comparing results from TOPEM and FDSC measurements of the AlSi12 powder to a FactSage calculation. The FactSage simulation well reflects the FDSC curve C100 H10k performed on the 100 ng sample.

7.4. DISCUSSION

The experimental approach first developed by examining high purity aluminium is found to yield highly reproducible results over a wide span of scanning rates. This approach is then utilised for experiments on eutectic AlSi commonly used in additive manufacturing. Collecting precise data under non-equilibrium conditions is greatly relevant to AM, and the presented results on eutectic AlSi already reveal useful information that could directly impact AM process parameters, or be fed into simulation calculations. Similar experiments for other materials could be easily derived from this same approach, and promise a wealth of information on non-equilibrium material states and rapid-rate processes.

7.4.1. C_P DETERMINATION STRATEGY

The results on pure Al presented in Figure 7.1b and c, which depict a gradual drift to more endothermic heat flow values, tangibly demonstrate how such systematic errors generate an additional uncertainty in heat capacity. This phenomenon is noticeable for the high temperature UFH 1 sensors, and was not obvious with low temperature UFS 1 sensors [9]. Since the melting enthalpy, sample colour and geometry do not change significantly during the experiments, the sample is not altered by oxidation. Other possible effects could involve reaction between sensor and sample, or changing sensor properties. The error of the heat capacity can be reduced by an improvement to experimental design as shown in Figure 7.1a and Figure 7.4. The principle of the improved determination method is to minimize the time between the segments which measure the heat loss and the sample heat flow. This

minimises the impact of the observed incremental changes in absolute heat flow. The cycle's cooling segments and fast-heating segments can then be adjusted to suit individual measurement needs, an approach which is followed in Figure 7.4 for the subsequent measurements on AlSi12. Performing the slow-rate heat flow correction on individual pairs, that is, correcting measured heat flow by subtracting the preceding +1 K s^{-1} heating scan from each fast-heating scan, should then yield more consistent results across multiple measurement cycles.

Further support for this measurement procedure is provided by Figure 7.2, where the pair-wise heat flow correction (Fig. 7.2c) is shown to yield the best consistency.

The corrected heat capacity curves for pure Al collected in Figure 7.3 cover the scanning rate range commonly utilised in FDSC scans, and therefore provide some insight into optimal measurement conditions. The inconsistencies found in the +1000 K s^{-1} curves may be due to changes in the sample surface, the sample-membrane interface, or some early-stage fatigue of the chip's sensors. Early-stage aging of the sensor is certainly a possibility, crucially because those curves in Figure 7.3a were measured before the other studied rates, and because the curves of Figure 6.3a tend to approach those values of Figure 7.3b,c,d with each successive cycle. This happens despite the execution of the standard sensor conditioning and the melting-solidification programs. This last observation is of crucial importance, since it implies the sample-sensor system does not reach a steady state after the initial melting cycles, but only after a few low-rate heating scans. Since this effect can impact the first few measurements on a sensor, it is worth considering in experimental design.

Since the determined c_p curves are all ~10 % lower than the literature values, the 64 ng mass determined from the pure Al sample's melting peak is suspected to be ~10 % higher than the true sample mass. Other than this apparent systematic error, the curves are highly consistent and parallel to the expected values, as such, similar heat capacity measurements could be a useful tool for assessing the accuracy of the FDSC determined mass. A similar issue of apparent mass inaccuracy was also found for pure Pb with UFS1 chip sensors [9]. Although in that case the c_p was always overestimated (meaning calculated mass was too low) rather than underestimated as in the present case for Al on the UFH1 chip sensors. In both cases, the results benefit from knowing the material's equilibrium heat capacity; however, precise mass estimation remains a source of probable inaccuracy for c_p calculation in FDSC experiments [8].

In any case, the results presented in Figure 7.3 represent a successful adaptation of the experimental design of [9] to the specific requirements of UFH 1 chip sensors; after some initial changes in the measurement values, the results converge upon the literature heat capacity and exhibit excellent reproducibility, establishing this pair-wise heat flow correction as a sound method.

7.4.2. APPLICATION TO ALSI12 AM POWDER

The developed method for heat capacity determination is generalised schematically in Figure 7.4. This experimental approach is followed for the heat capacity measurements presented in Figures 7.3 and 7.5, and may also serve as a template for precise heat flow measurements by FDSC on other materials.

The cooling rates for the experiments on AlSi12 were chosen in the range from near-equilibrium to strong, non-equilibrium conditions. Tuning the maximum and minimum temperatures, as well as the programmed fast heating and cooling rates (β_h and β_c in Fig. 7.4), to suit the individual needs of the material is a valid approach for precise heat flow measurements in general, provided the system in question is suited to cyclic analysis via the slow-rate heat flow correction method. That is, providing the sample properties of interest are not irreversibly changed during the slow heating segment. In general, metallic systems are well suited to this approach, since the system properties investigated can be consistently reproduced by cooling from the molten state. Taking a similar approach on other alloy systems promises a wealth of useful data.

Regarding the present results on AlSi12, Figure 7.5 shows a clear heat capacity depression above ~400 °C dependent on the chosen heating and cooling rates. The measured apparent heat capacity curves displayed in Figure 7.5 are the sum of i) the sensible specific heat capacity and ii) the latent specific heat capacity due to any thermal effect occurring during heating. The curves in Figure 7.5 therefore show that a significant exothermic event occurs on heating above ~400 °C. This event increases with a more rapid previous cooling rate. Assuming that faster cooling produces a stronger supersaturation, which has higher propensity for precipitation, points to precipitation causing the release of heat and the depression in determined apparent heat capacity. This is corroborated in the literature, where Si precipitation is reported at temperatures as low as 135 °C for a similarly composed AlSi alloy [41], while many other studies into Al-Si systems show Si precipitation as a surety when reheating rapidly cooled material [25,42].

Looking then at panels (c) and (d) with constant −30,000 K s^{-1} prior cooling show the curves measured at lower heating rates have a larger precipitation event. This aligns with expectations, since during slow heating the sample spends more time at precipitation-possible temperatures before melting at ~585 °C. This melting temperature is slightly higher than the reported eutectic temperature of 577 °C [43], likely a result of some device temperature inaccuracy. For the slowest prior cooling rate, an upward inflection is seen prior to melting. This could be associated with the endothermic equilibrium dissolution of Si, known from the solubility of Si in Al [43], and also seen in the calculated apparent c_p curve from FactSage in Figure 6.6. Additionally, the impact of heating rate on melting temperature, though minor, is possibly a consequence of grain growth/coarsening during heating, since smaller grains cause lower melting temperatures, and vice versa, larger grains comparatively higher melting temperatures [44,45]. Much of the success of AlSi12 and AlSi10Mg for LPBF is attributed to the presence of silicon [27], since it is largely responsible for heat absorption from the scanning laser [46], and also because of its impact on solidification by helping to reduce solidification cracking. Cracking during solidification is related to the solidification range of the alloy, the undercooling [20], the fluidity of the molten phase, the solidification shrinkage and the coefficient of thermal expansion; parameters which are all improved by a near-eutectic silicon content [27]. A deepened understanding of phase content during rapid processing is therefore highly relevant to AM.

The comparison of TOPEM, FDSC and simulated heat capacity curves in Figure 7.6 shows decent consistency across the three methods and establishes good confidence in the accuracy of the FDSC results. The "C100 H10k" measurement is chosen for comparison here since it involves little precipitation. The c_p depression seen in the TOPEM result occurs at the same temperature precipitation is found in the FDSC data, suggesting the precipitation and dissolution there as at least an indirect cause. Equilibrium c_p measurements of the as-produced AM powder, which is far from equilibrium, may not be the most optimal approach, even using temperature modulation. Tuning of parameters such as temperature amplitude could provide some benefit in this regard, but are outside of the scope of this work.

A broad assessment of the collected measurements on all three sensors also reveals some basic information regarding optimal measurement parameters. For the measurement of Al-based materials the optimum sample size for the UFH 1 sensor seems to be between 50 ng and perhaps a few hundred nanograms. This is supported by the present results since the lowest mass of 26 ng showed some inconsistency, particularly at heating rates below +10,000 K s^{-1} (see Fig. 6.5d); although the specific cause of this is not certain, the low mass seems likely. The 100 ng and 67 ng samples both performed well, with the exception of some noise on heating at +1000 K s^{-1} (see Fig 7.3a). Measurements at higher rates benefit from a better signal to noise ratio, with the noise at +5000 to +30,000 K s^{-1} having little impact on the determined curves, though the thermal lag at the highest rates can impact the range of usable results. Since high consistency was generally found for the studied samples, 2 to 6 measurements were sufficient for averaging. These general observations could serve to inform future experiments on UFH 1 sensors, particularly for metallic materials.

While the phenomena of Si precipitation in quenched Al-Si alloys is certainly nothing new, its impact on apparent heat capacity at such high heating rates, as found in LPBF, is very valuable data. Contemporary modelling and simulation studies in AM often rely on fixed or equilibrium values of heat capacity [47–50], and could certainly benefit from improved data here. Depending on the actual thermal history, apparent heat capacity could be only 35 % of the equilibrium value (Fig. 7.5). Moreover, the precipitation observed in the heat capacity data could have direct implications on the process parameters for AM and on the understanding of how microstructure and phase composition evolve during printing. The work of Yang et al. on the microstructure of single AlSi12 powder particles dependent on particle size and undercooling is also highly relevant here [21]. The precipitation revealed in Figure 7.5 goes some way to understanding how post-solidification heat spikes might impact the evolving microstructure, and how absorptivity and heat transfer might evolve during the process; considerations which dictate the optimal process parameters like laser power, scan speed and hash spacing.

7.5. CONCLUSION

Using high purity aluminium as a standard for assessing accuracy and precision, a measurement strategy based on a slow-rate heat flow correction is developed and refined for specific heat capacity measurements in fast differential scanning calorimetry using MultiStar UFH 1 chip sensors. This

strategy is then applied to the study of the aluminium alloy AlSi12, with the aim of further understanding the kinetic impacts and microstructural changes caused by high heating and cooling rates, and the results are discussed in the context of metal additive manufacturing. FactSage thermodynamic simulations and temperature-modulated DSC measurements contextualise the FDSC results on AlSi12. Differences in the measured apparent heat capacity reveal strong decomposition effects of super saturated solid solution, which are highly relevant to processing and for understanding the microstructure and phase content evolution during additive manufacturing methods such as laser powder bed fusion. The measurement method herein developed provides a reliable method for precision heat flow measurements involving rapid heating and cooling via FDSC, and can be easily adapted to suit many materials; especially metals and metal alloys used for additive manufacturing.

7.6. REFERENCES

[1]   Pijpers TFJ, Mathot VBF, Goderis B, Scherrenberg RL, van der Vegte EW. High-Speed Calorimetry for the Study of the Kinetics of (De)vitrification, Crystallization, and Melting of Macromolecules †. Macromolecules. 2002;35:3601–13. doi:10.1021/ma011122u.

[2]   Schawe JE. An analysis of the meta stable structure of poly(ethylene terephthalate) by conventional DSC. Thermochimica Acta. 2007;461:145–52. doi:10.1016/j.tca.2007.05.017.

[3]   Zhuravlev E, Schick C. Fast scanning power compensated differential scanning nano-calorimeter: 1. The device. Thermochimica Acta. 2010;505:1–13. doi:10.1016/j.tca.2010.03.019.

[4]   Mathot V, Pyda M, Pijpers T, Vanden Poel G, van de Kerkhof E, van Herwaarden S, et al. The Flash DSC 1, a power compensation twin-type, chip-based fast scanning calorimeter (FSC): First findings on polymers. Thermochimica Acta. 2011;522:36–45. doi:10.1016/j.tca.2011.02.031.

[5]   Schawe JEK. Influence of processing conditions on polymer crystallization measured by fast scanning DSC. J Therm Anal Calorim. 2014;116:1165–73. doi:10.1007/s10973-013-3563-8.

[6]   Cebe P, Partlow BP, Kaplan DL, Wurm A, Zhuravlev E, Schick C. Using flash DSC for determining the liquid state heat capacity of silk fibroin. Thermochimica Acta. 2015;615:8–14. doi:10.1016/j.tca.2015.07.009.

[7]   Cebe P, Hu X, Kaplan DL, Zhuravlev E, Wurm A, Arbeiter D, Schick C. Beating the heat--fast scanning melts silk beta sheet crystals. Sci Rep. 2013;3:1130. doi:10.1038/srep01130.

[8]   Zhuravlev E, Schick C. Fast scanning power compensated differential scanning nano-calorimeter:: 2. Heat capacity analysis. Thermochimica Acta. 2010;505:14–21. doi:10.1016/j.tca.2010.03.020.

[9]   Quick CR, Schawe J, Uggowitzer PJ, Pogatscher S. Measurement of specific heat capacity via fast scanning calorimetry—Accuracy and loss corrections. Thermochimica Acta. 2019;677:12–20. doi:10.1016/j.tca.2019.03.021.

[10]   Schick C, Mathot V. Fast Scanning Calorimetry. Cham: Springer International Publishing; 2016.

[11]   Adamovsky S, Minakov A, Schick C. Scanning microcalorimetry at high cooling rate. Thermochimica Acta. 2003;403:55–63. doi:10.1016/S0040-6031(03)00182-5.

[12]   Abdelaziz A, Zaitsau DH, Mukhametzyanov TA, Solomonov BN, Cebe P, Verevkin SP, Schick C. Melting temperature and heat of fusion of cytosine revealed from fast scanning calorimetry. Thermochimica Acta. 2017;657:47–55. doi:10.1016/j.tca.2017.09.013.

[13] Lai SL, Ramanath G, Allen LH, Infante P, Ma Z. High-speed (10 4 °C/s) scanning microcalorimetry with monolayer sensitivity (J/m 2). Appl. Phys. Lett. 1995;67:1229–31. doi:10.1063/1.115016.

[14] Kolesov I, Mileva D, Androsch R, Schick C. Structure formation of polyamide 6 from the glassy state by fast scanning chip calorimetry. Polymer. 2011;52:5156–65. doi:10.1016/j.polymer.2011.09.007.

[15] Spieckermann F, Steffny I, Bian X, Ketov S, Stoica M, Eckert J. Fast and direct determination of fragility in metallic glasses using chip calorimetry. Heliyon. 2019;5:e01334. doi:10.1016/j.heliyon.2019.e01334.

[16] Neuber N, Frey M, Gross O, Baller J, Gallino I, Busch R. Ultrafast scanning calorimetry of newly developed Au-Ga bulk metallic glasses. J Phys Condens Matter. 2020;32:324001. doi:10.1088/1361-648X/ab8252.

[17] Orava J, Greer AL, Gholipour B, Hewak DW, Smith CE. Characterization of supercooled liquid Ge2Sb2Te5 and its crystallization by ultrafast-heating calorimetry. Nature Mater. 2012;11:279–83. doi:10.1038/nmat3275.

[18] Pogatscher S, Uggowitzer PJ, Löffler JF. In-situ probing of metallic glass formation and crystallization upon heating and cooling via fast differential scanning calorimetry. Appl. Phys. Lett. 2014;104:251908. doi:10.1063/1.4884940.

[19] Yang B, Malz S, Zhuravlev E, Milkereit B, Schick C, Kessler O. Differential Fast Scanning Calorimetry as analytical tool for mimicking melting and solidification in additive manufacturing. Additive Manufacturing Meets Medicine 2019. doi:10.18416/AMMM.2019.1909S03P23.

[20] Zhuravlev E, Milkereit B, Yang B, Heiland S, Vieth P, Voigt M, et al. Assessment of AlZnMgCu alloy powder modification for crack-free laser powder bed fusion by differential fast scanning calorimetry. Materials & Design. 2021;204:109677. doi:10.1016/j.matdes.2021.109677.

[21] Yang B, Peng Q, Milkereit B, Springer A, Liu D, Rettenmayr M, et al. Nucleation behaviour and microstructure of single Al-Si12 powder particles rapidly solidified in a fast scanning calorimeter. J Mater Sci. 2021;56:12881–97. doi:10.1007/s10853-021-06096-6.

[22] Yang B, Abyzov AS, Zhuravlev E, Gao Y, Schmelzer, J. W. P., Schick C. Size and rate dependence of crystal nucleation in single tin drops by fast scanning calorimetry. The Journal of Chemical Physics. 2013;138:54501. doi:10.1063/1.4789447.

[23] Yang B, Gao Y, Zou C, Zhai Q, Abyzov AS, Zhuravlev E, et al. Cooling rate dependence of undercooling of pure Sn single drop by fast scanning calorimetry. Appl. Phys. A. 2011;104:189–96. doi:10.1007/s00339-010-6100-7.

[24] Pauly S, Wang P, Kühn U, Kosiba K. Experimental determination of cooling rates in selectively laser-melted eutectic Al-33Cu. Additive Manufacturing. 2018;22:753–7. doi:10.1016/j.addma.2018.05.034.

[25] Prashanth KG, Scudino S, Klauss HJ, Surreddi KB, Löber L, Wang Z, et al. Microstructure and mechanical properties of Al–12Si produced by selective laser melting: Effect of heat treatment. Materials Science and Engineering: A. 2014;590:153–60. doi:10.1016/j.msea.2013.10.023.

[26] Ponnusamy P, Rahman Rashid RA, Masood SH, Ruan D, Palanisamy S. Mechanical Properties of SLM-Printed Aluminium Alloys: A Review. Materials 2020. doi:10.3390/ma13194301.

[27] Aversa A, Marchese G, Saboori A, Bassini E, Manfredi D, Biamino S, et al. New Aluminum Alloys Specifically Designed for Laser Powder Bed Fusion: A Review. Materials 2019. doi:10.3390/ma12071007.

[28] Kempen K, Thijs L, van Humbeeck J, Kruth J-P. Processing AlSi10Mg by selective laser melting: parameter optimisation and material characterisation. Materials Science and Technology. 2015;31:917–23. doi:10.1179/1743284714Y.0000000702.

[29] Bale CW, Chartrand P, Degterov SA, Eriksson G, Hack K, Ben Mahfoud R, et al. FactSage thermochemical software and databases. Calphad. 2002;26:189–228. doi:10.1016/S0364-5916(02)00035-4.

[30] FTlite - the FACT Light Metal Alloy Database. www.factsage.com/facthelp/FSNew_Databases.htm#FTlite. Accessed 2 Dec 2020.

[31] Schawe JE, Hess K-U. The kinetics of the glass transition of silicate glass measured by fast scanning calorimetry. Thermochimica Acta. 2019;677:85–90. doi:10.1016/j.tca.2019.01.001.

[32] Valencia JJ, Quested PN. Thermophysical Properties. ASM Handbook. 2008;15: Casting:468–81. doi:10.1361/asmhba0005240.

[33] Wang X, Liu J, Zhang Y, Di H, Jiang Y. Experimental research on a kind of novel high temperature phase change storage heater. Energy Conversion and Management. 2006;47:2211–22. doi:10.1016/j.enconman.2005.12.004.

[34] Reading M, Elliott D, Hill VL. A new approach to the calorimetric investigation of physical and chemical transitions. Journal of Thermal Analysis. 1993;40:949–55. doi:10.1007/BF02546854.

[35] Schawe J. Principles for the interpretation of modulated temperature DSC measurements. Part 1. Glass transition. Thermochimica Acta. 1995;261:183–94. doi:10.1016/0040-6031(95)02315-S.

[36] Schawe J. A comparison of different evaluation methods in modulated temperature DSC. Thermochimica Acta. 1995;260:1–16. doi:10.1016/0040-6031(95)90466-2.

[37] Lacey AA, Nikolopoulos C, Reading M. A mathematical model for Modulated Differential Scanning Calorimetry. Journal of Thermal Analysis. 1997;50:279–333. doi:10.1007/BF01979568.

[38] Wunderlich B, Boller A, Okazaki I, Ishikiriyama K. Heat-capacity determination by temperature-modulated DSC and its separation from transition effects. Thermochimica Acta. 1997;304-305:125–36. doi:10.1016/S0040-6031(97)00184-6.

[39] Schawe J, Hütter T, Heitz C, Alig I, Lellinger D. Stochastic temperature modulation: A new technique in temperature-modulated DSC. Thermochimica Acta. 2006;446:147–55. doi:10.1016/j.tca.2006.01.031.

[40] Schubnell M, Heitz C, Hütter T, Sauerbrunn S, Schawe J.E.K. A multifrequency temperature-modulated technique for DSC. American Laboratory. 2006;38:18–26.

[41] Carlton G. Slough, Nathan D. Hesse. High Precision Heat Capacity Measurements of Metals by Modulated DSC. 2006. https://www.tainstruments.com/pdf/literature/ta339%20high%20precision%20cp%20measurements%20of%20metals%20by%20mdsc.pdf. Accessed 6 Oct 2022.

[42] Schawe JE. Temperature correction at high heating rates for conventional and fast differential scanning calorimetry. Thermochimica Acta. 2021;698:178879. doi:10.1016/j.tca.2021.178879.

[43] van Rooyen M, Mittemeijer EJ. Precipitation of silicon in aluminum-silicon: A calorimetric analysis of liquid-quenched and solid-quenched alloys. Metallurgical Transactions A. 1989;20:1207–14.

[44] Lasagni F, Mingler B, Dumont M, Degischer HP. Precipitation kinetics of Si in aluminium alloys. Materials Science and Engineering: A. 2008;480:383–91. doi:10.1016/j.msea.2007.07.008.

[45] Mondolfo LF. Aluminum Alloys: Structure and Properties. Burlington: Elsevier Science; 2013.

[46] Schlexer P, Andersen AB, Sebok B, Chorkendorff I, Schiøtz J, Hansen TW. Size-Dependence of the Melting Temperature of Individual Au Nanoparticles. Part. Part. Syst. Charact. 2019;36:1800480. doi:10.1002/ppsc.201800480.

[47] Sheng HW, Lu K, Ma E. Melting and freezing behavior of embedded nanoparticles in ball-milled Al–10wt% M (M=In, Sn, Bi, Cd, Pb) mixtures. Acta Materialia. 1998;46:5195–205. doi:10.1016/S1359-6454(98)00108-6.

[48] Sercombe TB, Li X. Selective laser melting of aluminium and aluminium metal matrix composites: review. Materials Technology. 2015:1–9. doi:10.1179/1753555715Y.0000000078.

[49] Panwisawas C, Qiu C, Anderson MJ, Sovani Y, Turner RP, Attallah MM, et al. Mesoscale modelling of selective laser melting: Thermal fluid dynamics and microstructural evolution. Computational Materials Science. 2017;126:479–90. doi:10.1016/j.commatsci.2016.10.011.

[50] Beal VE, Erasenthiran P, Ahrens CH, Dickens P. Evaluating the use of functionally graded materials inserts produced by selective laser melting on the injection moulding of plastics parts. Proceedings of the Institution of Mechanical Engineers, Part B: Journal of Engineering Manufacture. 2007;221:945–54. doi:10.1243/09544054JEM764.

[51] Loh L-E, Chua C-K, Yeong W-Y, Song J, Mapar M, Sing S-L, et al. Numerical investigation and an effective modelling on the Selective Laser Melting (SLM) process with aluminium alloy 6061. International Journal of Heat and Mass Transfer. 2015;80:288–300. doi:10.1016/j.ijheatmasstransfer.2014.09.014.

[52] Mirkoohi E, Seivers DE, Garmestani H, Liang SY. Heat Source Modeling in Selective Laser Melting. Materials 2019. doi:10.3390/ma12132052.

8. Metallic Sample Preparation for in-situ Heating Experiments in a TEM

The use of microelectromechanical systems (MEMS) within electron-microscopes is at the forefront of experimental materials science, allowing in situ experiments to be performed for a wide variety of applications. Sample preparation for transmission electron microscopy (TEM) often involves the use of focused ion beam (FIB) systems which may impact the final quality of the specimens in several different ways (e.g. Ga implantation leading to contamination). The present manuscript presents a unique, fast, reliable and implantation-free sample preparation methodology for ~50 μm electron-transparent metallic samples. The developed methodology is assessed with cutting-edge energy dispersive X-ray spectroscopy (EDX) and with a real-time in situ S/TEM heat treatment experiment of an innovative aluminium alloy. The experimental approach is of significance for a broad audience of scientists interested in microscopic aspects of phase transformations in materials and for the development of improved alloys.

A Fast and Implantation-Free Sample Production Method for Large Scale Electron Transparent Metallic Samples Destined for MEMS-based In-situ Experiments*

Microelectromechanical systems (MEMS) are currently supporting ground-breaking basic re-search in materials science and metallurgy as they allow in situ experiments on materials at the nanoscale within electron microscopes in a wide variety of different conditions such as extreme materials dynamics under ultrafast heating and quenching rates as well as in complex electrochemical environments. Electron-transparent sample preparation for MEMS e-chips remains a challenge for this technology as the existing methodologies can introduce contaminants, thus disrupting the experiments and the analysis of results. Herein we introduce a methodology for simple and fast electron-transparent sample preparation for MEMS e-chips without significant contamination. The quality of the samples as well as their performance during a MEMS e-chip experiment in situ within an electron microscope are evaluated during a heat treatment of a crossover AlMgZn(Cu) alloy.

8.1. INTRODUCTION

The use of microelectromechanical systems (MEMS) within scanning/transmission electron microscopes (S/TEM) is at the forefront of experimental science, particularly in the fields of nanotechnology and materials science. As a rapidly evolving and emerging technology, MEMS experiments with in situ TEM can provide countless opportunities for investigation of the real-time response of materials in corrosive and gaseous environments [1,2], under extreme dynamic changes when subjected to ultrafast heating and cooling rates of up to 10^6 K·s^{-1} [3,4], under mechanical loading [5,6] or when subjected to complex photocatalytic environments [7,8]. These experiments are now in fact contributing to the design of new materials at the nanoscale as well as supporting the progress of basic re-search in science by allowing complex physicochemical [9] and/or elastoplastic [10] mechanisms to be fundamentally investigated at the nanoscale.

A major challenge when carrying out MEMS experiments with in situ TEM lies in the sample preparation methodology chosen for producing good-quality, electron-transparent lamellae and their subsequent transfer to the MEMS e-chips. Up to now, such sample preparation methodology has been highly dependent on the application of dual-beam scanning electron microscopes (SEM) with focused ion beam (FIB) capabilities [4,11,12].

Unquestionable reliability and efficiency are evident characteristics of FIB-based methods for producing electron-transparent samples from metallic substrates [13], but several degradation mechanisms are reported to occur during the stages' sample preparation within SEM-FIBs [14]. These may impact the final quality of a specimen and possibly affect the reliability of the results generated

during MEMS experiments within a S/TEM. Many metallurgical samples, such as those made from Al-based alloys, may strongly interact with either Ga ions [15] or Pt/C layers often used as a top-protective coatings [14,16], resulting in contamination and subsequent formation of undesirable artefacts. The advent of plasma-based FIBs (using Xe ions) is reported to mitigate some deleterious effects found in Ga-based FIBs [15], but the use of Xe ions can impact electron-transparent metallic la-mellae in different ways including radiation-induced damage or even the formation of nanometer-sized Xe bubbles [17].

Given the facts, the optimal scenario would be an electron-transparent sample preparation methodology free of both implantation from ballistic cascades (Ga, Xe) and contamination from welding (Pt). We report in this paper an alternative methodology for producing good-quality and implantation-free electron-transparent metallic specimens for MEMS experiments with in situ S/TEM, consisting, in essence, of a series of scalpel cuts on an electropolished 3 mm disk to isolate a suitably sized sample. Following a detailed description of the MEMS electron-transparent sample preparation methodology, a heat treatment experiment in situ within a S/TEM is presented using a MEMS chip and the quality of the produced specimen before and after the experiment is evaluated using conventional and analytical electron-microscopy techniques.

8.2. Materials and Methods

8.2.1. Provenance of the metallic Samples

The MEMS sample preparation methodology reported in this research works for a wide variety of metallic samples. As a demonstrative example, the experiments reported in this present paper use a novel crossover $AlMg_{4.7}Zn_{3.6}Cu_{0.6}$ alloy (in wt.%). Throughout the text, these samples will be referred to as "AlMgZn(Cu) alloy". The alloy was pre-aged for 3 h at 373 K and subjected to a minor deformation level of 2% (for details on the synthesis, processing and materials properties we refer to [18]).

8.2.2. Jet Electropolishing (JEP)

Electron-transparent specimens of the AlMgZn(Cu) alloy were prepared using the technique of jet electropolishing. The samples were polished and ground to 100 μm of thickness and mechanically punched out to 3 mm disks. For the JEP procedure, an electrolyte solution composed of 25% nitric acid and 75% methanol (in vol.%) was used at a temperature range of 253–257 K with the electrode potential set to 12 V. During JEP, the specimen current slightly oscillated around 90 mA. After JEP, the samples were washed in three different pure methanol baths and left to dry in air.

8.2.3. Scanning/Transmission Electron Microscopy (S/TEM)

Electron microscopy was carried out using a Thermo Fisher Scientific™ Talos F200X scanning/transmission electron microscope (ThermoFisher Scientific, Hillsboro, OR, USA). The microscope operates a X-FEG filament (a refinement of the Schottky thermally assisted field emission gun) at 200 kV and features the Super-X energy dispersive X-ray (EDX) spectroscopy technology. For

the investigations reported in this paper, the following imaging modes were used: bright-field TEM (BF-TEM), selected-area electron diffraction (SAED), low-angle annular dark-field (LAADF) and bright-field STEM (BF-STEM).

8.2.4. MEMS Experiments with In Situ S/TEM

In situ S/TEM heat treatment experiments were performed using a Protochips FUSION 200 MEMS chip-based holder (Protochips, Morrisville, NC, USA). with double-tilt capability. For the heat treatment experiments reported in this work, the AlMgZn(Cu) alloy was subjected to a heating ramp of +60 K·min^{-1} up to 458 K where the samples were held for 1200 s. Then, a cooling ramp of -60 K·min^{-1} was applied down to a temperature of 298 K. This heat treatment specification is denoted in the metallurgical literature as a paint bake [18]. For the MEMS experiments reported in this work, e-chips without coating on the SiN membrane (a hollow region with 9 holes where the electron-transparent piece was placed to be analysed within the S/TEM) were used.

8.3. Results and Discussion

8.3.1. MEMS Sample Preparation Methodology

The MEMS sample preparation methodology investigated in this work is described in the set of optical micrographs in Figure 8.1a–i. The entire process can be performed using a simple stereo microscope with magnification in the order of 100–200×.
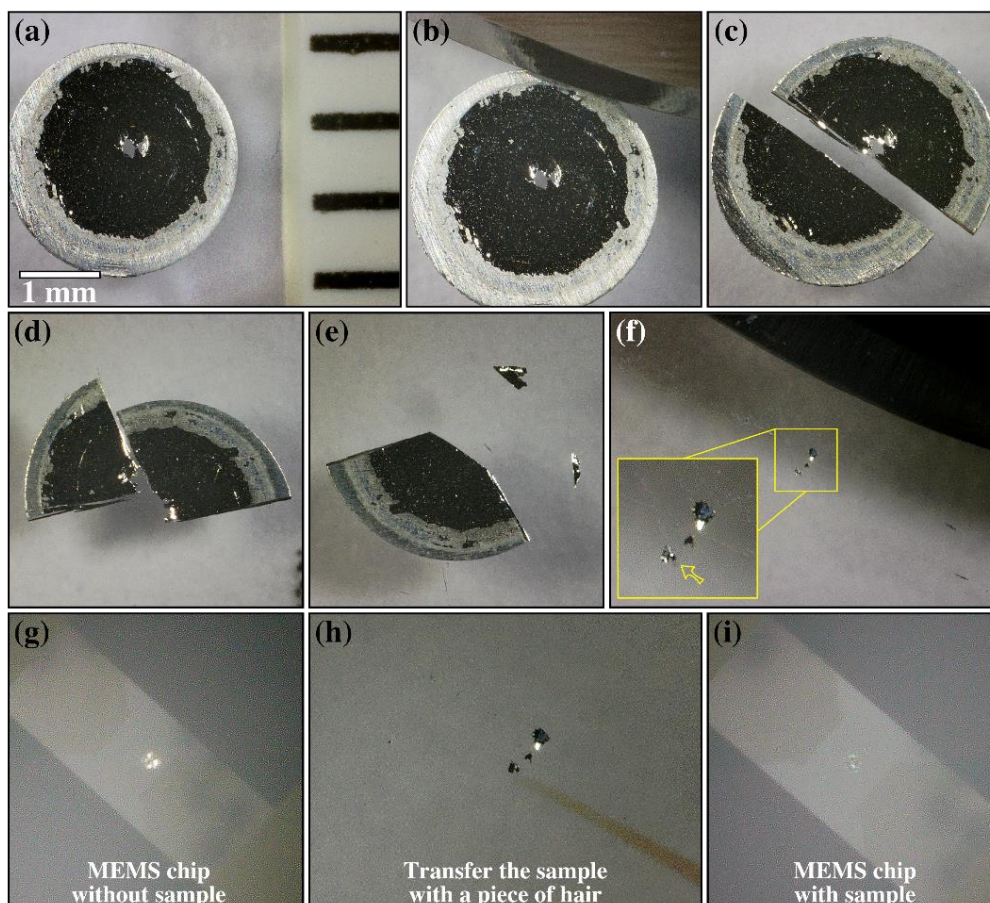
Figure 8.1: Step-by-step description of the sample preparation methodology proposed in this work. The optical micrograph in (**a**) shows the 3 mm disk of the electropolished AlMgZn(Cu) alloy with a central hole where the electron-transparent regions are located. Image (**b**) includes the curved scalpel used to make the cuts in the field of view. Steps(**c–e**) show the subsequent cutting made with a sharp laboratory scalpel: note the cuts are made to separate the regions-of-interest around the central hole from the whole 3 mm disk. The optical micrograph in (**f**) shows three pieces of an electron-transparent area that have been cut at higher magnification: a mid-sized piece of size around 50 μm as indicated by the yellow arrow in the inset in (**f**) was selected for transfer onto the microelectromechanical systems (MEMS) chip. The optical micrograph in (**g**) shows the MEMS chip without the sample in its membrane (with holes). The sample is then transferred (**h**) to the MEMS chip by using a piece of brush-bristle with intrinsic static after frictional static charging. The sample is positioned on the MEMS chip membrane as shown in (**i**). The leftover pieces (from the inset in (**f**)) can still be used to produce additional samples in different MEMS e-chips

The methodology consists of selecting an electropolished 3 mm disk that was preconfirmed to have electron-transparent areas around its central hole as shown in Figure 8.1a. These transparent areas are the regions-of-interest (ROI) for the MEMS experiments with in situ S/TEM. The 3 mm disk is placed onto a glass slide. Then, with a sharp laboratory scalpel, a series of cuts are performed on the 3 mm disk in order to isolate parts of the ROI as shown in the set of optical micrographs in Figure 8.1b–e. The samples prepared in this work used a polished sapphire slide as a cutting surface. Sapphire's high hardness means that no visible scalpel scratches result from the cutting process, which, in addition to visible and tactile benefits, means much fewer potential contaminate particles originate from the cutting surface. The general experience with conventional laboratory glass slides is decent, however, especially with softer materials, and is an adequate choice for this procedure. For optimal results when making the cuts, the authors advise using a curved scalpel and aligning the intended cut while the

scalpel tip is in contact with the cutting surface. Firmly lowering the scalpel handle from this position provides the best control and allows the precision necessary to isolate the ROI. With the ROI cut into smaller pieces of around 50–100 µm as denoted, one piece is selected to be transferred onto the MEMS chip as shown in the inset of the optical micrograph in Figure 8.1f.

With the electron-transparent piece (≈50 µm) cut and selected from the ROI, the MEMS chip is placed into the field-of-view: the membrane of the MEMS chip can be seen in the stereo microscope as shown in Figure 8.1g, and this is the target area for the electrontransparent piece. The transfer procedure is performed with the use of an animal hair (taken from a regular high-quality paint brush commonly found in stationery shops). The hair is then statically charged by friction and its tapered point is used to catch the electron-transparent piece and deposit it onto the membrane of the MEMS chip as shown in the micrographs of Figure 8.1h,i. For slight repositioning of the sample upon the membrane, the hair tool can be washed in isopropanol. This serves to remove any residual static charge and allows manipulation of the sample without it attaching to the hair. The electrontransparent piece sticks firmly onto the MEMS e-chips and empirical experience (acquired by repeating this process several times) shows that smaller samples (on the order of the membrane dimensions of the MEMS chip, i.e., 50 µm × 50 µm) do not fall from the MEMS chip during sample loading into the electron-microscope, despite the holder turning upside-down during the loading steps. New practitioners of this procedure will likely find little difficulty when using the scalpel, though will need some small patience when using the hair to manipulate the sample position. A fair analogy would be threading a needle. With practice, the entire process from electropolished disk to positioned sample can take only about 15 min, which was indeed the case for the sample showcased in Figure 8.1.

Some final notes must be made regarding the sample preparation methodology above described. The final quality of the specimen will be dependent on the initial quality of the electropolished 3 mm disks as well as on the overall cutting procedure. While cutting will induce plastic deformation, and therefore dislocations at the cut edges, the ROI is actually the hole's edge, which remains uncut. Although brittle thin samples can be easily cut with a scalpel, the AlMgZn(Cu) alloy used in this work is highly ductile [18] and cutting was also easily performed. Therefore, it is expected that the methodology works for electropolished metallic samples either brittle or ductile. For brittle materials, practitioners can expect that the scalpel, rather than cutting with plastic deformation through the sample, causes fractures and breaks beneath the blade, for the same end-result in ROI isolation. Ceramic materials were not tested in this work, but, given that 3 mm disks can be punched ultrasonically and subsequently mechanically thinned, dimpled and ion-polished (using a precise ion polishing system or PIPS) to electron-transparency, the proposed methodology may also be applicable for this class of materials.

8.3.2. CHARACTERIZATION WITH S/TEM

The electron-transparent piece attached to the MEMS e-chip as shown in Figure 8.1i was loaded into the electron-microscope. Figure 8.2a shows a BF-TEM micrograph taken at low-magnification indicating that the sample was stationary on the MEMS chip during both loading procedures into the

holder and into the electron-microscope. Figure 8.2a also indicates that the sample is covering four holes of the membrane of the MEMS e-chip. A high magnification BF-TEM micrograph was taken from the hole indicated with a blue square in Figure 8.2a: as shown in Figure 8.2b, the sample is high-quality and electron-transparent, thus demonstrating the viability of the proposed sample preparation methodology.
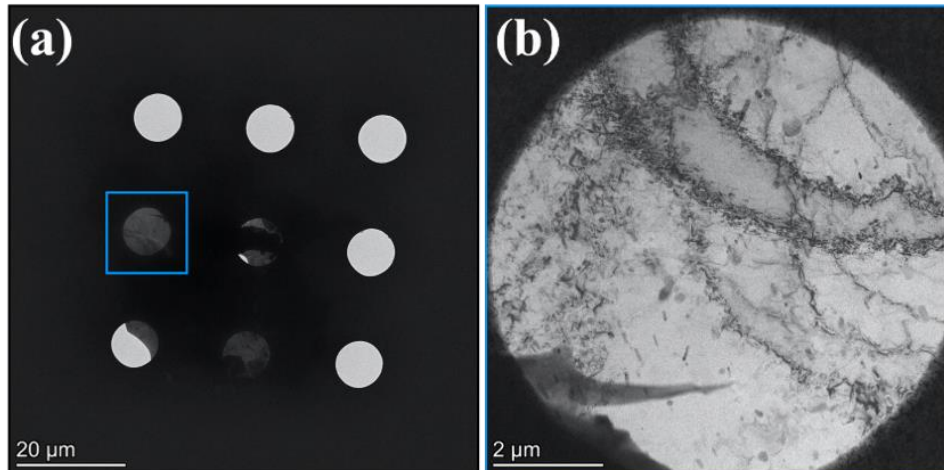

Figure 8.2: Bright-field TEM (BF-TEM) micrographs after the sample preparation procedure showing (**a**) an electron transparent sample of the AlMgZn(Cu) alloy attached to the MEMS chip and (**b**) the sample lying over a hole (indicated by the blue square in (**a**)) on the MEMS chip.

It is worth emphasising that, when using the SEM-FIB for producing samples for MEMS e-chips, Pt is often deposited in specific areas of the sample in order to weld it onto the e-chip membrane [2]. This step may introduce a significant yield of Pt contamination onto the surfaces of the electron-transparent specimen, which may compromise the MEMS experiments. The same is expected to occur upon interaction of either Ga or Xe ion beams with the metallic specimens during the stages of trenching, milling, cutting and polishing within the SEM-FIB. Conversely, in the several steps of the sample preparation methodology reported in this work neither Pt, Ga nor Xe are used; therefore, the sample will be free of those contaminants when compared to samples made within the SEM-FIB.

8.3.3. PAINT BAKE OF ALMGZN(CU) ALLOY WITHIN A S/TEM

In order to evaluate both the quality and performance of the electron-transparent sample during a MEMS experiment a paint bake treatment was performed in situ in the STEM, which consisted of heating the AlMgZn(Cu) alloy up to 458 K for 1200 s. The LAADF micrograph in Figure 8.3a shows the microstructure of the alloy prior to paint bake, which is composed of nanometer-sized Guinier–Preston zones (or simply GP Zones) and a high density of dislocations, given that the alloy was 2% deformed. Note that this is similar microstructure to that found in a conventionally produced AlMgZn(Cu) alloy [18].

Upon paint bake, the microstructural evolution of the AlMgZn(Cu) alloy was monitored in real-time using the BF-STEM and LAADF detectors, the latter of which is shown in the micrographs in Figures 8.3b–e, the former being reported in [18]. A reorganization of the initial dislocation structure was

observed to take place, including complete annihilation of pre-existing dislocations. During the experiment, the sample experienced minimal drift, only on the order of few nanometers, which was easily corrected manually with stage movement.

The SAED patterns shown in Figures 8.4a,b exhibit the microstructure of the AlMgZn(Cu) alloy before and after the paint bake treatment. It is worth emphasising that the SAED patterns before and after the experiment do not show any Debye–Scherrer rings commonly associated with polycrystalline nanometer-sized artefacts introduced by Pt and Ga contamination when using samples produced via the SEM-FIB technique. As this is an experiment performed with an electron-transparent lamella at the nanoscale, the results may not correspond directly to those reported by Stemper, where heat treatment was performed in bulk specimens [18].
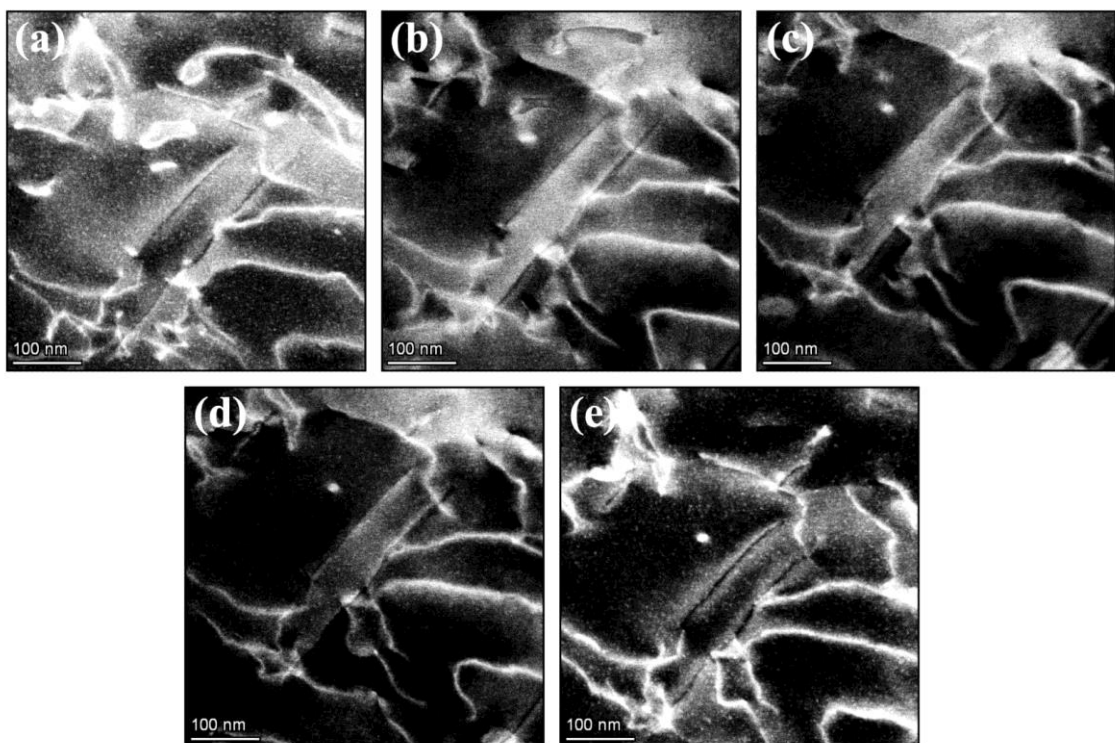

Figure 8.3: Heat treatment of the AlMgZn(Cu) alloy in situ within a scanning/transmission electron microscope (S/TEM) using the MEMS chip. The set of micrographs (**a–e**) and show the microstructural evolution of the AlMgZn(Cu) alloy as a function of time with the low-angle annular dark-field (LAADF) detectors. Micrograph (**a**) was taken prior to paint bake whilst micrographs (**b**), (**c**), (**d**) and (**e**) were taken at 200, 400, 800 and 1200 s, respectively. The corresponding bright-field STEM (BF-STEM) micrographs were reported in [18].
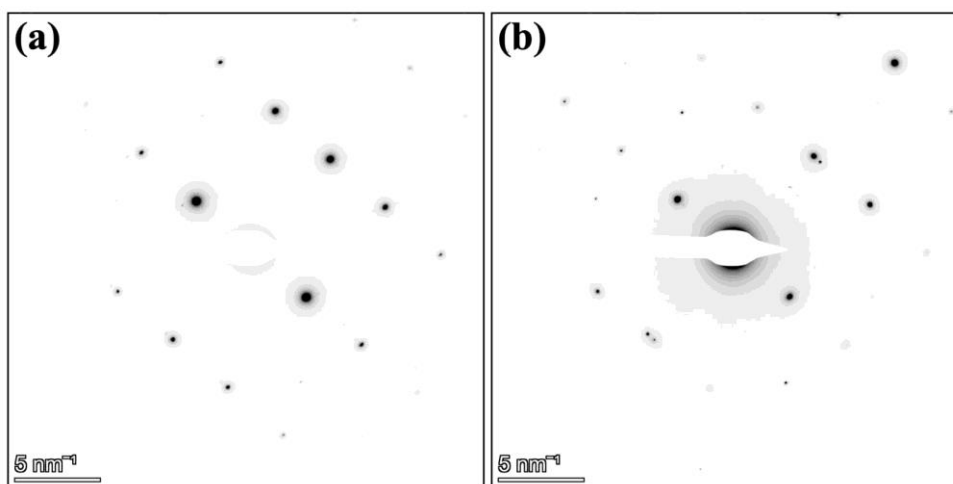
Figure 8.4: Selected-area electron diffraction (SAED) patterns of the AlMgZn(Cu) alloy oriented along [112] zone-axis (**a**) before and (**b**) after paint bake treatment. The additional spots in (**a**) and (**b**) are due to dispersoid phases not in the field of view. The field of view of the SAED patterns correspond to the selected-area aperture covering the whole grain in Figure 8.3a.

8.3.4. POST-EXPERIMENT IMPURITY ANALYSIS

STEM-EDX was used to analyse the elements present in the sample after the in situ STEM paint bake treatment. Figure 8.5 shows a long-exposure (2 h) STEM-EDX raw spec-trum collected from the whole area corresponding to the micrograph in Figure 8.4b. The in-tensity axis (y-axis) of the STEM-EDX plot in Figure 8.5 was set to logarithmic scale in order to better evaluate the presence of minor elemental peaks and a locally estimated scatter-plot smoothing (LOESS) fit was used to better identify the peaks' positions in the energy axis (x-axis). In order to define the relevance of a peak with respect to the background noise, the relative intensity of each identified peak was calculated against the strongest signal peak, e.g., the Al Kα peak index 7 located at 1.487 keV. Peaks with less than 0.01% of relative intensity were not considered.
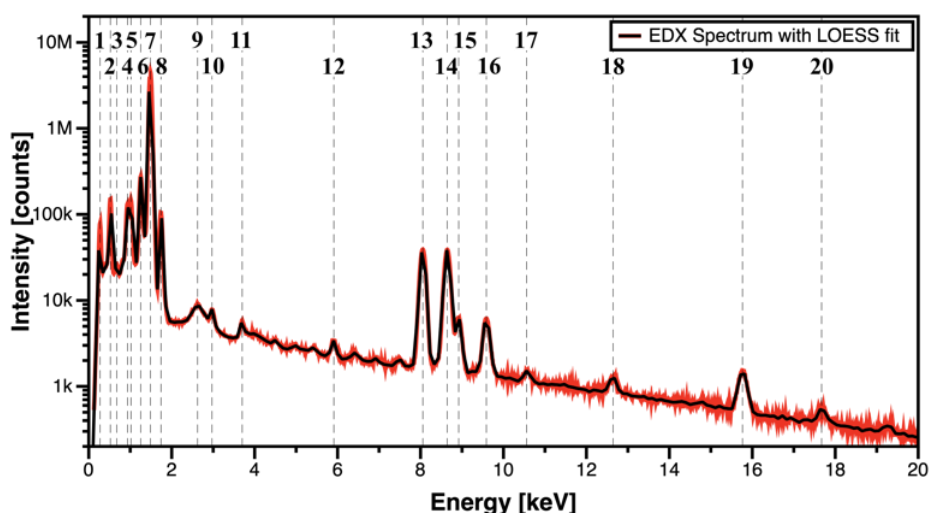
Figure 8.5: STEM energy dispersive X-ray (EDX) raw spectrum acquired from the whole area covered in Figure 8.4b. Note: the y-scale was set to logarithmic in order to maximize visualisation smaller peaks.

Using this methodology, 20 peaks were identified in the STEM-EDX raw spectrum. The peaks' indexes, as well as their energy and relative intensity, were extracted from the plot. The results are shown in Table 8.1 and the accuracy of the STEM-EDX detector is noted. Most of the peaks are confirmed to have an energy match (with their expected position using reference values in the software Velox) in the third decimal place. Given such accuracy, the absence of contaminants such as Pt (Lα = 9.442 keV and Mα = 2.050 keV) and Ga (Kα = 9.251 keV and Lα = 1.098 keV) is remarkably noted. Minor impurities were identified as coming from the alloy production: Ca and Zr with extremely low relative intensity: 0.13% and 0.01% respectively. The presence of O is expected as Al self-passivates. Due to overlap between multiple different elements, the peaks corresponding to labels 3, 9, 10, 12, 17 and 18 were not properly identified, although their relative intensity is below 1%; therefore, we assume these impurities are from the inner microscope electronics, holder, e-chip or background noise.

The only contaminant observed with relative intensity of 1.6% was the element C (peak label 1). It is well known that EDX precludes the identification of the element C [19], but the presence of this small peak can indeed be attributed to carbonaceous contamination either in the surface of the AlMgZn(Cu) sample or in the MEMS e-chip. However, this C contamination can be mitigated with the use of plasma cleaning, which was not applied in this work. Regardless of the minor C contamination and the presence of small impurities, the experiment and its outcomes were not in any way affected as confirmed by the detailed post-paint bake electron-microscopy analysis. No artefacts were observed to nucleate and grow on the alloy microstructure as a result of the experiment.

Table 8.1: STEM-EDX impurity analysis of the paint baked Al alloy.

Peak Index	Measured (keV)	Expected (keV)	Relative‡ (%)	Identified Element
1†	0.273	0.280	1.60	C Kα
2	0.521	0.524	3.20	O Kα
3†	0.675	-	0.61	Multi. Elements
4	0.933	0.929	2.89	Cu Lα
5	1.018	1.012	3.34	Zn Lα
6	1.253	1.254	6.34	Mg Kα
7	1.487	1.487	100	Al Kα

8	1.742	1.742	2.31	Si Kα
9†	2.623	-	0.21	Multi. Elements
10†	2.971	-	0.18	Multi. Elements
11†	3.699	3.691	0.13	Ca Kα
12†	5.910	-	0.08	Multi. Elements
13	8.055	8.048	0.09	Cu Kα
14	8.644	8.639	0.09	Zn Kα
15	8.921	8.907	0.14	Cu Kβ
16	9.587	9.574	0.14	Zn Kβ
17†	10.558	-	0.04	Multi. Elements
18†	12.643	-	0.03	Multi. Elements
19†	15.764	15.775	0.04	Zr Kα
20†	17.671	17.667	0.01	Zr Kβ

†Note 1: all the identified impurities have low relative intensity (i.e., the signal from impurities are comparable to noise).

‡Note 2: the relative intensity was calculated with respect to the most intense peak in the spectrum (the Al Kα peak index 7).

8.4. CONCLUSIONS

An alternative method for producing good-quality and implantation-free electron-transparent samples for MEMS experiments in situ within a S/TEM was introduced in this paper. The method consisted of using electropolished 3 mm disks from metallic samples with an electron-transparent hole in the center. The disk is then subjected to a set of precise cuts in order to separate the electron-transparent region into smaller pieces of around ≈50 μm. The electron-transparent piece can be transferred to pristine MEMS e-chips, with a high-quality animal hair used as a micrometer-sized manipulation tool.

The introduced methodology is faster than SEM-FIB and it allows the sample preparation of multiple samples from only one 3 mm electropolished disk. A paint bake experiment of an AlMgZn(Cu) alloy was performed in order to attest the quality of the sample and its stability during an in situ STEM experiment. Yield of minor impurities were observed to come from the Al alloy itself rather than the sample preparation method. The only minor extrinsic contamination observed was C, which is commonly identified when using the EDX technique for elemental estimation. None of the minor impurities nor C contamination were observed to affect the results of the paint bake experiment as no arte-facts were observed to form and evolve in the sample.

This sample preparation methodology works well for both ductile and brittle metallic 3 mm electropolished disks, but it has not been yet tested for 3 mm dimpled and ion-polished ceramic discs.

8.5. REFERENCES

[1] Noh, K.; Sun, L.; Chen, X.; Wen, J.; Dillon, S. In Situ TEM Characterization of Electrochemical Systems. *Microsc. Microanal.* **2011**, *17*, 1572–1573.

[2] Zhong, X.L.; Schilling, S.; Zaluzec, N.J.; Burke, M.G. Sample Preparation Methodologies for In Situ Liquid and Gaseous Cell Analytical Transmission Electron Microscopy of Electropolished Specimens. *Microsc. Microanal.* **2016**, *22*, 1350–1359.

[3]   Damiano, J.; Nackashi, D.P.; Mick, S.E. A MEMS based Technology Platform for in-situ TEM Heating Studies. *Microsc. Microanal.* **2008**, *14*, 1332–1333.

[4]   Novák, L.; Stárek, J.; Vystavěl, T.; Mele, L. MEMS-based Heating Element for in-situ Dynamical Experiments on FIB/SEM Systems. *Microsc. Microanal.* **2016**, *22*, 184–185.

[5]   Hattar, K.; Han, J.; Saif, T.; Robertson, I.M. Development and Application of a MEMS-Based In Situ TEM Straining Device for Ultra-Fine Grained Metallic Systems. *Microsc. Microanal.* **2004**, *10*, 50–51.

[6]   Tochigi, E.; Sato, T.; Shibata, N.; Fujita, H.; Ikuhara, Y. In situ STEM Mechanical Experiments at Atomic-Resolution Using a MEMS Device. *Microsc. Microanal.* **2019**, *25*, 1884–1885.

[7]   Dillon, S.J.; Liu, Y. In-Situ TEM in Complex Environments: Photocatalysis. *Microsc. Microanal.* **2012**, *18*, 1072–1073.

[8]   Sun, L. In-situ TEM Study on Solar Cell. *Microsc. Microanal.* **2020**, *26*, 3160.

[9]   Li, W.; Li, M.; Wang, X.; Xu, P.; Yu, H.; Li, X. An in-situ TEM microreactor for real-time nanomorphology & physicochemical parameters interrelated characterization. *Nano Today* **2020**, *35*, 100932.

[10] Imrich, P.J.; Kirchlechner, C.; Kiener, D.; Dehm, G. In Situ TEM Microcompression of Single and Bicrystalline Samples: Insights and Limitations. *JOM* **2015**, *67*, 1704–1712.

[11] Tuck, K.; Ellis, M.; Geisberger, A.; Skidmore, G.; Foster, P. FIB Prepared TEM Sample Lift-out Using MEMS Grippers. *Microsc. Microanal.* **2004**, *10*, 1144–1145.

[12] Vijayan, S.; Jinschek, J.R.; Kujawa, S.; Greiser, J.; Aindow, M. Focused Ion Beam Preparation of Specimens for Micro-Electro-Mechanical System-based Transmission Electron Microscopy Heating Experiments. *Microsc. Microanal.* **2017**, *23*, 708–716.

[13] Giannuzzi, L.A.; Stevie, F.A. A review of focused ion beam milling techniques for TEM specimen preparation. *Micron* **1999**, *30*, 197–204.

[14] Mayer, J.; Giannuzzi, L.A.; Kamino, T.; Michael, J. TEM Sample Preparation and FIB-Induced Damage. *MRS Bull.* **2007**, *32*, 400–407.

[15] Ernst, A.; Wei, M.; Aindow, M. A Comparison of Ga FIB and Xe-Plasma FIB of Complex Al Alloys. *Microsc. Microanal.* **2017**, *23*, 288–289.

[16] Bender, H.; Franquet, A.; Drijbooms, C.; Parmentier, B.; Clarysse, T.; Vandervorst, W.; Kwakman, L. Surface contamination and electrical damage by focused ion beam: Conditions applicable to the extraction of TEM lamellae from nanoelectronic devices. *Semicond. Sci. Technol.* **2015**, *30*, 114015.

[17] Estivill, R.; Audoit, G.; Barnes, J.-P.; Grenier, A.; Blavette, D. Preparation and Analysis of Atom Probe Tips by Xenon Focused Ion Beam Milling. *Microsc. Microanal.* **2016**, *22*, 576–582.

[18] Stemper, L.; Tunes, M.A.; Dumitraschkewitz, P.; Mendez-Martin, F.; Tosone, R.; Marchand, D.; Curtin, W.A.; Uggowitzer, P.J.; Pogatscher, S. Giant hardening response in AlMgZn(Cu) alloys. *Acta Mater.* **2021**, *206*, 116617.

[19] Isabell, T.C.; Fischione, P.E.; O'Keefe, C.; Guruz, M.U.; Dravid, V.P. Plasma Cleaning and Its Applications for Electron Microscopy. *Microsc. Microanal.* **1999**, *5*, 126–135.

9. CONCLUSIONS AND OUTLOOK

As material demands in frontier technologies grow ever more complex, more intricate characterisation of material changes becomes ever more important in state of the art material science. Meanwhile, the development of fundamental theory requires better precision and exploiting new measurement opportunities. Micro-electromechanical systems (MEMS) offer highly capable electronic sensing components, and their implementation and integration in scientific analysis is hugely advantageous in bridging the technology gap to novel measurements and more comprehensive characterisation techniques.

With regards to metallic systems, MEMS based experiments are extremely valuable tools which, combined with metallurgical theory, improve understanding of material properties. With FSC for instance, existing and novel alloys can be examined at states far from equilibrium to measure and evaluate dynamic thermochemical properties. This is highly relevant to optimisation of processing parameters in state of the art production methods. Additive manufacturing is an example of this, but the kinetics of microstructural changes are hugely important to alloy development and metallurgy in general, and MEMS-based experiments provide a valuable approach to better understanding here.

The initial publication included in Chapter 6 conducts demonstrative heap capacity measurements using pure Pb as an evaluation standard. First showing the poor accuracy of heat capacity curves determined from the measured heat flow, two approaches to heat flow correction are implemented and evaluated by their impact on the determined specific heat capacity. Both methods involve measuring and accounting for systematic heat losses and provide similar improvements in comparison to literature data, and to be similarly affected by sample mass and heating rate during measurement. Crucially, the slow-rate heat flow correction is most relevant in the study of metallic alloys. Of the four samples examined on UFS 1 MEMS chip sensors, those with middling mass of 1-3 µg performed best, while the programmed heating rates were less impactful on the final measurement result. Good consistency and temperature dependence was found for each sample, and as such the inaccuracy compared to literature values of c_p is attributed to inaccuracy in sample mass determination. The methodology and results aid both in their description of heat loss correction in FDSC, and generally in informing broader FDSC measurements on metallic materials using UFS 1 chip sensors.

The following Chapter 7 continues to address precise heat capacity determination, this time using the high temperature UFH 1 MEMS chip sensors and examining pure Al and eutectic Al-Si. Rapid heating rates and rapid cooling rates are implemented, and their impacts on the determined heat capacity is evaluated. To negate the observed drift in measured heat flow, the slow-rate heat loss measurement is integrated into an iterative temperature program, while averaging the corrected heat flow curves improved the signal to noise ratio. The determined c_p of pure aluminium allows easy assessment of the experiment methodology which is then applied to Al-Si metallic powder. Heating rate during the measurement, as well as the prior quench rate from liquid, is found to majorly impact the measured apparent heat capacity curves due to the precipitation of Si from the super saturated

solid solution. The rapid heating rates examined are highly relevant to metal additive manufacturing, which involves temperature changes in the tens of thousands of Kelvin per second. The results also describe the impacts on the behaviour and degree of Si precipitation, which can reveal a lot about an alloy's kinetic properties. A similar approach of heat loss correction for the c_p measurements taken here could be adapted to suit many high precision measurements on metallic materials, and promises good accuracy and reproducibility.

Using sample preparation techniques generally chosen for FDSC experiments, Chapter 8 includes a publication where metallic samples were prepared from foils and examined inside a TEM and subjected to in-situ MEMS heating experiments. A paint bake thermal treatment was implemented on an AlMgZn(Cu) crossover alloy and its microstructural evolution was monitored in the LAADF detector and by selected area electron diffraction (SAED). Compositional analysis using energy dispersive X-ray spectroscopy (STEM-EDX) showed only impurities from the alloy itself, and C which is common using the EDX technique, with none of the impurities associated with FIB-based sample preparation. Instead, from electropolished 3mm disks of the alloy, electron transparent samples are sectioned by hand with a scalpel and transferred to the MEMS e-chip using a hair stylus. In many cases this approach may be more convenient and superior to FIB-based sample preparation, and is described in some detail to enable its reproduction. MEMS chips also make calorimetry possible in a TEM, and is a promising direction for in-situ structural and thermal investigations of metallic materials in general.

The investigations undertaken in these manuscripts have collected measurements which are useful in their own right in a material-specific sense, and also demonstrate the high precision capabilities of some state-of-the-art MEMS technologies. For such measurements to take full advantage of these frontier technologies, full attention must be given to experimental approach and sample preparation. It is in this respect that the content of this thesis holds its widest relevance; in exploiting the means of current technologies to realise their maximum potential, and drive novel research at the frontiers of materials science.

"…every branch of physical science must consist of three things; the series of facts which are the objects of the science, the ideas which represent these facts, and the words by which these ideas are expressed. Like three impressions of the same seal, the word ought to produce the idea, and the idea to be a picture of the fact."

"Perhaps…someday the precision of the data will be brought so far that the mathematician will be able to calculate at his desk the outcome of any chemical combination, in the same way, so to speak, as he calculates the motions of celestial bodies."
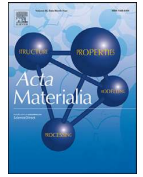
—Antione-Laurent Lavosier, 1743-1794

10.   ADDITIONAL CONTRIBUTIONS TO PUBLISHED WORKS

10.1.   MEMS-BASED IN SITU ELECTRON MICROSCOPY INVESTIGATION OF RAPID SOLIDIFICATION AND HEAT TREATMENT ON EUTECTIC AL-CU*

This work followed a similar methodology for producing electron transparent samples as that outlined in Chapter 8, and investigated the behaviour of the lamellar microstructure of AlCu eutectic subject to various thermal treatments. Spheroidisation of lamellas and grain boundary movement are observed in the solid state at elevated temperatures, and a model is put forward based on cooling rate, lamellar spacing and interfacial energy.

MEMS-Based in situ electron-microscopy investigation of rapid solidification and heat treatment on eutectic Al-Cu

Phillip Dumitraschkewitz [a],*, Matheus A. Tunes [c], Cameron R. Quick [a], Diego Santa Rosa Coradini [a], Thomas M. Kremmer [a], Parthiban Ramasamy [b], Peter J. Uggowitzer [a], Stefan Pogatscher [a]

[a] *Chair of Nonferrous Metallurgy, Department of Metallurgy, Montanuniversitaet Leoben, Franz-Josef-Str. 18, 8700, Leoben, Austria*
[b] *Erich Schmid Institute of Materials Science, Austrian Academy of Sciences, Jahnstraße 12, Leoben A 8700, Austria*
[c] *Materials Science and Technology Division, Los Alamos National Laboratory, United States*

ABSTRACT

The solidification behavior of a eutectic AlCu specimen is investigated via *in situ* scanning transmission electron microscope (STEM) experiments. Solidification conditions are varied by imposing various cooling conditions via a micro-electro-mechanical system (MEMS) based membrane. The methodology allows the use of material processed by a melting and casting route close to industrial metallurgically fabricated material for *in situ* STEM solidification studies. Different rapid solidification morphologies could be obtained solely on a single specimen by the demonstrated strategy. Additional post-solidification heat treatments are investigated in terms of observation of spheroidization of lamellas during annealing at elevated temperatures.

1. Introduction

Eutectic alloys are classical and well studied metallurgical systems. In particular, the Al-Cu system is a regular eutectic system, which is defined by coupled growth of phase constituents from the melt [1,2].

The rise of additive manufacturing [3] and rapid solidification [1,4,5], as well as the emergence of the so-called eutectic high-entropy alloys (EHEA) [6,7], has led to new fundamental research efforts in the scope of eutectic alloys which resulted in a revisit to the Al-Cu system [8–11].

Regular eutectic systems are characterized by a lamellar or rod morphology, which is the result of the interfacial α factor for the constituent phases. The interfacial factor mainly depends on the entropy of fusion and on crystal structure and orientation. If both eutectic constituents have an interfacial factors $\alpha \leq 2$, a regular eutectic is expected. Depending on the composition of the near eutectic binary, either rod or lamellar morphology is expected [1].

Tiller [12] formulated scaling laws for the dynamics of lamellar eutectic growth from the melt (eutectic scaling laws, see Eqs. (1), (2) and (3)) by using the principle of a minimum of the total interfacial undercooling ΔT. The eutectic scaling laws describe the relationship between undercooling, solidification velocity v and resulting optimal steady state lamellar spacing λ. Tiller's model was later further refined by Glicksman [1], Hunt and Jackson [13], Lemaignan [14]

$$\lambda^2 v = \text{const.} \tag{1}$$

$$\frac{\Delta T^2}{v} = \text{const.} \tag{2}$$

$$\Delta T \lambda = \text{const.} \tag{3}$$

Under high solidification velocities, as common for rapid solidification processing (RSP), the theoretical model defined by

---

* Corresponding author.
E-mail addresses: phillip.dumitraschkewitz@unileoben.ac.at (P. Dumitraschkewitz), matheus.tunes@unileoben.ac.at (M.A. Tunes), stefan.pogatscher@unileoben.ac.at (S. Pogatscher).

the eutectic scaling laws has limited applicability since different microstructures are able to form such as degenerate eutectics, cell/dendrites, bands and extended solid solutions [15].

Gill and Kurz [15,16] experimentally and theoretically investigated a microstructure selection map for the Al-Cu system. *Ex situ* experiments within a transmission electron microscope (TEM) on rapid laser solidification processed material were conducted [15] and compared to predictive theoretical calculations using eutectic, dendritic, banding and plane front growth models [16]. The morphology transition for the eutectic composition, from low to highest experimental solidification velocities, is reported in Eq. (4) [16].

$$\text{lamellar eutectic} \rightarrow \text{cellular and dendritic} \rightarrow \text{banded} \qquad (4)$$

In general, ultimately increasing the solidification velocity can lead to partitionless solidification via solute trapping resulting in a partition coefficient of unity [17], the formation of quasicrystals [18] or vitrification as experienced in bulk metallic glasses [19].

For Al-Cu alloys, innovative methods have permitted direct and real-time observation of the solidification process in hypo-eutectic compositions in recent years [9–11]. By means of dynamic TEM (DTEM) [9] and movie-mode TEM (MM-TEM) [10,11], the solidification behavior of an *in situ* pulse-laser-melted pre-deposited hypo-eutectic Al-Cu film has been investigated. The material was prepared by electron beam evaporation of the pure materials onto a Si_3N_4 membrane. With a pulsed laser, an elliptical melt pool of $\approx 50~\mu m$ was created locally and solidified by natural cooling, mainly driven by in-plane heat conduction of the surrounding solid. The solidification velocity increased during the solidification and reached a maximum of ≈ 1.4 m/s. [11]

A different approach for *in situ* electron-microscopy rapid solidification studies in the Al-Cu eutectic system is herein investigated. In general, the methodology presented allows usage of material processed by a melting and casting route, which is closer to industrial, metallurgically fabricated material than usual in *in situ* S/TEM solidification studies. Moreover, the sample production method is expected not to be limited to a single alloy system. Additionally, the method can be time-saving if compared to a focused ion beam (FIB) sample production routine. The applicable time-temperature (t-T) programs for heat treatments are various below the maximum temperature range 1200 °C [20] of the membrane. This is especially true for relative short time spans, and could also be used to mimic t-T profiles of additive manufacturing cycles including solidification.

Utilizing a MEMS-based heating/cooling membrane, an electron transparent specimen, prepared by a simple method, is investigated. To demonstrate the capabilities of the methodology, different solidification velocities are explored in a single sample by imposing different cooling conditions via the chip. Additional post-solidification heat treatments are conducted and changes on the microstructure in terms of spheroidization of lamellas are investigated.

2. Experimental methods

The material was produced by induction melting (Indutherm MC100V) and die casting, starting from the pure metals Al (99.99 wt.%) and Cu (99.99 wt.%) to a target nominal composition of 17.39 at.% Cu. The melting process was conducted under Ar atmosphere. The material was melted at 700 °C, held for approximately 10 min, and cast.

Pieces of the ingot were cut, ground and analyzed via optical emission spectroscopy (OES) of type SPECTROMAXx. The composition measured was 82.48 at.% Al and 17.52 at.% Cu.

A volume of approx. 2×10^3 mm, cut from the bottom third of the ingot, was used for melt-spinning. Several meters of ribbons could be produced of usable quality. The thickness of the produced ribbons varied from approximately 30 μm to 50 μm.

For scanning electron microscopy (SEM) analysis a SEM type Jeol JSM-IT300 equipped with a EDS system (Oxford X-Max^{50}) was used.

For STEM sample preparation, pieces of the melt-spun ribbons were cut and manually polished. The polished ribbons were punched and electro-polished with a mixture of a 1/3 nitric acid (HNO_3) and 2/3 methanol (CH_3OH). A jet electro-polishing (JEP) setup was used (TenuPol-5). The electrolyte was cooled down with LN_2 to -20 °C and a voltage of 12 V was applied. After JEP, the material was washed in a sequence of three beakers containing pure methanol.

Following this, a small piece of material ($\approx 50~\mu$m) was cut from the electro-polished sample with a scalpel. The small sample was positioned on a Protochips Fusion Select *in-situ* heating/cooling holder chip by hand using a natural grown animal hair as a manipulator stylus (for more details on this new procedure please see Reference [21,22]). The entire positioning and cutting was performed using a stereo microscope. This procedure is initially known from chip calorimetry [23–26], though the samples used there are comparatively thicker, usually in the range of several μm. The sample was positioned such that the thin, electro-transparent area covered the MEMS membrane holes which are intended for observation of a sample. Due to the size of the sample, several membrane holes were fully or partly covered, see exemplary Fig. 1a.

For temperature control the Protochips Fusion Clarity program was used, which operates a Keithley 2450, utilizing a standard control time-step time of 100 ms.

The sample was investigated by scanning transmission microscopy high angle annular dark field (STEM-HAADF) and EDS with a ThermoFisher Scientific^{TM} Talos F200X G2 scanning transmission electron microscope with an acceleration voltage of 200 kV and at a pressure of $\approx 8 \times 10^{-6}$ Pa.

3. Results

In the following, the morphology for different conditions resulting from different time temperature programs are presented. In general, the results are organized according to the structure of the overview Fig. 1. Figure 1b and c show the pristine sample. In Fig. 1d, e and f the time temperature program and the coarsened state are reported; furthermore, in Fig. 1g, h and i the respective information and images of a melted and re-solidified state are given.

The morphology of the pristine material and the specimen is briefly described in the following last paragraph due to the generality of observed features, which is also referred to in later sections.

We give two detailed examples for application of our newly developed methodology. Firstly, the description of the spheroidization behavior, especially of a lamellar structure, including the measurement of an interface velocity follows in Section 3.1. And secondly, structures generated upon melting and re-solidification are presented in Section 3.2.

In Fig. 1b, a high-angle annular dark field (HAADF) image of the pristine, as-meltspun, sample is shown. No unidirectional morphology of lamellas is obtained in the field-of-view, but colonies of lamellas can be identified in subdomains. The dark areas are identified as the α-Al eutectic constituent, due to the z-contrast of HAADF and the relative high z-number of Cu, and the bright areas accordingly θ-Al_2Cu. Energy dispersive X-ray spectroscopy (EDS, seen in Fig. 1c, f and k) does confirm the high Cu content
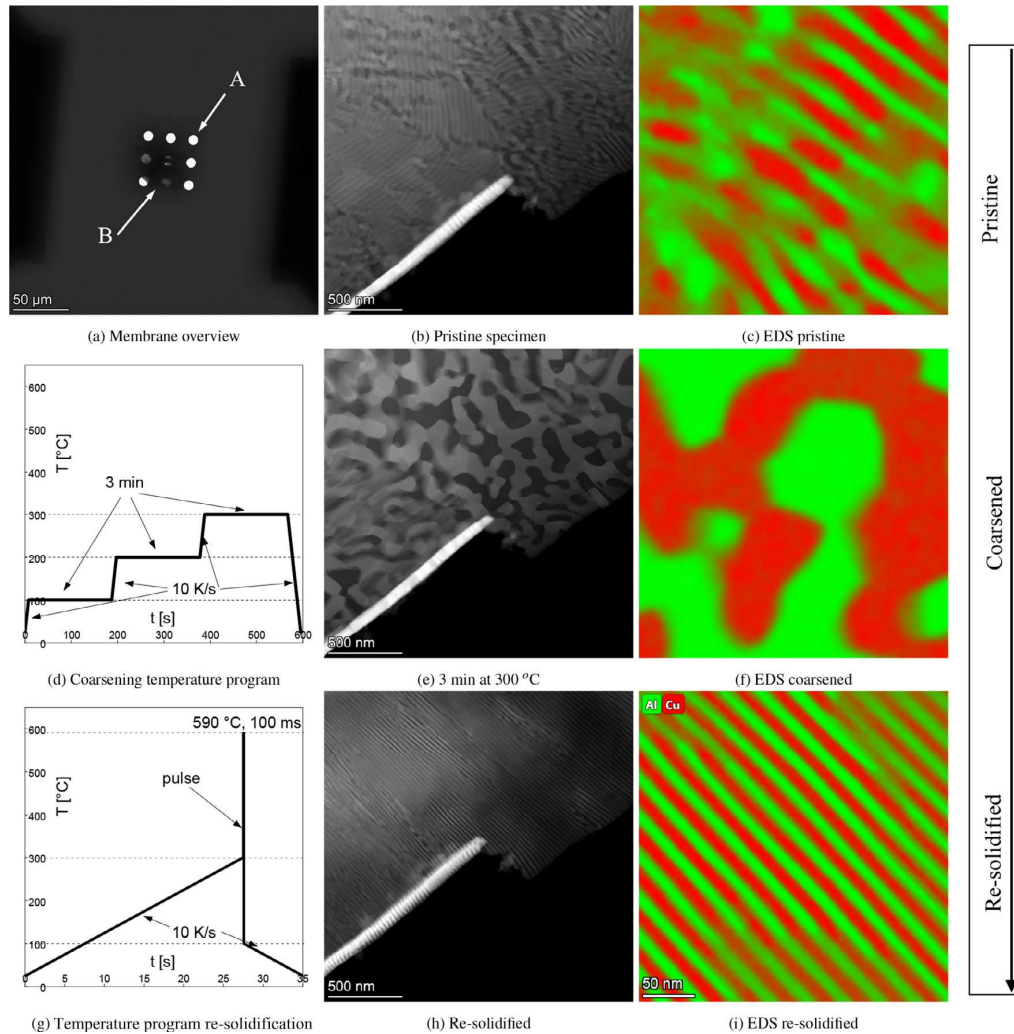
Fig. 1. Overview of the membrane, HAADF and EDS images of the pristine, coarsened pristine and re-solidified material with corresponding temperature programs. a) Membrane overview with membrane holes [22] (feature A) and specimen (feature B). Following microstructures are obtained: b,c) lamellar colonies with varying orientation; e,f) interconnected spheroidized grains; h,i) unidirectional lamellas. Bright areas in HAADF show the θ-Al$_2$Cu and dark areas are α-Al phase as identified by EDS. h,i) After re-solidification a newly formed nanostructured hierarchy is obtained, consisting of α-Al and θ-Al$_2$Cu unidirectional lamellas. The bright feature, reaching approximately into the center of the figure b,e,h), is a roll-up of the sample.

of the bright lamellas (for direct comparison see also Fig. B.1). The bright area, reaching approximately into the center of the figure, is a roll-up of the sample. The minimum lamellar spacing is $\lambda \approx 32$ nm in the pristine sample. It should be noted that this value is the peak to peak value, analogous to a wavelength.

3.1. Spheroidization and coarsening of lamellar structures

The spheroidization behavior for annealing at 300 °C for 3 min of the pristine material can be observed in Fig. 1e (see also Ref. [27] video 1). In the pristine material, nucleation of polyhedra grains at the front of the colonies of the θ lamellas is observed, which grow at the cost of dissolving lamellas and form a mostly inter-connected θ-grain network.

For the unidirectionally oriented lamella morphology (Fig. 1j), growth in width of θ lamellas (further refered to as "thickening", feature A in Fig. 2) and spheroidization (feature B in Fig. 2) is observed while annealing at 300 °C.

Several previously parallel lamellas are seen to form interconnected, significantly elongated round grains after 3 min at 300 °C (Fig. 3a).

Lamella faults are often found to be nucleation points for thickening and spheroidization. For thickening of lamellas, the increase in width follows the main direction of the lamella at the cost of neighboring lamellas (see Ref. [27], video 2 and Fig. 2). Annealing at 500 °C for 3 min leads to coarser elongated spheroidized grains (Fig. 3b).

3.1.1. Recrystallization kinetics of lamellar colonies

The thickening of a lamellar at the cost of a neighboring lamella, feature A in Fig. 2, is measured to be ≈ 41 nm/s on average for an isothermal holding temperature of 300 °C (see also Ref. [27], video 2).

For several frames, the length of the initial (dissolving) lamella is measured and tracked. The time t is calculated with a frame-to-frame time Δt of 706 ms, setting the time for the reference frame
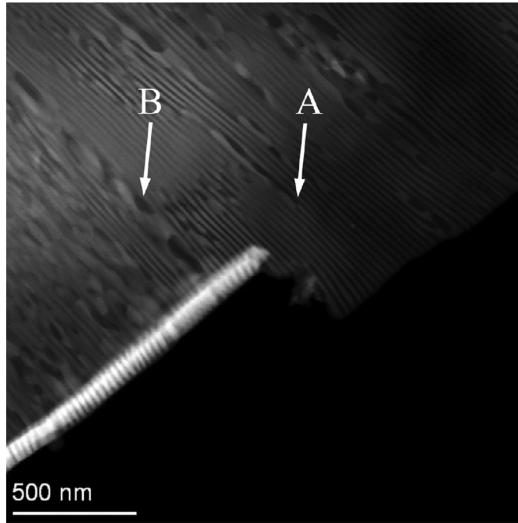
Fig. 2. HAADF image of coarsening at 300 °C (Video 2). Feature A shows thickening of a lamella. Feature B shows beginning spheroidization of lamellas.

$n_{frame,initial}$ as origin to zero, and for further frames numbers n_{frame} according to Eq. (5).

$$t = \Delta t \left(n_{frame} - n_{frame,initial} \right) \tag{5}$$

The first frame shows a length for the inital lamella of 584.4 nm (Δs_{max}) and the λ value is $\approx$ 22 nm. In the last used frame the initial lamella vanished (Ref. [27], video 2, frames 148–168). The average velocity v_{avg} is calculated according to Eq. (6), where $\Delta t_{max} = 14.12$ s, yielding 41 nm/s.

$$v_{avg} = \frac{\Delta s_{max}}{\Delta t_{max}} \tag{6}$$

Interval velocities v_{int} are computed according to Eq. (7), where $\Delta s_{interval}$ and $\Delta t_{interval}$ are the respective length differences of the initial lamella and time differences between two frames.

$$v_{int} = \frac{\Delta s_{interval}}{\Delta t_{interval}} \tag{7}$$

The interval velocities vary from in the range of 23 - 71 nm/s.

3.2. Melting and re-solidification

Two re-solidification experiments are are presented in Fig. 4. As the main parameter the cooling conditions are varied; pulse heating with free cooling and cooling with 100 K/s is utilized.

During the progression in number of experiments, holes developed in the specimen at the partly covered membrane hole (Fig. 4b, feature A). It should be noted that the specimen is thicker at feature B. In general the sample area shrinks and the thickness can increase over the sequence of meltings.

Cooling with a rate of 100 K/s during solidification results in a coarse more 3-dimensional morphology (Fig. 4b at feature B). Large thin dendritic crystals, either α or θ, at the surface are covering lamella morphologies behind them. Not only a single structure through the whole thickness of the sample is apparent in the field-of-view.

Solidification after a pulse heating and free cooling resulted in unidirectionally oriented lamellas with a λ_{min} of $\approx$ 22 nm, see Fig. 4a.

The overall composition of the pristine sample is measured to be $\approx$ 14.6 at.% Cu and 85.4 at.% Al in balance. Further EDS measurements are reported in Table B.1 and discussed in Section 4.2.1.
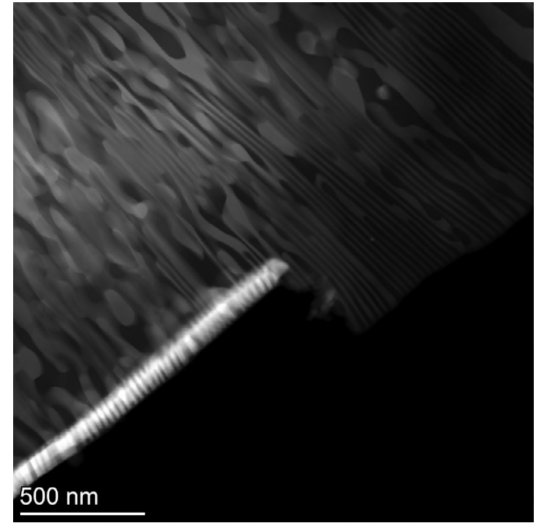
(a) Coarsened at 300 °C for 3 min
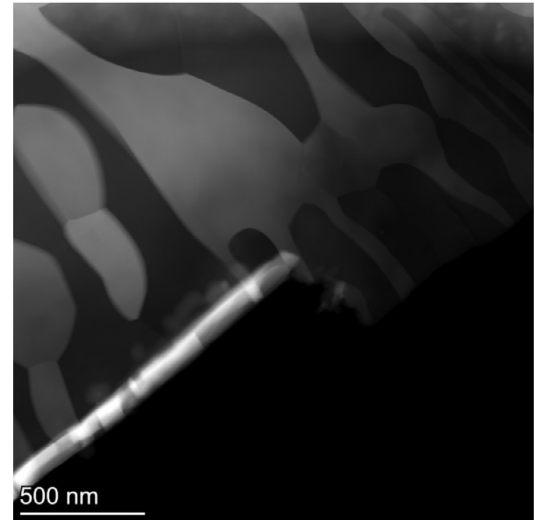
(b) Coarsened at 500 °C for 3 min

Fig. 3. HAADF images of coarsened material after pulse heating and free cooling. a) lamellar spheroidization and lamellar thickening. b) Additional coarsening heat treatment lead to coalescence and growth of grains.

Notably, it should be mentioned that the roll-up feature of the image is retained, even after melting and re-solidifcation.

4. Discussion

In the following, spheroidization is discussed and a term for the thermodynamical driving force for a special case is developed (Section 4.1). Please note that additional details on the derivation of the model are given in the appendix and only the essential parts are reproduced in the main text for better readability and to focus on the main result. Moreover, the re-solidified morphologies are discussed in Section 4.2.

4.1. Lamella spheroidization and coarsening

A rough estimation of the coarsening rate of eutectic lamellas has already been conducted by Lemaignan [14], but also stated that

(a) pulse heating and free cooling
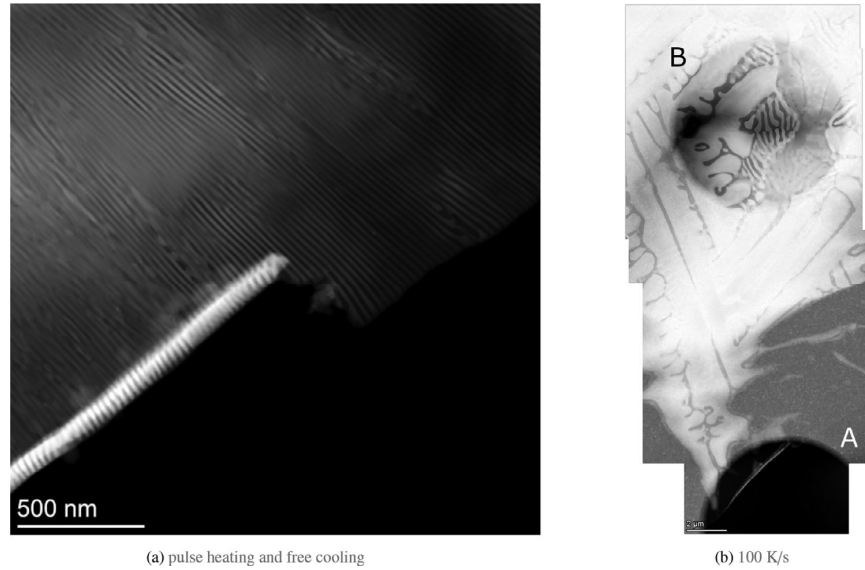
(b) 100 K/s

Fig. 4. HAADF images for re-solidification experiments with varied cooling conditions; after a pulse heating and free cooling (a) and cooling with 100 K/s (b). Image in a) was taken at the partly covered membrane hole; feature A in b). Following microstructures are obtained: a) strong unidirectional lamellar, b) coarse lamellar and surface grains. Note that b) is a stitch out of 4 images from a video sequence.

the geometrical situation is different for lamellar eutectic systems than in the applied model. The equation initially used for the estimation was built for smaller solid particles/dispersoids dissolving to benefit the growth of larger particles in a liquid [28].

In Reference [29], the driving force of recrystallization p is given by the free enthalpy reduction $-dG$ gained by passing the grain boundary over a volume dV, see Eq. (8).

$$p = -\frac{dG}{dV} \tag{8}$$

Several expressions for p can be found assuming different driving forces for recrystallization, e.g. for continuous recrystallization Eq. (9) is stated [29], where γ denotes the grain boundary energy and R the radius of curvature.

$$p = \frac{2\gamma}{R} \tag{9}$$

For the special case of thickening a θ-lamella at the cost of a neighbor (Fig. 2, feature A), as observed in video 2 Ref. [27] during annealing at 300 °C, an expression for p is developed (see Appendix A) and reported in Eq. (10). $\gamma_{\alpha\theta}$ denotes the columnar interface energy of the α/θ lamellas and λ_{init} the initial lamella distance.

$$p = \frac{2\gamma_{\alpha\theta}}{\lambda_{init}} \tag{10}$$

For a hemispherical grain ending in a differently oriented grain, Eq. (11) is given [30]. For a similar case, a triple junction, where a grain ends between two differently oriented grains, a driving force as in Eq. (12) is reported [31,32], where w represents the grain width. β is the grain boundary angle with possible values ranging from 0 to $\pi/3$ in the model, if the shrinking grain is not dragged by the triple junction itself.

Using λ for w shows that Eq. (10) matches Eq. (11), or respectively lies in the range of Eq. (12), below the limiting case. If no drag of the triple junction slows the boundary movements, the angle $\beta = \pi/3$ as limiting case can be used [30]; comparing Eqs. (10) or (11) to (12) leads a ratio of 2 to $2\pi/3$. It should be noted that Eq. (12) was derived by a formalism surface tension act-
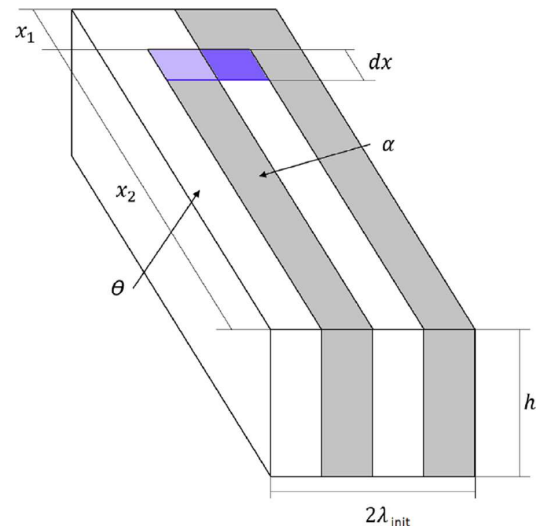
Fig. 5. Simplified geometry for lamella thickening. h is the thickness of the sample, dx is the movement of the interface with a time interval and λ_{init} is the initial lamella spacing. The bright blue area changes from α to θ phase, and the dark blue area from θ to α, during the interface movement of dx. (For interpretation of the references to colour in this figure legend, the reader is referred to the web version of this article.)

ing on boundary [32].

$$p = \frac{2\gamma}{w} \tag{11}$$

$$p = \frac{2\beta\gamma}{w} \tag{12}$$

However, in the present case, four grains meet with two of them of different phase (Fig. 5). The different geometric situation will therefore contribute to differences in derived expressions.

The geometry of the connected grains cannot be clearly observed with the used magnification of Fig. 2. In the derivation of Eq. (10), the influence of bowed interface lines is neglected. Flat lines would actually create locking of the boundary lines [33], but, the free ending corners in Fig. 5 introduce points of instability. Here it should be emphasized that the lamella defects are seen to be nucleation points for thickening of lamellas and also elicit spheroidization. Further, for the energetic derivation formalism only the self-similarity of the front interface before and after the movement of dx is needed.

Another general simplification made for Eq. (10), as in the other two dimensional cases, is the assumption of a constant height of the sample, when actually the sample is likely wedge-shaped and gets thinner towards the sample edge. This could explain the faster movement [34,35] of feature A in Fig. 2, in comparison to a slow moving, similar feature in the opposite direction. A deleterious effect of grain boundary grooving is not expected for Al due to an existing oxide layer [35,36]. Faster recrystallization velocity could be caused by smaller sample thickness.

An estimation of the driving force acting in Fig. 2 by Eq. (10), with $\gamma_{\alpha\theta} \approx 253$ mJ/m² [37] and $\lambda_{init} \approx 22$ nm, gives a value of ≈ 20 MPa, reaching driving forces in the order of primary recrystallization of heavily cold worked metals [29].

To physically assess the kinetics of lamellar thickening, we first consider the thickening rate without taking into account the exact mechanism. With the driving force p and the mobility m of the phase boundaries, the velocity $\tilde{v}$ according to Gottstein [29] results in

$$\tilde{v} = mp,\tag{13}$$

whereby the mobility is specified in relation to the migration-determining diffusion coefficient D_m, the jumping distance b, the Boltzmann constant k and the absolute temperature T with

$$m = \frac{b^2 D_m}{kT}.\tag{14}$$

With $a = 0.405$ nm as the fcc lattice constant, b is estimated by $b = \sqrt[3]{a^3/4}$ [38]. The diffusion coefficient can therefore be expressed by Eq. (15).

$$D_m = kT \frac{\lambda_{init}}{2\gamma_{\alpha\theta} b^2} \tilde{v}\tag{15}$$

Inserting the isothermal temperature of 300 °C (573 K), with the values for λ_{init} and $\gamma_{\alpha\theta}$ given earlier in the text, and varying $\tilde{v}$ from 23 to 71 nm/s results in values for $D_m = 1.22 - 3.75 \times 10^{-12}$ cm²/s. Literature data for self-diffusion of Al are at comparable values of $D_{Al} = 5.32 \times 10^{-13}$ cm²/s measured by void annihilation [38] and $D_{Al} = 1.85 \times 10^{-13}$ cm²/s determined by tracer experiments [39]. For Cu volume diffusion in Al [40], a similar value of $D_{Cu} = 4.65 \times 10^{-13}$ cm²/s is found, see also Table A.1. Considering that diffusion is expected to be faster along interfaces, values are in reasonable agreement, but should not be over-interpreted. In this context, it is important to note that the thickening of a θ-lamella takes place at the expense of neighbor lamella, as observed in video 2, and is achieved by a movement of the phase boundary perpendicular to the thickening direction. Energy criteria, as in Eq. (9), have been developed for single phase materials, but for multiphase materials more effects would need consideration, e.g. the combined diffusion of Al and Cu, solute drag of additional elements [41] and the orientation dependence of the $\gamma_{\alpha\theta}$ interface energy [37]. A sound description is anything but trivial and is out of the scope of this paper.

Modeling methods as phase-field [42] or molecular dynamics [31] simulations could deepen the understanding of the observed phenomenom.

An important general observation which should be pointed out is that in comparison to the pristine material (Fig. 1b), the strong uni-directional morphology (Fig. 1j) tends to have a higher resistance to recrystallization, compare Fig. 3a to Fig. 1e which both experienced annealing for 3 min at 300 °C. This results from fewer lamella faults, which act as nucleation points for recrystallization, in the strong uni-directional morphology.

4.2. Re-solidified morphologies

A small lamella spacing, according to eutectic scaling laws (Eq. (2)) has been expected for rapid cooling conditions.

Rapid surface re-solidification experiments showed that lamellar spacing can only reach a minimum of ≈ 17 nm and increases again with further increasing solidification velocity [43]. When a critical solidification speed is reached a cellular and dendritic microstructure is expected for eutectic composition [15]. Further a phase replacement for the θ phase has been reported for solidification velocities where the regular eutectic morphology breaks down, and a re-increase in λ spacing is observed [15,43]. For even higher solidification velocities so-called banded regions [11,15] which appear at very high solidification velocities and are the result of an oscillatory solidification. Here no α/θ phase constituents are present any more, but a partitionless (up to a resolution of about 3 nm) solidification of α alternating to θ' phase, which has a kinetic advantage for nucleation due to coherent interfaces to α. [11,44]

However, in general not only the solidification velocity determines the morphology, but also the temperature gradient and the melt composition during the course of solidification. [5,45]

Nucleation [46,47] will influence the amount of undercooling and together with the external heat exchange the recalescence [48] behavior.

The conduction of heat to the unheated parts of the chip is the dominant effect for cooling the membrane. The heat exchange from the sample to the chip will not be ideal heat conduction, but better described by a thermal contact conductance [49], i.e. a heat exchange coefficient between the chip and the solid or liquid specimen. Average cooling rates for the modeling of splat-cooling are discussed in Ref. [50] for both mentioned heat exchange cases and varied thickness.

Comparing to Ref. [9], this work's fastest applied cooling (via pulse heating and free cooling) is estimated to be slower. Due to lack of high sampling frequency, the actual temperature of the membrane was not followed with high enough temporal resolution for the pulse heating with free cooling experiment. The chip membrane part which is heated via Joule heating [20] here is $\approx 200 \times 200$ µm² (see Fig. 1a) comparing to the meltpoolsize of $\approx 27 \times 35$ µm² in Ref. [9]. Still, rapid coooling conditions can be realized, for the predecessor chips membrane a maximum cooling rate in the order of 10^6 K/s is reported in Ref. [20].

The area of the sample is seen to decrease with increasing time in the melt/subsequent number of melting and re-solidification cycles, compare feature A in Fig. 4a to b. With decreasing area the thickness of the specimen increases, see also Section B.1.

Direct comparison to the microstructure selection map from e.g. Ref. [15] is difficult; the solidification structures are produced upon an imposed cooling rate at the chip, but the selection map requires a solidification velocity, which is indirectly deduced from the laser movement velocity [43].

For the pulse heating experiment with free cooling (Fig. 4a) a lamellar morphology with a spacing of ≈ 22 nm is observed. We could identify the Al₂Cu lamella for a pulse heating experiment as θ-Al₂Cu (see Supplementary Material Fig. 1). Surface grains in a dendrite morphology and a partial lamellar coarse structure are observed with a cooling rate of 100 K/s. The change of morphology from one to another is attributed to the imposed cooling rate at the chip and change in thickness of the specimen.

The exact linkage between the quantities as temperature gradient, cooling rate and solidification velocity depends on the solution of the *Stefan* problem [1,51] (moving boundary condition). The temperature distribution could be simulated e.g. via the finite difference method [50,52], finite element method (e.g. as in Ref. [53]) or other numerical methods.

It should be noted that in general the occurrence of additional elements [6,54] will strongly affect the solidification behavior. Therefore ternary/off-eutectic compositions could limit the applicability of the calculated [16] microstructure selection map of Reference [15].

4.2.1. Composition analysis

Looking at Al and Cu contents only (Table B.1), one observes an off-stoichiometry for the pristine state of the θ-phase (Al$_2$Cu), comparing an average Cu content of 26.3 to 33.3 at.% Cu. Calculating the ratio of the overall sample composition (14.6 at.% Cu) to the expected (OES measured) value of 17.5 gives a value of 0.83, proceeding the same way for the Cu content of the Al$_2$Cu phase gives a ratio of 0.79. The measured deficiency is therefore likely caused by an underestimation of the Cu content due to the used k-factor method. Besides the Al and Cu signal expected from the specimen, further artefact element signals are detected as discussed in Appendix B, which could additionally contribute to uncertainty in EDS composition. Furthermore, for very small sized features, EDS measured values (e.g. fine lamellas) could be influenced by limited resolution of the sampling area. No significant correlation between different morphologies and Cu content are deduced from EDS.

5. Summary and conclusions

With this set of experiments it is demonstrated that in-situ STEM solidification of an nanoscaled eutectic alloy is possible, using a recently developed sample preparation method [21] and a MEMS based heating/cooling holder. Even subsequent experiments with the same specimen are conducted.

Two examples for potential investigations with the newly developed methodology are reported in detail, influence of the cooling conditions on the rapid solidification morphology and recrystallization heat treatments.

With application of pulse heating and free cooling from the melt, a strong uni-directional, nanostructured morphology could be observed, reaching a lamella spacing of 22 nm. Using a cooling rate of 100 K/s, the re-solidified morphology is coarser by at least an order of magnitude.

Analysis of in-situ recrystallization experiments shows an average interface velocity of 41 nm/s at 300 °C for lamella thickening. For this special recrystallization case a term for the thermodynamical driving force is developed (Eq. (10)). Besides this findings a general higher resistance of strongly oriented lamellas against recrystallization is observed.

Applying the demonstrated experimental setup opens up a new way for in-situ solidification studies of Al based alloys and likely other metallic materials. Post-solidification heat treatments, like additional heatspikes observed after solidification, as for e.g. mimic additive manufacturing, are able to be investigated. Although some limitations due to free surface of the TEM specimen should be considered [55–57].

Declaration of Competing Interest

The authors declare no competing interests.

Acknowledgements

Appendix A. Model for lamellar thickening

A simplified geometry as seen in Fig. 5 is used. Due to simplification, the three-dimensional problem is reduced to a two-dimensional problem. Instead of interface areas only the interface 'lines' need to be counted.

Before the movement of the boundary the interface lines have the length s_0 seen in Eq. (A.1) and after the movement of dx the length s_1 of Eq. (A.2). d_α and d_θ are the respective width of the α and θ lamella and x_1, x_2 the length of the thickened, respectively the initial lamella. This interface length change of Eq. (A.3) over the volume $\lambda h dx$, inserted into Eq. (8), leads to Eq. (A.4).

$$s_0 = x_1 + d_\alpha + x_2 + 2x_2 + d_\theta \tag{A.1}$$

$$s_1 = x_1 + dx + d_\alpha + (x_2 - dx) + 2(x_2 - dx) + d_\theta \tag{A.2}$$

$$s_1 - s_0 = -2dx \tag{A.3}$$

$$p = -\frac{-2h\gamma_{\alpha\theta}dx}{\lambda_{\text{init}}hdx} \tag{A.4}$$

Therefore the energy consideration leads to an expression as in Eq. (10) during interface/grain boundary movement.

Table A1

Numerical values for diffusion constant calculations according to $D = D_0 \exp\left(-\frac{Q}{RT}\right)$.

Ref.	D_0 [cm^2/s]	Q [kJ/mol]
[38]	0.176	126.39
[39]	1.710	142.29
[40]	0.150	126.40

In Table A.1 information is given, which is used for calculation of the literature diffusion constants in Section 4.1. The interested reader is referred to Reference [58] for diffusion constants in the liquid state.

Appendix B. EDS Analysis, contamination, oxide layer and the occurence of Si

Compositional analysis is performed via EDS as reported in Table B.1. In Fig. B.1 the uni-directional lamellar structure (Fig. 4a) is shown with the respective EDS mappings for Al, Cu, Si and O. The Cu rich lamellas show approximately the composition of θ-Al$_2$Cu, and Al rich show the composition expected for α-Al with solute Cu. Despite clearly discernible lamellas for Al and Cu, there seem to be inter-connected lamellas, possibly over layers of surface crystals of the respective phase. The resulting Cu and Al contents of the by HAADF contrast discernible phases are reported in Table B.1.

Table B.1

EDS chemical analysis. For evaluation Al, Cu as possible elements were chosen. C and O as possible contamination and further Si signal (originating from the Si_3N_4 membrane) is neglected in the evaluation.

sample state	morphology	HAADF phase	Al [at.%]	Cu [at.%]
pristine	lamellar	bright[a]	73.7	26.3
		dark[b]	96.6	3.4
		overall[c]	85.4	14.6
pulse heated	lamellar	bright	73.9	26.1
		dark	98.7	1.3
		overall	86.6	13.4
cooled with 100 K/s[d]	dendritic surface grains, coarse lamellas			

[a] Sampling area of θ-Al_2Cu.
[b] Sampling area of α-Al.
[c] Sampling area of overall morphology.
[d] No EDS measured.

(a) HAADF (b) Al (gren), Cu (red) (c) Si (d) O
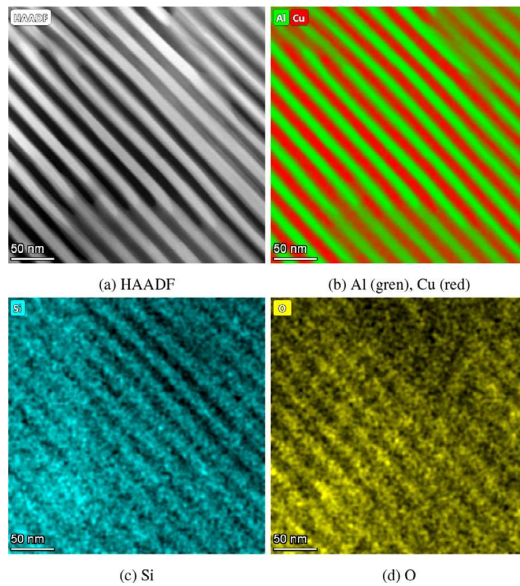
Fig. B.1. HAADF and EDS images after of uni-directional lamellas (Fig. 4a). Bright areas are Cu rich (θ-Al_2Cu) and dark areas are rich in Al (α-Al). It can be seen that some lamellas are likely interconnected over a small surface layer of the respective phase. Si seems to be partitioned into θ-Al_2Cu, while O is more prominent in α-Al lamellas.

As seen in Fig. B.1, Si seems to be partitioned into the θ-Al_2Cu lamellas, while O is prominent in α-Al lamellas. The same partitioning behavior is also observed for recrystallized structures. No partitioning could be observed for C.

C is a typical surface contaminant and likely emerges from cleaning residues. No defined aggregation behavior in the sample has been observed.

O is expected from surface oxidation, but also partitioning seems to be apparent into α-Al. While higher surface oxidation of α-Al phase in the pristine sample could be possible, for the re-solidified sample (as in Fig. B.1), it is not expected for newly formed lamellas, due to operation under high vacuum (HV) conditions in the STEM. The amount measured (order of percentage) is far beyond solubility for an interstitial element, especially for Al with almost non-existent solubility of O. In fact, for the shown state in Fig. B.1d, only little partitioning, approx. 0.5% at. absolute excess, is observed. The found intensity is likely overlaid with an existing signal from an oxide layer, and possibly an artefact of stray radiation.

Si is observed to be partitioned into θ-Al_2Cu. A source of Si signal can be stray signal from the Si_3N_4 holder. Direct signal from

the membrane can be excluded due to observation at a membrane hole. The observed supposedly partitioning of Si into the θ-Al_2Cu phase can be explained by the x-ray fluorescence of excited Cu atoms. Si in the material is further ruled out by an additional SEM EDS of a ribbon from the same batch, showing only Al and Cu, but no Si signals.

B1. Sample shape

After the sample preparation, the sample is thought to be in a wedge shape, a form with varying thickness over sample in plane dimensions, but with a low thickness to width ratio ($\approx 1/500$) in general. An oxide layer is expected at the surface due to preparation at atmosphere and rapid (passivating) surface oxidation of Al alloys.

If the initial contact-angle ψ between liquid (sample) and solid (membrane) is lower than the equilibrium value determined by Youngs' equation (Eq. (B.1)), then during the liquid state an increase in thickness by spheroidization/balling is expected until the equilibrium angle and shape is reached. σ_{sg}, σ_{sl} and σ_{lg} here denote respectively the solid-gas, solid-liquid and the liquid-gas surface tensions. Due to the low aspect ratio, the assumption of a too low initial contact angle seems plausible. The spheroidization to reach equilibrium shape is in general a time and temperature dependent process, due to needed directional movement, or flow, of atoms by diffusion in the melt.

$$\cos(\psi) = \frac{\sigma_{sg} - \sigma_{sl}}{\sigma_{lg}} \tag{B.1}$$

It should be noted that other metal systems than Al based systems might exhibit different spheroidization/balling characteristics.

B2. Oxide layer and pile-up

The role of a surface oxide layer at the specimen between the sample and holder is difficult to judge. The oxide layer could contribute to a decreased thermal contact conductance coefficient. An oxide layer formed at atmosphere is usually only some few nanometers in thickness and of amorphous nature. Cracking surface oxide layers upon heating could be expected, likely due to different heat expansion coefficients of oxide and metal. However, the remaining roll-up artefact after several melting and re-solidification events of the sample hints to some form stability of at least some parts of the oxide layer.

Supplementary material

Supplementary material associated with this article can be found, in the online version, at doi:10.1016/j.actamat.2022.118225.

References

[1] M.E. Glicksman, Principles of Solidification, Springer, New York, NY, 2011, doi:10.1007/978-1-4419-7344-3.

[2] Kurz, Fisher, Fundamentals of Solidification, Trans Tech Publications, 1984.

[3] S. Gorsse, C. Hutchinson, M. Gouné, R. Banerjee, Additive manufacturing of metals: a brief review of the characteristic microstructures and properties of steels, Ti-6Al-4V and high-entropy alloys, Sci. Technol. Adv. Mater. 18 (1) (2017) 584–610, doi:10.1080/14686996.2017.1361305.

[4] W. Kurz, R. Trivedi, Rapid solidification processing and microstructure formation, Mater. Sci. Eng. A 179–180 (1994) 46–51.

[5] W. Kurz, D.J. Fisher, R. Trivedi, Progress in modelling solidification microstructures in metals and alloys: dendrites and cells from 1700 to 2000, Int. Mater. Rev. 64 (6) (2019) 311–354, doi:10.1080/09506608.2018.1537090.

[6] B. Chanda, G. Potnis, P.P. Jana, J. Das, A review on nano-/ultrafine advanced eutectic alloys, J. Alloys Compd. 827 (2020) 154226, doi:10.1016/j.jallcom.2020.154226.

[7] P. Shi, W. Ren, T. Zheng, Z. Ren, X. Hou, J. Peng, P. Hu, Y. Gao, Y. Zhong, P.K. Liaw, Enhanced strength-ductility synergy in ultrafine-grained eutectic high-entropy alloys by inheriting microstructural lamellae, Nat. Commun. 10 (1) (2019) 489, doi:10.1038/s41467-019-08460-2.

[8] Q. Lei, B.P. Ramakrishnan, S. Wang, Y. Wang, J. Mazumder, A. Misra, Structural refinement and nanomechanical response of laser remelted Al-Al2Cu lamellar eutectic, Mater. Sci. Eng. A 706 (2017) 115–125, doi:10.1016/j.msea.2017.08.105.

[9] J.T. McKeown, A.K. Kulovits, C. Liu, K. Zweiacker, B.W. Reed, T. LaGrange, J.M. Wiezorek, G.H. Campbell, In situ transmission electron microscopy of crystal growth-mode transitions during rapid solidification of a hypoeutectic Al–Cu alloy, Acta Mater. 65 (2014) 56–68, doi:10.1016/j.actamat.2013.11.046.

[10] J.T. McKeown, K. Zweiacker, C. Liu, D.R. Coughlin, A.J. Clarke, J.K. Baldwin, J.W. Gibbs, J.D. Roehling, S.D. Imhoff, P.J. Gibbs, D. Tourret, J.M.K. Wiezorek, G.H. Campbell, Time-resolved in situ measurements during rapid alloy solidification: experimental insight for additive manufacturing, JOM 68 (3) (2016) 985–999, doi:10.1007/s11837-015-1793-x.

[11] V. Bathula, C. Liu, K. Zweiacker, J. McKeown, J.M. Wiezorek, Interface velocity dependent solute trapping and phase selection during rapid solidification of laser melted hypo-eutectic Al-11at.%Cu alloy, Acta Mater. 195 (2020) 341–357, doi:10.1016/j.actamat.2020.04.006.

[12] W. Tiller, Liquid metals and solidification, ASM Cleveland Ohio 276 (1958) 24.

[13] J. Hunt, K. Jackson, Lamellar and rod eutectic growth, Trans. Metall. Soc. AIME 236 (1966) 1129–1142.

[14] Lemaignan, Initial stages of eutectic solidification, Acta Metall. 29 (1981) 1379–1384.

[15] S.C. Gill, W. Kurz, Rapidly solidified Al-Cu alloys–I. Experimental determination of the microstructure selection map, Acta Metall. Mater. 41 (12) (1993) 3563–3573.

[16] S.C. Gill, W. Kurz, Rapidly solidified Al-Cu alloys'II. Calculation of the microstructure selection map, Acta Metall. Mater. 43 (1) (1995) 139–151.

[17] M.J. Aziz, T. Kaplan, Continuous growth model for interface motion during alloy solidification, Acta Metall. 36 (8) (1988) 2335–2347.

[18] G. Kurtuldu, K.F. Shamlaye, J.F. Löffler, Metastable quasicrystal-induced nucleation in a bulk glass-forming liquid, Proc. Natl. Acad. Sci. U.S.A. 115 (24) (2018) 6123–6128, doi:10.1073/pnas.1717941115.

[19] J.F. Löffler, Bulk metallic glasses, Intermetallics 11 (6) (2003) 529–540, doi:10.1016/S0966-9795(03)00046-3.

[20] L.F. Allard, W.C. Bigelow, M. Jose-Yacaman, D.P. Nackashi, J. Damiano, S.E. Mick, A new MEMS-based system for ultra-high-resolution imaging at elevated temperatures, Microsc. Res. Tech. 72 (3) (2009) 208–215, doi:10.1002/jemt.20673.

[21] M.A. Tunes, C.R. Quick, L. Stemper, D.S.R. Coradini, J. Grasserbauer, P. Dumitraschkewitz, T.M. Kremmer, S. Pogatscher, A Fast and Implantation-Free Sample Production Method for Large Scale Electron-Transparent Metallic Samples Destined for MEMS-Based In Situ S/TEM Experiments, Materials 14 (5) (2021) 1085, doi:10.3390/ma14051085.

[22] M.A. Tunes, C. Quick, L. Stemper, D.S.R. Coradini, J. Grasserbauer, P. Dumitraschkewitz, T.M. Kremmer, S. Pogatscher, A contamination-free electron-transparent metallic sample preparation method for MEMS experiments with in situ S/TEM, 2020b, arXiv preprint arXiv:2012.02941

[23] Mettler-Toledo GmbH, Flash DSC 2+ User Manual V3.00, 2018.

[24] B. Yang, B. Milkereit, Y. Zhang, P.A. Rometsch, O. Kessler, C. Schick, Continuous cooling precipitation diagram of aluminium alloy AA7150 based on a new fast scanning calorimetry and interrupted quenching method, Mater. Charact. 120 (2016) 30–37, doi:10.1016/j.matchar.2016.08.016.

[25] N. Shamim, Y.P. Koh, S.L. Simon, G.B. McKenna, Glass transition temperature of thin polycarbonate films measured by flash differential scanning calorimetry, J. Polym. Sci. Part B Polym. Phys. 52 (22) (2014) 1462–1468, doi:10.1002/polb.23583.

[26] G.V. Poel, D. Istrate, A. Magon, V. Mathot, Performance and calibration of the Flash DSC 1, a new, MEMS-based fast scanning calorimeter, J. Therm. Anal. Calorim. 110 (3) (2012) 1533–1546, doi:10.1007/s10973-012-2722-7.

[27] P. Dumitraschkewitz, M.A. Tunes, C.R. Quick, D.S.R. Coradini, T.M. Kremmer, P.J. Uggowitzer, S. Pogatscher, STEM AlCu videos, 2020. Mendeley Data, V1, https://doi.org/10.17632/vkjmpct4pm.1.

[28] G. W. Greenwood, The growth of dispersed precipitates in solutions, Acta Metall. 4 (1956) 243–247.

[29] G. Gottstein, Physikalische Grundlagen der Materialkunde, Springer-Lehrbuch, 3. aufl. ed., Springer, Berlin, Heidelberg, 2007.

[30] G. Gottstein, D.A. Molodov, L.S. Shvindlerman, Grain boundary migration in metals: recent developments, Interface Sci. 6 (1998) 7–22.

[31] M. Upmanyu, D.J. Srolovitz, L.S. Shvindlerman, G. Gottstein, Molecular dynamics simulation of triple junction migration, Acta Mater. 50 (2002) 1405–1420.

[32] G. Gottstein, V. Sursaeva, L.S. Shvindlerman, The effect of triple junctions on grain boundary motion and grain microstructure evolution, Interface Sci. 7 (1999) 273–283.

[33] G. Gottstein, Y. Ma, L.S. Shvindlerman, Triple junction motion and grain microstructure evolution, Acta Mater. 53 (5) (2005) 1535–1544, doi:10.1016/j.actamat.2004.12.006.

[34] C. Bauer, Mechanisms for grain boundary migration, in: Defect and Diffusion Forum, vol. 66, Trans Tech Publ., 1990, pp. 749–764.

[35] G. Gottstein, L.S. Shvindlerman, On the true dependence of grain boundary migration rate on driving force, Scr. Metall. Mater. 27 (1992) 1521–1526.

[36] Y. Zhang, A. Godfrey, D.J. Jensen, Local boundary migration during recrystallization in pure aluminium, Scr. Mater. 64 (4) (2011) 331–334, doi:10.1016/j.scriptamat.2010.10.028.

[37] V. Kokotin, U. Hecht, Molecular dynamics simulations of Al–Al2Cu phase boundaries, Comput. Mater. Sci 86 (2014) 30–37, doi:10.1016/j.commatsci.2014.01.014.

[38] T.E. Volin, R.W. Ballufe, Annealing kinetics of voids and the self–diffusion coefficient in aluminum, Phys. Stat. Sol. 25 (1968).

[39] T.S. Lundy, J.F. Murdock, Diffusion of Al^{26} and Mn^{54} in aluminum, J. Appl. Phys. 33 (5) (1962) 1671–1673.

[40] M.S. Anand, S.P. Murarka, R.P. Agarwala, Diffusion of copper in nickel and aluminum, J. Appl. Phys. 36 (12) (1965) 3860–3862.

[41] J.C. Verhasselt, G. Gottstein, D.A. Molodov, L.S. Shvindlerman, Shape of moving grain boundaries in Al-bicrystals, Acta Mater. 47 (3) (1999) 887–892, doi:10.1016/S1359-6454(98)00398-X.

[42] T. Pinomaa, J.M. McKeown, J.M. Wiezorek, N. Provatas, A. Laukkanen, T. Suhonen, Phase field modeling of rapid resolidification of Al-Cu thin films, J. Cryst. Growth 532 (2020) 125418, doi:10.1016/j.jcrysgro.2019.125418.

[43] M. Zimmermann, M. Carrard, W. Kurz, Rapid solidification of Al-Cu eutectic alloy by laser remelting, Acta Metall. 37 (12) (1989) 3305–3313.

[44] K.W. Zweiacker, C. Liu, M.A. Gordillo, J.T. McKeown, G.H. Campbell, J. Wiezorek, Composition and automated crystal orientation mapping of rapid solidification products in hypoeutectic al-4 at.%cu alloys, Acta Mater. 145 (2018) 71–83, doi:10.1016/j.actamat.2017.11.040.

[45] W. Kurz, D.J. Fisher, Dendrite growth in eutectic alloys: the coupled zone, Int. Metals Rev. 24 (1) (1979) 177–204, doi:10.1179/imtr.1979.24.1.177.

[46] C. Simon, J. Gao, Y. Mao, G. Wilde, Fast scanning calorimetric study of nucleation rates and nucleation transitions of Au-Sn alloys, Scr. Mater. 139 (2017) 13–16, doi:10.1016/j.scriptamat.2017.06.004.

[47] B. Yang, Q. Peng, B. Milkereit, A. Springer, D. Liu, M. Rettenmayr, C. Schick, O. Keßler, Nucleation behaviour and microstructure of single Al-Si12 powder particles rapidly solidified in a fast scanning calorimeter, J. Mater. Sci. (2021), doi:10.1007/s10853-021-06096-6.

[48] C. Levi, R. Mehrabian, Heat flow during rapid solidification of undercooled metal droplets, Metall. Trans. A 13 (2) (1982) 221–234.

[49] A. Minakov, J. Morikawa, E. Zhuravlev, M. Ryu, C. Schick, Thermal contact conductance at melting and crystallization of metal micro-droplets, Mater. Res. Express 7 (6) (2020) 066524, doi:10.1088/2053-1591/ab9a7e.

[50] R.C. Ruhl, Cooling rates in splat cooling, Mater. Sci. Eng. (1967) 313–320.

[51] H.S. Carslaw, J.C. Jaeger, Conduction of Heat in Solids, second ed., Oxford university press, Oxford, 1959.

[52] J. Crank, The Mathematics of Diffusion, second ed., Clarendon Press, Oxford, 1975.

[53] T. Keller, G. Lindwall, S. Ghosh, L. Ma, B.M. Lane, F. Zhang, U.R. Kattner, E.A. Lass, J.C. Heigel, Y. Idell, M.E. Williams, A.J. Allen, J.E. Guyer, L.E. Levine, Application of finite element, phase-field, and CALPHAD-based methods to additive manufacturing of Ni-based superalloys, Acta Mater. 139 (2017) 244–253, doi:10.1016/j.actamat.2017.05.003.

[54] U. Hecht, L. Gránásy, T. Pusztai, B. Böttger, M. Apel, V. Witusiewicz, L. Ratke, J. de Wilde, L. Froyen, D. Camel, B. Drevet, G. Faivre, S.G. Fries, B. Legendre, S. Rex, Multiphase solidification in multicomponent alloys, Mater. Sci. Eng. R Rep. 46 (1–2) (2004) 1–49, doi:10.1016/j.mser.2004.07.002.

[55] P. Saidi, M. Topping, C. Dai, F. Long, L.K. Béland, M.R. Daymond, The dependence of damage accumulation on irradiation dose rate in zirconium alloys: rate theory, atomistic simulation and experimental validation, J. Nucl. Mater. 543 (2021) 152478, doi:10.1016/j.jnucmat.2020.152478.

[56] Q. Dong, P. Saidi, H. Yu, Z. Yao, M.R. Daymond, A direct comparison of annealing in TEM thin foils and bulk material: application to Zr-2.5Nb-0.5Cu alloy, Mater. Charact. 151 (2019) 175–181, doi:10.1016/j.matchar.2019.03.002.

[57] P. Dumitraschkewitz, P.J. Uggowitzer, S.S.A. Gerstl, J.F. Löffler, S. Pogatscher, Size-dependent diffusion controls natural aging in aluminium alloys, Nat. Commun. 10 (1) (2019) 4746, doi:10.1038/s41467-019-12762-w.

[58] U. Dahlborg, M. Besser, M. Calvo-Dahlborg, S. Janssen, F. Juranyi, M.J. Kramer, J.R. Morris, D.J. Sordelet, Diffusion of Cu in AlCu alloys of different composition by quasielastic neutron scattering, J. Non Cryst. Solids 353 (32–40) (2007) 3295–3299, doi:10.1016/j.jnoncrysol.2007.05.074.